DEPARTMENT OF ELECTRONIC & ELECTRICAL ENGINEERING

University of Strathclyde Engineering

Wideband Data-Independent Beamforming for Subarrays

Abdullah Alshammary

Centre for Excellence in Signal and Image Processing

Department of Electronic and Electrical Engineering

University of Strathclyde, Glasgow

A Dissertation Presented in Partial Fulfillment

of the Requirements for the Degree

Doctor of Philosophy

October 31, 2018

This thesis is the result of the authors original research. It has been composed by the author and has not been previously submitted for examination which has led to the award of a degree.

Signed:

Date:

Abstract

The desire to operate large antenna arrays for e.g. RADAR applications over a wider frequency range is currently limited by the hardware, which due to weight, cost and size only permits complex multipliers behind each element. In contrast, wideband processing would have to rely on tap delay lines enabling digital filters for every element. As an intermediate step, in this thesis we consider a design where elements are grouped into subarrays, within which elements are still individually controlled by narrowband complex weights, but where each subarray output is given a tap delay line or finite impulse response digital filter for further wideband processing.

Firstly, this thesis explores how a tap delay line attached to every subarray can be designed as a delay-and-sum beamformer. This filter is set to realised a fractional delay design based on a windowed sinc function. At the element level, we show that designing a narrowband beam w.r.t. a centre frequency of wideband operation is suboptimal, and suggest an optimisation technique that can yield sufficiently accurate gain over a frequency band of interest for an arbitrary look direction, which however comes at the cost of reduced aperture efficiency, as well as significantly increased sidelobes.

We also suggest an adaptive method to enhance the frequency characteristic of a partial wideband array design, by utilising subarrays pointing in different directions in different frequency bands — resolved by means of a filter bank — to adaptively suppress undesired components in the beam patterns of the subarrays.

Finally, the thesis proposes anovel array design approach obtained by rotational tiling of subarrays such that the overall array aperture is densely constructed from the same geometric subarray by rotation and translation only. Since the grating lobes of differently oriented subarrays do not necessarily align, an effective grating lobe atten-

uation w.r.t. the main beam is achieved. Based on a review of findings from geometry, a number of designs are highlight and transformed into numerical examples, and the theoretically expected grating lobe suppression is compared to uniformly spaced arrays.

Supported by a number of models and simulations, the thesis thus suggests various numerical and hardware design techniques, mainly the addition of tap-delay-line per subarray and some added processing overhead, that can help to construct a large partial wideband array close in wideband performance to currently existing hardware.

Contents

List of Figures

List of Tables

Acknowledgements

I like to thank my supervisor Dr Stephan Weiss for his guidance, support and keen interest in every idea. But above all, his charming and caring personality.

I also thank John Soraghan, Ahmed Alzain, Amr Nagy and the rest of my colleges in Signal & Image Processing research group for the advices and fruitful discussions.

Publications

- A. Alshammary; S. Almorqi, Wideband 2-Dimensional scanning planar subarray. 10th IMA International Conference on Mathematics in Signal Processing 2014, Birmingham.
- A. Alshammary; S. Weiss. Low-cost and accurate broadband beamforming based on narrowband sub-arrays. 20th International ITG Workshop on Smart Antennas WSA 2016, Munich Germany.
- A. Alshammary; S. Weiss.; S. Almorqi. Grating Lobe Suppression in Rotationally Tiled Arrays. 11th European Conference on Antennas and Propagation EUCAP 2017, Paris, France.
- Patent number 5832, Abdullah Alshammary; Sultan Almorqi, Wideband antenna array with modular subarray. Saudi Patent Office.

List of Abbreviations

ADC	Analog to Digital conversion
AESA	Active Electronically Steered Array
ANC	Adaptive Noise Cancellation
APA	Affine Projection Algorithm
dB	Decibels
DFT	Discrete Fourier Transform
DSP	Digital Signal Processing
FDF	Fractional Delay Filter
FFT	Fast Fourier Transform
FIBP	Frequency Invariant Beam Pattern
FIR	Finite Impulse Response
GSC	Generalised Sidelobe Canceler
GVF	Gradient Vector Flow
IIR	Infinite Impulse Response
LFM	Linear Frequency Modulation
LFOV	Limited Field Of Regard
l.h.s.	left hand side
LPI	Low Probability of Intercept
NCTI	Non-Cooperative Target Identification
NLMS	Normalized Least Means Squares

PIC	Postbeamformer Interference Canceler
PSD	Power Spectral Density
QCQP	Quadratically Constrained Quadratic Programming
RF	Radio Frequency
r.h.s.	right hand side
RLS	Recursive Least Square
SIFT	Scale-Invariant Feature Transform
SAR	Synthetic Aperture Radar
SDL	Sensor Delay Line
SLL	Sidelobe Level
SINR	Signal to Interference plus Noise Ratio
SPC	Statistical Process Control
SRV	Spatial Response Variation
TDL	Tapped Delay Line
TDU	Time Delay Unit
TTD	True Time Delay
UHF	Ultra Hight Frequency
VHF	Very High Frequency
w.r.t.	with respect to

Common Symbols

General Notations

a	Scalar quantity
$\mathbf{a}$	Vector quantity
$\mathbf{A}$	Matrix quantity
$\mathbf{A}^\dagger$	Pseudo-inverse of matrix $\mathbf{A}$
$\mathbb{Z}$	Space of integer numbers
$\mathbb{C}^K$	Space of complex valued column vectors of size K
$\mathbb{R}^K$	Space of real valued column vectors of size K

Relations and operators

$(.)^{\mathrm{T}}$	Transpose operation
$(.)^{*}$	Conjugate operation
$(.)^{\mathrm{H}}$	Conjugate transpose operation
$\|\|.\|\|_F$	Frobenius norm of a matrix
$\mathbf{1}_p$	Column vector of ones with length p
$\mathbf{1}_{p\mathrm{x}q}$	Matrix of ones with size pxq
$std()$	Standard deviation function
$\lfloor \rceil$	Rounding function
$\circ\!\!-\!\!\bullet$	Discrete Fourier Transform pair, $s[n] \ \circ\!\!-\!\!\bullet \ S(e^{j\Omega})$
$\bullet\!\!-\!\!\circ$	Inverse Discrete Fourier Transform pair, $S(e^{j\Omega}) \ \bullet\!\!-\!\!\circ \ s[n]$
Δ	Difference operator e.g. $\Delta\mathbf{k} = \mathbf{k} - \mathbf{k}_0$
$\Phi(.)$	Phase of a complex value
c_{in}	Incircle of a Euclidean shape
$Conv(.)$	Convex hull of a set of points
$diag(\mathbf{A})$	Vector of the diagonal elements of matrix $\mathbf{A}$
$std()$	Standard deviation
$sgn()$	Sign function
$LCM()$	Least common multiple
N	Total number of array elements
M	Number of subarray
J	Order of tapped delay line
$\mathbf{w}^{\mathrm{H}}$	Antenna narrowband weights
$\mathbf{v}^{\mathrm{H}}$	Antenna wideband weights
τ	Time delay
d	Elements spacing
$P(\omega, \theta, \phi)$	Array response
$P_d(\omega, \theta, \phi)$	Desired array response
ξ_{ss}	Sum of squares of mailobe deviation

λ	Wavelength
T_s	Sampling time
ξ	the summation of the error squares over space and frequency
$\odot$	Element-wise multiplication
$\otimes$	Kronecker product

Chapter 1

Introduction

This is a study of wideband antenna subarray design and beamforming. Standard wideband beamforming requires time delay units or digital receivers for each array element. The work of this thesis focuses on achieving a suitable wideband characteristic by controlling the narrowband weights of the individual array elements, introducing tap delay line for groups of sensors organized in subarrays, and improving the subarrays processing and geometry.

1.1 Background and Motivation

Introducing adaptive processing or expanding the instantaneous bandwidth of an antenna array generally requires the digital representation of the signal paths at the element level [1], or introducing time delay units [2], or sacrificing a spatial domain to apply spectral domain processing [3]. Antenna arrays that utilise these components have a frequency-invariant response but are also large, heavy and have a high power demand. Many applications that require adaptive processing can meet the required performance with fewer degrees of freedom compared to the number of antenna elements contained within their antenna array. For example, the number of targets and interference sources that a phased array radar needs to handle is lower than its number of elements, compared to the number of elements required to meet a certain gain or beamwidth.

In addition, there are many practical factors that restricts the wideband performance of an array like the antenna element, the microwave distribution and switching network and the digital receivers sampling speed and throughput.

The main motivation of adopting subarray structures in this thesis, is to meet the practical constraints in airborne and mobile antenna array systems that need wide instantaneous bandwidth to fulfil their missions. For example, the next-generation airborne active electronically steered array (AESA) radar in fighter aircrafts promises to perform high resolution imaging by functioning as synthetic aperture radar (SAR), identify threats using non-cooperative target identification (NCTI), improve detection and tracking by applying advanced signal processing algorithms like space-time adaptive processing and reuse radar front end for electronic warfare and communications functions [4]. While advancements in microwave and fabrication led to the miniaturisation of phase shifters, the true time delay and analog to digital conversion are impractical at element level on airborne AESA.

Subarray structures allow the system designer to control the performance of the antenna and the signal processing requirements independently, especially when the required number of the receiver channels is a fraction of the array size. For example, AESA radar can improve clutter and jammer rejection while conforming to size, weight, heat dissipation, and power consumption. A subarray structure is not without drawbacks. The additional weighting at the subarray level is excessive if the required performance and constraints can be met by a fully analog or fully digital array. Improving the elements weighting can be more feasible than adding an additional layer to an already complex system.

This thesis specifically targets phased array radars that traditionally utilise complex weighting at elements level. Among phased array radar aspects that this thesis aims to improve are,

- broadband waveforms required for high range resolution, target classifications, imaging and Low Probability of Intercept (LPI) Radars.
- Life cycle cost reduction by introducing modularity. Utilising common components reduces time and cost of design, verification and integration. It also offers

higher reliability and easier maintenance.

- Multi-functionality by offering a highly flexible spatial and spectral response.

Most beamforming techniques target arrays at the element level. Most of the reviewed literature on subarrays deals with the formation of grating lobes or studies the bandwidth impact of Time Delay Units (TDU). Adaptive subarray processing in Radars and acoustics is also an active topic. This study applies wideband beamforming to subarrays and proposes subarray structures and beamformers to resolve bandwidth-related issues like beam squinting, spectral flatness and grating lobes.

1.2 Original contributions

The following is considered to be the novel contributions of this research.

- **Low-cost and accurate broadband beamforming based on narrowband subarrays [5].** Simplified broadband beamformers can be constructed by sharing a single tapped delay line within a narrowband subarray. This contribution proposes the use of fractional delay filters for steering in the digital domain. For the narrowband subarrays, an optimisation approach is proposed to maintain a flat off-broadside beam pointing constraint across a given frequency range.

- **Beam alignment using phase windowing.** Current implementations of beam-steering or delay-and-sum beamforming suggest a linear phase progression calculated at the centre of the operating frequency band. Even if the wideband beamforming is utilisedon narrowband arrays, most beamformers use a single frequency point that minimizes the variation across the bandwidth. Linear phased progression results in beam drift across the frequency range in the mainlobe. I suggested applying a window function on the elements' phase shift of a partially adaptive subarray. This window maintains a peak response towards the desired direction across the band.

- **Interference suppression of a phase-windowed partial wideband array.** Using the phase windowing in partial wideband arrays, a subband adaptive noise

cancellation filter bank uses the subarrays steered away from desired direction at each frequency subband as an interference source. The noise cancellation filters individually suppress the interference frequency components from the subarrays output.

- **Grating Lobe Suppression in Rotationally Tiled Arrays [6].** Uniform placement of array elements limits the maximum operational frequency due to the formation of grating lobes. While non-uniform spacing of elements or subarrays has significantly lower grating lobes, it reduces the aperture efficiency and leads to arrays that are difficult to design and manufacture. I proposed a novel planar array design using a modular asymmetric convex-shaped subarray to build the array by rotation and translation, filling the aperture without overlaps or gaps. These new arrays can significantly reduce grating lobes compared to uniform arrays. They can also lower the design, manufacturing and operation costs by offering identical subarrays and providing an array that can be easily scaled in size.

1.3 Outline of the Thesis

The remainder of this thesis is organized as follows.

Chapter 2 reviews wave propagation, array and partial wideband array models. The chapter also introduces technologies necessary to extend the array bandwidth like tapped delay lines and time delay units. Wideband data-independent beamforming techniques are then introduced and discussed. Finally, three different approaches to apply beamforming to partial wideband arrays are described and evaluated.

Chapter 3 introduces the fractional delay filter and how it can be applied to subarrays to improve the partial wideband array's bandwidth. Then, fractional delay filters are combined with an optimisation of the element-level weighting to reduce the variation of frequency response at the desired direction. This approach is illustrated with two examples.

Chapter 4 discusses beam squinting in narrowband arrays and proposes windowing

of the elements' phase shifts in a linear partial wideband array structure. The chapter investigates decorrelation between subarray outputs when a phase windowing is applied. A subband adaptive noise cancellation architecture is then proposed utilising the signal decorrelation between subarray as a result of phase windowing. The phase windowing is demonstrated on a linear, partially adaptive wideband array and compared to the conventional delay-and-sum beamforming.

Chapter 5 reviews the formation of grating lobes in uniformly spaced arrays and the available solutions in the literature. The chapter then introduces the tiling concept in geometry and reviews the related terminology and classifications. The design methodology of tiled arrays and various measures are introduced. Finally, two novel designs of tiled arrays are introduced, simulated and evaluated.

Chapter 6 provides a summary of the contributions and a discussion of the results, and provides some suggestions for further research.

Chapter 2

Wideband Beamforming

2.1 Introduction

The study of antenna arrays dates back to 1920. Among the early researchers in the array field were G. H. Brown, E. Bruce, P. S. Carter, C. W. Hansell, and many others [7]. Antenna arrays were operating in Very High Frequency (VHF) and Ultra High Frequency (UHF) bands during the Second World War. After that, antenna array radars were built in the microwave range [8]. Today, antenna arrays cover more frequencies and have many applications in both the commercial and military areas. It has not been until the recent advances in Gallium arsenide (GaAs) microwave circuitry and real-time signal processing that array antenna have become affordable and reliable enough for mass production and wider ranges of applications. Antenna arrays have recently been deployed in many ground, naval, and airborne platforms because of the reduction in microwave component cost and size, and because of their flexibility compared to single antenna systems [9].

Among the advantages of an antenna array over single antenna systems in radars are the elimination of moving parts, which enhances reliability and speed. An array antenna beam pattern can be controlled electronically, allowing control over the signal environment and pattern characteristics like the gain and sidelobes.

2.2 Wave Propagation

Communication and Radar use radio waves to convey information, detect objects, or measure the environment. Radio waves are electromagnetic waves with wavelengths from 1 mm up to 100,000 km. These waves are interpreted as signals when they arrive at the antenna elements. Radio frequency waves travel in a straight path at the speed of light, which is approximately 3x10^8 m/s.

The propagation of radio frequency (RF) waves in the space is commonly described using Cartesian or spherical coordinates. Cartesian coordinates (x, y, z) are suitable to describe the antenna array geometry and elements locations. Spherical coordinates (r, θ, ϕ) are more suitable to describe wave propagation and signal environment.

Waves propagating from far field sources, called plane waves shown in figure 2.1, have a constant phase along the plane normal to the propagation direction. Consider a sinusoidal signal with frequency $\omega = 2\pi\ f$ and phase Φ propagating towards the origin of the coordinate system. The wave amplitude is assumed constant across the array because the free-space attenuation and path loss is negligible in the relatively small space containing the antenna array. However, the phase of the wave fluctuates in both time and space. If the phase is observed at a specific point in space w.r.t. the phase at the point of origin, it will vary with the product of frequency and time $\omega\ t$. If a snapshot is taken in time, the phase along the propagation path will vary according to the term $\frac{\omega}{c}r$, where r is the length of the propagation path. The space-time representation of the phase function at an observation point $\mathbf{r} = [x, y, z]^{\mathrm{T}}$ is

$$\Phi(t, \mathbf{r}) = \omega\ t + \mathbf{k}^{\mathrm{T}}\mathbf{r}\ , \tag{2.1}$$

where the angular frequency ω is the time rate of change of the wave phase, $\omega = \frac{\partial \Phi}{\partial\, t}$ and is measured in radians per second. The wavenumber vector $\mathbf{k}$

$$\mathbf{k}(\theta, \phi) = -\frac{\omega}{c}\begin{bmatrix} \sin\theta\cos\phi & \vec{x} \\ \sin\theta\sin\phi & \vec{y} \\ \cos\theta & \vec{z} \end{bmatrix} \quad , \tag{2.2}$$

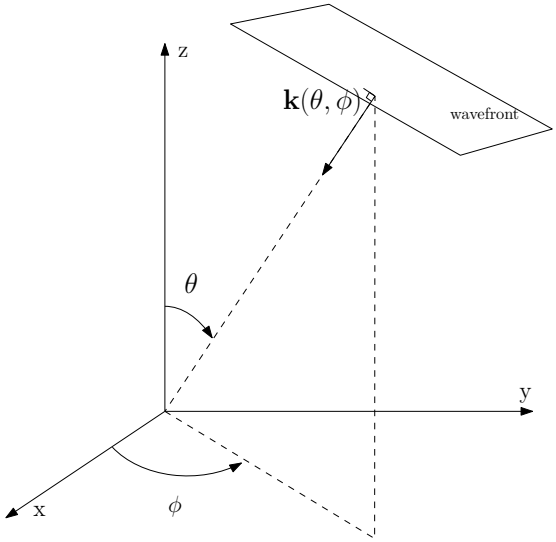

Figure 2.1: Propagation model in Cartesian and spherical coordinates.

which is also referred to as the spatial frequency, is the directional gradient of the wave phase with respect to space. Figure 2.1 demonstrates the wavenumber vector and its relationship to the plane wave propagation. The wavenumber amplitude $|\mathbf{k}|$ is a measure of the wave oscillation per unit distance [10] and is measured in radians per meter. The negative sign indicates an approach of the wave since the azimuth and elevation angles are measured w.r.t. to the point of origin instead of the propagation source. The $u-v$ coordinates are the components of the propagation vector and are commonly used to describe the propagation path,

$$\begin{bmatrix} u \\ v \\ t \end{bmatrix} = \begin{bmatrix} \sin\theta\cos\phi \\ \sin\theta\sin\phi \\ \cos\theta \end{bmatrix} , \tag{2.3}$$

where the third coordinate term $t = \cos\theta$ is omitted when dealing with planar arrays. The wavenumberprojection on the $u-v$ space can be expressed as,

$$\mathbf{k}_{uv} = -\frac{\omega}{c}[u, v]^{\mathrm{T}} . \tag{2.4}$$

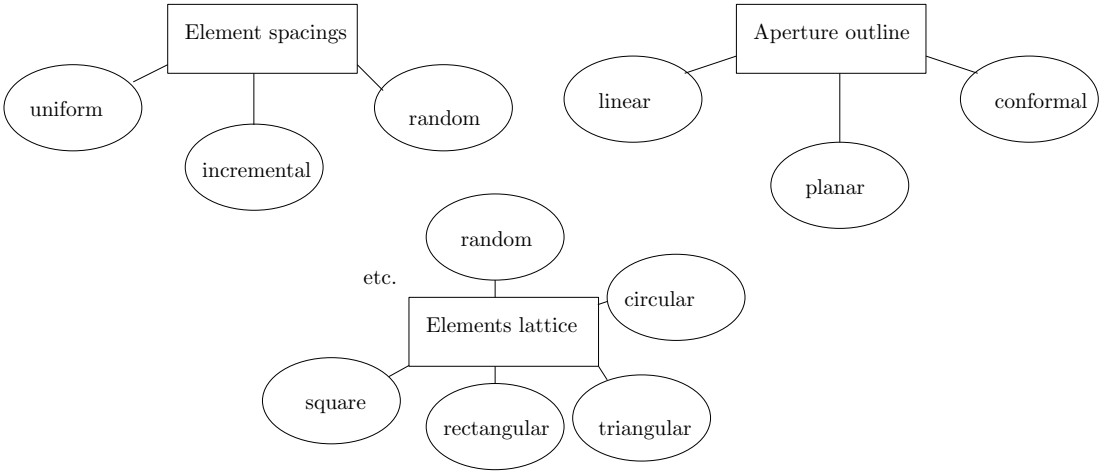

Figure 2.2: Categories of antenna arrays.

2.3 Array Model

The antenna array is a plurality of antennae in proximity that are connected to achieve a performance that is otherwise not possible using an individual antenna. Arrays can be categorized based on their geometry into linear, planar, and conformal arrays. A linear array extends over a straight line. A linear array is steerable in one spatial dimension only. Planar arrays include circular, rectangular and ring arrays, and are steerable in both azimuth and elevation angles. A conformal array takes the shape of its platform due to constraints such as aerodynamics, structural integrity, and aesthetics. Figure 2.2 lists such antenna array classifications and types.

The element distribution can be uniform, where the element spacings are fixed in all dimensions. The distribution can also be incremental, such as harmonically nested arrays, or randomly distributed, such as found with some sparse arrays. In uniform spacing, the two-dimensional lattice of the elements can be square, rectangular, or triangular. Figure 2.3 lists different combinations of elements spacings and array outlines. A planar array is shown in figure 2.4, having N elements in three-dimensional space. Element are located at locations described by the vector $\mathbf{r} = [\mathbf{x}, \mathbf{y}, \mathbf{z}]$, where the n^{th} row of $\mathbf{r}$ contains the location vector of the n^{th} element. If a plane wave illuminates the array, the signal is sampled in space by the antenna elements, and the spatial response of these elements is represented by the steering vector. The steering vector

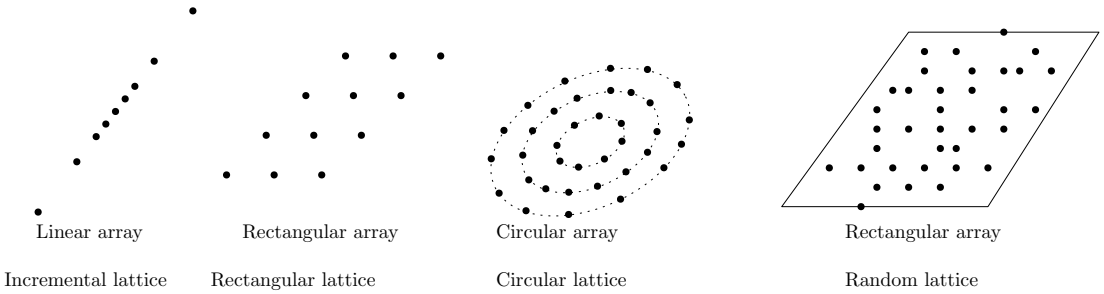

Figure 2.3: Antenna arrays with different combinations of array outlines and element distributions or lattices.

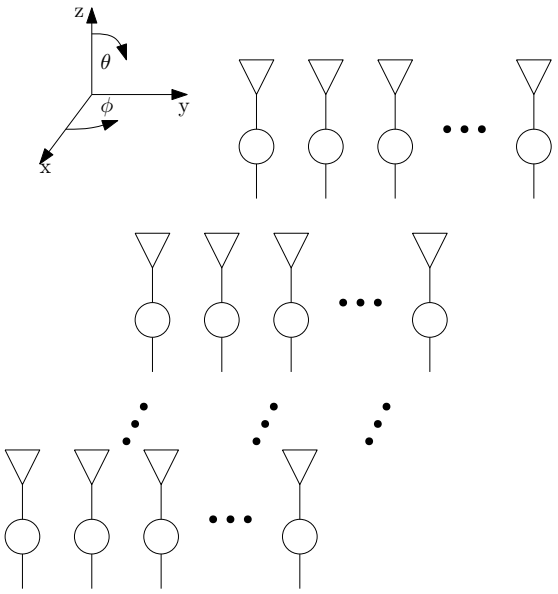

Figure 2.4: A planar antenna array model lying on the x–y plane.

is normally calculated w.r.t. the median element location or the phase centre. The steering vector for an incident signal of frequency ω and angle of arrival (θ, ϕ) is

$$\mathbf{a}(\omega, \theta, \phi) = e^{j(\mathbf{r}\,\mathbf{k})} \ . \tag{2.5}$$

The steering vector becomes

$$\mathbf{a}(\omega, \theta, \phi) = e^{-j\frac{\omega}{c}\mathbf{r}[\sin\theta\cos\phi\ ,\ \sin\theta\sin\phi\ ,\ \cos\theta]^{\mathrm{T}}} \ . \tag{2.6}$$

The arrays studied in this thesis are either linear or planar and have no structure along

the z-axis such that the element location vectors have zero z components. Hence, in this thesis, the location vectors $\mathbf{r}$ are reduced to only x and y components, and the wavenumber vector $\mathbf{k}$ also only requires u and v components.

$$\mathbf{a}(\omega, \mathrm{u}, \mathrm{v}) = e^{-j\frac{\omega}{c}\mathbf{r}[\mathrm{u}\ ,\ \mathrm{v}]^{\mathrm{T}}}\ . \tag{2.7}$$

Each antenna element is attached to a complex weight. The elements' outputs are combined to form the array response or array factor $P(\omega, \theta, \phi)$ as

$$P(\omega, \theta, \phi) = \mathbf{w}^{\mathrm{H}}\mathbf{a}(\omega, \mathrm{u}, \mathrm{v}) = \sum_{n=1}^{N} \mathrm{w}_n\ e^{-j\frac{\omega}{c}\mathbf{r}_n[\mathrm{u}\ ,\ \mathrm{v}]^{\mathrm{T}}}\ , \tag{2.8}$$

where $\mathbf{r}_n$ contains the location vector of the n^{th} element, and $\mathbf{w}^{\mathrm{H}}$ is the Hermitian conjugate of the column vector containing the array weights.

$$\mathbf{w}^{\mathrm{H}} = [\mathrm{w}_1\ ,\quad \mathrm{w}_2\ ,\quad \ldots\ ,\quad \mathrm{w}_N]\ . \tag{2.9}$$

A linear array with a uniform spacing d has the response,

$$P(\omega, \theta) = \mathbf{w}^{\mathrm{H}}\mathbf{a} = \sum_{n=0}^{N-1} \mathrm{w}_n\ e^{-j\frac{\omega}{c}\ (n-\frac{N-1}{2})\ d\ \sin\theta}\ . \tag{2.10}$$

Beam-steering aims to adjust the array weights such that the phases of signals align for a waveform with a particular angle of arrival. In response to beam-steering towards θ_0 and frequency ω_0, the n^{th} element weight shown in equation (2.9) according to [2] is,

$$\mathrm{w}_n = \frac{h(n)}{\sqrt{N}} e^{j\frac{\omega_0}{c}\ (n-\frac{N-1}{2})\ d\ \sin\theta_0} \tag{2.11}$$

where $h(n)$ is a tapering window for a linear array. Substituting (2.11) into (2.10) the beam-steering response of a linear array is,

$$P(\omega, \theta, \phi) = \sum_{n=0}^{N-1} \frac{h(n)}{\sqrt{N}} e^{-j\frac{1}{c}\ (n-\frac{N-1}{2})\ d\ (\omega\sin\theta - \omega_0\sin\theta_0)}\ . \tag{2.12}$$

Equation (2.12) shows that the array response is a function of the difference ($\omega \sin\theta - \omega_0 \sin\theta_0$). The peak response is reached when $\omega \sin\theta = \omega_0 \sin\theta_0$. Up to this point, the signal is assumed continuous in time. In digital signal processing (DSP) the signal is sampled every T_s seconds which corresponds to a sampling rate f_s of $\frac{1}{T_s}$ sample per seconds. For discrete signals, it is common to use the normalized angular frequency $\Omega = 2\pi \frac{f}{f_s}$.

2.3.1 Array Characteristics

Directivity

Directivity is the array ability to concentrate power towards a particular direction. It is the ratio between the power concentration towards the desired direction and the total power propagated through the unit hemisphere around the antenna array, i.e.

$$D(\omega, \theta, \phi) = \frac{|P(\omega_0, \theta_0, \phi_0)|^2}{\frac{1}{4\pi} \int_\theta \oint_\phi |P(\theta, \phi)|^2 d \sin\theta \; d\theta d\phi} \tag{2.13}$$

Substituting the array response P with (2.8) leads to,

$$\begin{aligned} D(\omega, \theta, \phi) =& \frac{\mathbf{w}^{\mathrm{H}} \mathbf{R}_0 \, \mathbf{w}}{\frac{1}{4\pi} \mathbf{w}^{\mathrm{H}} (\int_\theta \oint_\phi \mathbf{a}^2(\theta, \phi) \sin\theta \; d\theta d\phi) \mathbf{w}} \\ =& \frac{\mathbf{w}^{\mathrm{H}} \mathbf{R}_0 \, \mathbf{w}}{\frac{1}{4\pi} \mathbf{w}^{\mathrm{H}} \, 4\pi \mathbf{w}} \\ =& \frac{\mathbf{w}^{\mathrm{H}} \mathbf{R}_0 \, \mathbf{w}}{\mathbf{w}^{\mathrm{H}} \, \mathbf{w}} \; , \end{aligned} \tag{2.14}$$

where $\mathbf{R}_0$ is the sensor covariance matrix obtained at the desired direction as

$$\mathbf{R}_0 = \mathbf{a}(\omega_0, \theta_0, \phi_0) \; \mathbf{a}^{\mathrm{H}}(\omega_0, \theta_0, \phi_0) \; . \tag{2.15}$$

Equation (2.14) describes the directivity of planar arrays, with weights $\mathbf{w}$ and steering vector $\mathbf{a}(\omega, \theta, \phi)$. The equation shows that the array directivity depends on the beamformer, represented by the weights vector $\mathbf{w}$. The equation will be later used in section 2.7 to compare between weights application methods.

Beamwidth

Beamwidth is the angular width of the mainlobe measured in degrees. There are two common definitions of beamwidth: half-power and null-to-null beamwidths. The half-power beamwidth θ_{3db} is the angle between the directions where the array power drops by one-half or 3 dB from its peak value. The null-to-null beamwidth is the angular width between the nearest two nulls in both sides the mainlobe. The half-power beamwidth is more common because it represents the width of the beam that can maintain a relatively high gain. The half-power beamwidth of the mainlobe at angle θ_0 is defined as

$$\theta_{3db} \;=\; \{\min(\theta_2 - \theta_1) \;:\; \theta_2 > \theta_0 > \theta_1, \quad P(\theta_1) = P(\theta_2) = \frac{1}{\sqrt{2}} P(\theta_0)\} \;. \tag{2.16}$$

The definition in (2.16) means that the beamwidth is the minimum difference between two arbitrary angles θ_1 and θ_2 on either side of the beam pointing direction, where the array response drops by $\frac{1}{\sqrt{2}}$ which corresponds to half in power ratio.

Mainlobe and Sidelobes

The highest peak in the array beam pattern is called the mainlobe or mainbeam. For a narrowband arrayoperating over a wideband range, the mainlobe direction varies with frequency. A progressive shift of the mainlobe direction is a result of the non-linear time delay response of phase shifters. Sudden change of mainlobe directios is the result of the rise of the sidelobes above the mainlobe level. Partial wideband structures, like a contiguous subarray and harmonic nesting arrays, can be subjected to either of these variations. In this chapter, the mainlobe is defined as the lobe closer to the desired direction, and beam squinting angle is the angle between the desired direction and the mainlobe.

Beam-steering

Historically, a single antenna is mechanically rotated when changing the beam-pointing direction. Initially, an antenna array was able to change its beam-pointing direction to

a discrete number of angles without mechanical rotation, which is called beam switching [11]. Beam switching has been realized in microwave design using the Blass array [12], the Butler matrix [13] and the Rotman lens [14], or using a sample delay [11] in the digital domain. But the most common form of beam control is beam-steering or delay-and-sum beamforing [15], which is compensating for the propagation delay using phase shift or time delay.

Taper Efficiency

Taper efficiency measures how amplitude taper effects the array directivity. Beam-steering with a uniform amplitude provides the highest directivity, albeit at the cost of high sideobe level. For a uniform array, the taper efficiency is defined similarly to the aperture efficiency [16] as

$$\eta_t = \frac{D(\omega_0, \theta_0, \phi_0)}{D_{\max}(\omega_0, \theta_0, \phi_0)} \ , \tag{2.17}$$

where $D(\omega_0, \theta_0, \phi_0)$ is the directivity and $D_{\max}(\omega_0, \theta_0, \phi_0)$ is the maximum directivity at which $\mathbf{w} = \mathbf{1}$.

2.3.2 Grating Lobes in Uniform Arrays

One of the main design goals in array antenna design is achieving the largest aperture with the smallest number of elements. Directivity increases with the increase in effective aperture and beamwidth is inversely proportional to the effective aperture size [17]. In uniformly spaced array however, if the element spacing exceeds half the wavelength of the highest operating frequency, grating lobes will form within $-\pi/2 \leq \theta \leq \pi/2$ and $-\pi \leq \phi \leq \pi$, which is called the visible region. Figure 2.5 demonstrates the antenna pattern of a 5x5 uniform planar array operating at four times the maximum frequency. Notice that the reduction in array response between the angles 0° and 180° is due to the reduced aperture projection towards the angle of arrival. Figure 2.6 demonstrates the effect of the steering angle, shown here for azimuth angle, and the operating frequency on the location and spacing of grating lobes. In the figure, the black dot represents the mainlobe, the grey dots represent the grating lobes. The green circles represents the visible region where the azimuth angle θ is bound between $-\pi$ and π. The pink

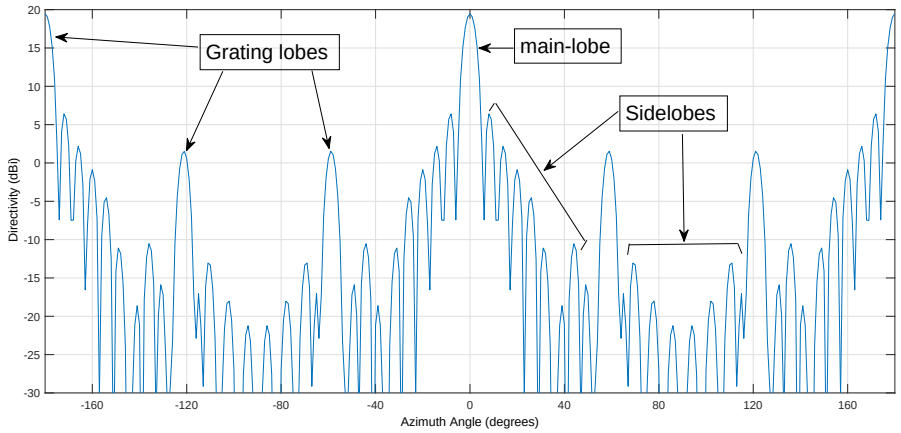

Figure 2.5: Array pattern with a steering angle of 0° operating at $\Omega = 4\pi$. The graph shows the mainlobe, the grating lobes and sidelobes.

circles are images of the visible region that does not manifest in the real observable array response. The effect of the steering angle is to shift the grating lobes, as well as the mainlobe, without affecting the spacing between them. However, the operating frequency changes the grating lobes spacing by expanding the grating lobes, when decreasing the frequency, or compacting them, when increasing the frequency.

Consider a rectangular array with a uniform spacing d lying in the $x - y$ plane. An incident signal with frequency ω from azimuth angle ϕ and elevation angle θ is characterized by the wavenumber vector as

$$\mathbf{k} = -\frac{\omega}{c} \begin{bmatrix} \sin\theta\cos\phi \\ \sin\theta\sin\phi \\ \cos\theta \end{bmatrix} \quad . \tag{2.18}$$

The array factor in response to theprojection of the wavenumber vector $\mathbf{k}$on the u–v space, due to zero component of $\mathbf{r}$ in the z axis, is

$$P(\omega,\theta,\phi) = \sum_{n_x=0}^{N_x-1}\sum_{n_y=0}^{N_y-1} \mathrm{w}[n_x,n_y]e^{-j\mathbf{r}(n_x,n_y)\mathbf{k}_{uv}} \ , \tag{2.19}$$

where $\mathbf{r}(n_x,n_y)$ and $\mathrm{w}[n_x,n_y]$ are the the location vector and the weight of the sensor

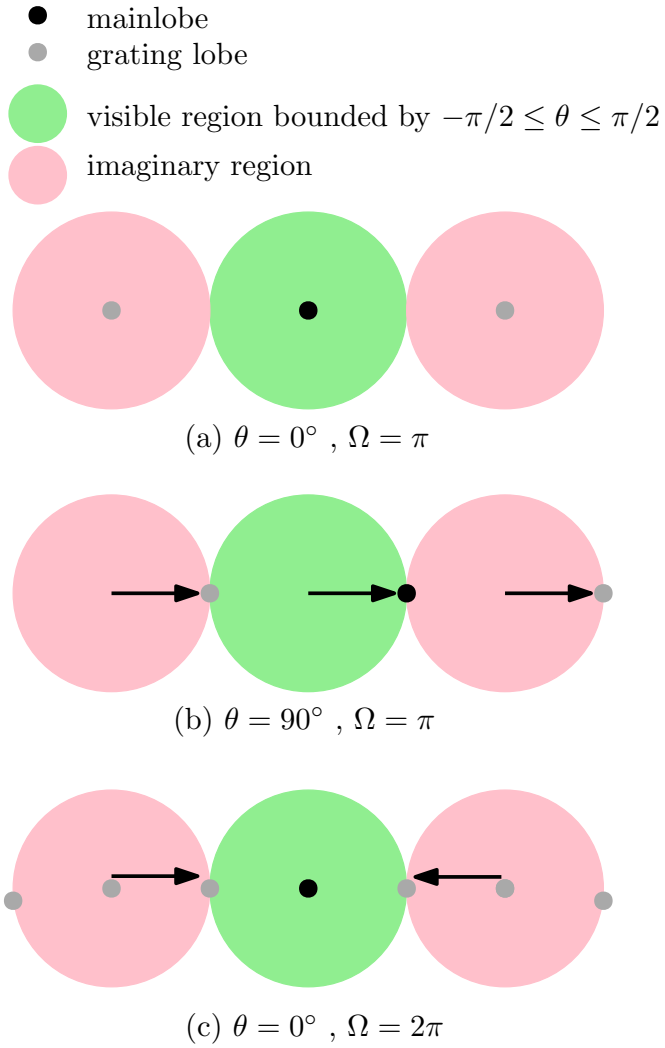

(a) $\theta = 0^\circ$, $\Omega = \pi$

(b) $\theta = 90^\circ$, $\Omega = \pi$

(c) $\theta = 0^\circ$, $\Omega = 2\pi$

Figure 2.6: A demonstration of the effect of steering angle and frequency on the grating lobes locations. (a) The array is steered to boresight $\theta = 0^\circ$ and the maximum frequency which is half the Nyquist frequency $\Omega = \pi$. (b) The array is steered to $\theta = 90^\circ$ and the maximum frequency $\Omega = \pi$. (b) The array is steered to boresight $\theta = 0^\circ$ but at twice the maximum frequency $\Omega = 2\pi$.

with indexes n_x and n_y. Notice that $\mathbf{r}(n_x, n_y)$ is the n^{th} row of the location matrix introduced in (2.6). Also notice that the third term component of the location vector is zero due to structure of the array in the z axis. For a square and symmetric array with a uniform element spacing d, the location of the element with indexes $(n_x\ ,\ n_y)$ is

$$\mathbf{r}(n_x, n_y) = d\left[n_x - \frac{N_x - 1}{2}\ , n_y - \frac{N_y - 1}{2}\ , 0\right]\ , \tag{2.20}$$

i.e. the array is centred in the origin. The beamformer can shape or steer the array response, but it cannot reduce grating lobe levels or separation w.r.t. the main lobe. For a delay-and-sum beamformer, the array is steered towards the direction $\mathbf{k}_0(\omega_0, \theta_0, \phi_0)$ and the array factor in (2.19) simplifies to

$$P(\omega, \theta, \phi) = \frac{1}{\sqrt{N_x\ N_y}} \frac{\sin(\frac{1}{2}\mathbf{r}_{\max}^{\mathrm{H}} \Delta\mathbf{k})}{\sin(\frac{1}{2}\mathbf{r}_{\min}^{\mathrm{H}} \Delta\mathbf{k})}\ , \tag{2.21}$$

where $\Delta\mathbf{k} = \mathbf{k} - \mathbf{k}_0$, $\mathbf{r}_{\min} = [d, d, 0]$ and $\mathbf{r}_{\max} = d[N_x, N_y, 0]$. The array response is periodic w.r.t. wave number vector $\Delta\mathbf{k}$ with period $\frac{2\pi}{d}$. As a result, the grating lobes are located at the zeros of the denominator in (2.21), for $\Delta\mathbf{k} = p\frac{2\pi}{d}\ \ \forall\ p \in \mathbb{Z}$ in the direction of both x- and y-axes. To avoid grating lobes, the zeros of the response denominator should be outside the visible region bounded by $-\pi/2 \leq \theta \leq \pi/2$ and $-\pi \leq \phi \leq \pi$ or $-\frac{\omega}{c} \leq \Delta\mathbf{k}(\omega, \theta, \phi) \leq \frac{\omega}{c}$. For a wideband uniform array, the manifestation of grating lobes in the visible region limits its upper operating frequency.

2.4 Wideband Array Antenna

Narrowband array structures have a complex-valued weight per element in order to facilitate a phase shift. But when the operating bandwidth increases, the beam-pointing direction starts to squint and the level of the sidelobes increases [2, p. 31]. A time delay unit, which is utilised in wideband and partial wideband arrays as will be defined in the next section, can compensate for the propagation delay irrespective of the wavelength. Alternatively, the signal can be sampled in time to apply temporal filtering. Temporal filtering can be implemented using finite impulse response (FIR) or infinite impulse response (IIR) filters. It can also be implemented using an additional dimension of elements provided that it is not perpendicular to the direction of propagation. This structure is called a sensor delay line, and it uses two-dimensional arrays to steer or scan in azimuth while using the elevation dimension for spectral processing [3, 18].

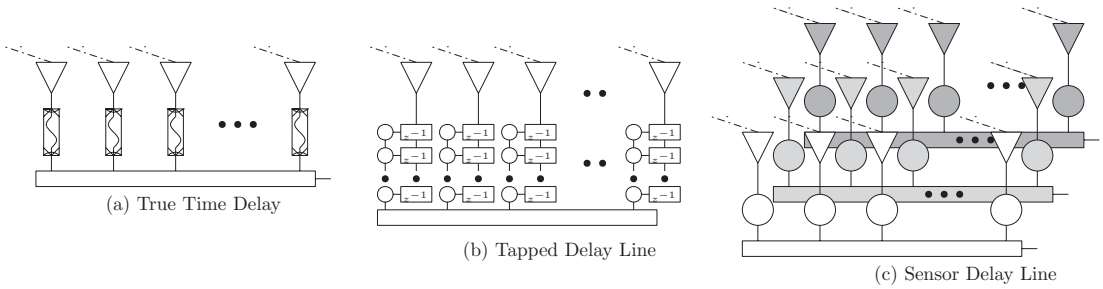

Figure 2.7: Three examples of a wideband linear array. (a) Elements with time delay units. (b) Elements with tapped delay line to apply temporal filtering. (c) Sensor delay line architecture where the elevation angle is fixed.

2.4.1 Wideband Architectures

The narrowband antenna array's reliance on a phase shifter means that the signal delay introduced in each element is frequency dependent. Wideband operation requires wideband weights which have a linear phase of the form,

$$\mathbf{w} = |\mathbf{w}|e^{-j\Omega\tau} \,, \tag{2.22}$$

where $|\mathbf{w}|$ is the amplitude tapering and τ is the propagation delay vector. The definition of wideband is relative to the antenna architecture and the desired performance. But generally a fractional banwidth $\frac{\Delta f}{f_0}$ of 0.25 is considered broadband according to [19], where Δf is the bandwidth and f_0 is the centre frequency. Extending the antenna array bandwidth can be achieved using either a true time delay module [20, 21], a tapped delay line (TDL) [22, 23], or a sensor delay line [18, 24, 25]. Time delay units (TDU) are photonic-based or subband transmission lines. Tapped delay lines are realized mainly in the digital domain and allow the application of Finite Impulse Response (FIR) or frequency selective filtering. Figure 2.7 shows the three types of wideband arrays. Figure 2.7 shows the three types of wideband weights that can be applied to array elements, as in the case of wideband arrays, or subarray elements, as in the case of partial wideband array. This thesis utilises the time delay unit and the tapped delay line weights while the sensor delay line is only shown for completeness. The analog array in figure 2.7(a) is utilising time delay units for each element to compensate for

the propagation delay. The digital array in figure 2.7(b) implements a representation of the time delay unit in the digital domain. The narrowband planar array in figure 2.7(c) uses the planar array as a one-dimensional wideband array.

Tapped Delay Line (TDL) Architecture

The tapped delay line is a means to apply spectral filtering and weighting. TDL processes the signals purely in the time domain, and its response is independent of the angle of arrival. TDL is used to implement FIR-based data-independent beamforming [26] or adaptive algorithms [1]. TDL can also realize an IIR-based beamforming [27] or Fast Fourier Transform (FFT) [28].

Sensor Delay Line (SDL) Architecture

A sensor delay line is applied to a narrowband planar array to substitute the elevation angle control for a frequency-invariant response. A planar array can be narrowband with full control over azimuth and elevation, or wideband with azimuth control only, which offers a functional flexibility [3, 18].

2.4.2 Subarray Model

A subarray is a group of elements within an array that are accessible through one port. The individual elements are not accessible and are not necessarily exclusive. This means that elements can be shared between several subarrays and such an architecture is called an overlapped subarray [2]. The subarray architecture offers fewer processing degrees of freedom than a fully digital array. Control over the elements weighting is still possible, with the exception of a limited field of view (LFOV) subarray [29, 30].

The subarray structure allows for two-tier weighting to enhance bandwidth, such as the contiguous subarray, or to reduce the number of weights as in the LFOV subarrays. The architecture of narrowband subarrays followed by a time delay or a digital filter is referred to as the contiguous subarray, which has been addressed in [31–34]. Subarray architectures offer the following advantages:

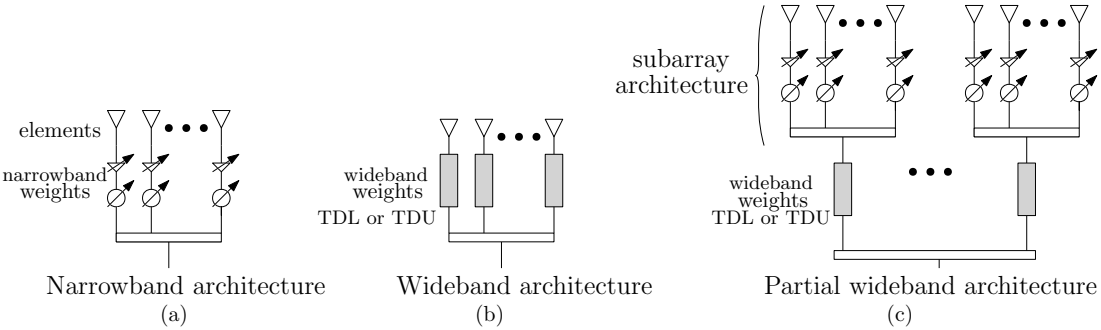

Figure 2.8: The array architectures studied in this thesis. (a) The narrowband architecture where elements are connected to narrowband weights, (b) the wideband architecture where all array elements are connected to a TDL or TDU wideband weights, (c) the partial wideband architecture consisting of multiple narrowband arrays as subarrays, and wideband weights, either TDL or TDU, attached to the subarrays' outputs.

- Separation of array performance aspects such as beamwidth, directivity, and sidelobe level, from processing requirements such as interference suppression, noise cancellation, and adaptive beamforming. The number of digital channels can be reduced without compromising the beam pattern characteristics.

- Subarrays can be frequency-allocated, as in the overlapped nested array, to provide a wideband coverage.

- The subarray can be modular in terms of the distribution network design, microwave filtering and conditioning. Modularity can reduce complexity and cost.

- Subarrays are easier to assemble and interface because they have fewer ports than a full array.

Figure 2.8 shows the three array architectures discussed in this thesis. The narrowband architecture is where elements are connected to complex weights consisting of gain control and phase shifts. Although the gain control is wideband, the phase shift introduces a time delay that changes with frequency, as will be explained in chapter 4. The wideband architecture has a similar configuration to the narrowband array. But the array can be either a fully digital array where the elements are digitised and processed using TDL filter, or the complex weights are replaced with a TDU which

can implement a frequency-independent time delay. The partial wideband architecture uses the narrowband array as a subarray, and combines the subarrays' outputs after applying wideband weights identical to those used in the wideband architecture.

A partial wideband array consists of N sensors distributed in the x–y plane, followed by narrowband weights. The partial wideband array contains M subarray. Each subarray consists of K sensors. The sensors within the subarray are weighted and combined into one output. If the wideband weights are TDUs, then the required time delay for each subarray is compensated using a scalar time delay value in the TDU without further processing or gain control. If the wideband weights are TDLs, then the partial wideband array needs a mathematical model to represent this two-tier weighting. Each subarray is then followed by a TDL of length J. The subarray spatial steering is a column vector $\mathbf{a}_s(\Omega, \theta, \phi)$ which is derived from equation (2.6) as

$$\mathbf{a}_s(\Omega, \theta, \phi) = e^{-j\frac{\Omega}{c}\mathbf{r}\begin{bmatrix} \sin\theta\cos\phi \\ \sin\theta\sin\phi \end{bmatrix}}, \tag{2.23}$$

where $\mathbf{r}$ is the sensor location matrix where each row contains the $x-y$ coordinated of a sensor. The temporal delay vector $\mathbf{a}_t(\Omega)$ that represents the TDL transfer function is

$$\mathbf{a}_t(\Omega) = e^{-j\Omega[0:J-1]^{\mathrm{T}}} . \tag{2.24}$$

The entire steering vector $\mathbf{a}(\Omega, \theta, \phi)$ is the Kronecker product of the spatial steering vector (2.23) and the temporal sample delay (2.24),

$$\mathbf{a}(\Omega, \theta, \phi) = \mathbf{a}_t(\Omega) \otimes \mathbf{a}_s(\Omega, \theta, \phi) . \tag{2.25}$$

The resulting steering representation is a column vector of length KMJ.

The m^{th} subarray has a complex weights column vector $\mathbf{w}_m$ attached to its K sensors, and a TDL weights column vector $\mathbf{v}_m$ attached to its J tabs. Similar to (2.25), the entire array weights are the Kronecker product of the subarray TDL weights and

the subarrays elements weights, i.e.

$$\mathbf{w} = \begin{bmatrix} \mathbf{v}_1 \otimes \mathbf{w}_1 \\ \vdots \\ \mathbf{v}_M \otimes \mathbf{w}_M \end{bmatrix}, \tag{2.26}$$

which is a column vector of length KMJ. Finally, the array response is obtained by substituting the modified steering and weight vectors in (2.10) as $P(\Omega, \theta, \phi) = \mathbf{w}^{\mathrm{H}}\, \mathbf{a}$.

Each K rows of the array weights in (2.26) are linearly dependent. This prevents the use of many fixed and adaptive beamforming techniques without proper modelling of the steering vector and weights. Finally, it is useful to define a subarray ratio to reflect the ratio between the number of subarrays and the total number of elements. For example, an array containing 16 elements and 4 subarrays has a subarray ratio of 4:16.

2.4.3 Beamspace Adaptive Beamforming

Beamspace beamforming is the formation of multiple array outputs or beams, and the processing of the signals derived from those beams to meet a specific optimization criteria [11]. In the architectures described in figure 2.8, each array element is attached to a single narrowband weight. This limits the degrees of freedom of the adaptive processing or wideband beamforming that can be ut at the subarray level. However, in beamspace processing, multiple beams can be produced by applying a multiple element-level beamformers that are independent from each other. Figure 2.9 shows a beamspace array consisting of Q beam outputs. Each beamformer independently steers the angle and the frequency while having access to all array elements.

In adaptive beamspace processing, one beam is steered towards the main source and is called quiescent pattern [11]. The remaining beams, called the auxiliary beams, are steered towards the interfering sources to enable adaptive filtering such as noise cancellation and interference rejection. For a beamspace beamformer containing N

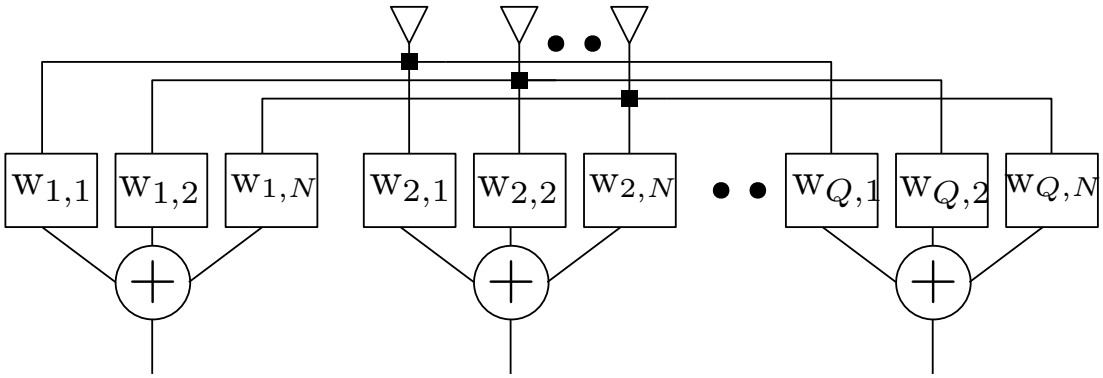

Figure 2.9: A generic structure for a beamspace array. Beamspace beamformers contain narrowband weights and are independently steered to produce multiple beams.

elements and Q beam processors, the quiescent beam is

$$P(\Omega, \theta, \phi) = \mathbf{w}_q^{\mathrm{H}}\ \mathbf{a}_s(\Omega_0, \theta_0, \phi_0), \tag{2.27}$$

where $\mathbf{w}_q$ is the row vector containing the narrowband weights steered towards the signal of interest, and $\mathbf{a}_s(\Omega_0, \theta_0, \phi_0)$ is the spatial steering vector for the direction and frequency of the signal of interest. Similarly, the array response of the for the a^{th} auxiliary beam is

$$P(\Omega, \theta, \phi) = \mathbf{w}_a^{\mathrm{H}}\ \mathbf{a}_s(\Omega, \theta, \phi)\ \ , a = 1, \cdots, Q-1. \tag{2.28}$$

The simplest form of the adaptive beamspace processing is the generalised sidelobe canceler (GSC) which has one quiescent and one auxiliary beam processors. The quiescent beamformer has fixed weights vector $\mathbf{w}_q$ which is steered towards the signal of interest. The auxiliary part consists of a fixed blocking matrix $\mathbf{B}$ to remove the signal of interest by placing a null at its direction, i.e. $\mathbf{B}^{\mathrm{H}}\mathbf{a}(\Omega_0, \theta_0, \phi_0) = \mathbf{0}$, and an adaptive weights vector $\mathbf{w}_a$ to minimize the output power while maintaining a unit response towards the desired direction. The resulting weight of the GSC is

$$\mathbf{w}_{gsc} = \mathbf{w}_q - \mathbf{B}\mathbf{w}_a\ . \tag{2.29}$$

2.5 Wideband Beamforming

The beamformer is a form of discrete spatial filtering. It is the weighted combination of the incident signals on the array elements for a receiving array. Beamforming can perform more than just beam-steering towards the desired direction. Provided that sufficient degrees of freedom are available, beamforming can generate multiple beams towards sources of interest, or form multiple nulls towards interferences. More specifically, the number of controllable sensors defines the combined number of beams and nulls that can be formed, while the aperture size limits the beamwidth of the beam(s) [35]. In this section, the common wideband beamforming techniques will be introduced. These are designed using least squares, the eigenfilter method and convex optimisation.

2.5.1 Least Squares

The least squares solution is an unconstrained optimisation technique [36] of the form

$$\underset{\mathbf{x}}{\text{minimize}} \; |\mathbf{A}\mathbf{x} - \mathbf{b}|^2 \; . \tag{2.30}$$

Recall from (2.8) that the array response can be represented in vector format as the product of weights and the steering vector. The goal is to minimize the deviation between the array response $\mathbf{w}^{\mathrm{H}}\mathbf{a}(\Omega, \theta, \phi)$, and the desired pattern $P_d(\Omega, \theta, \phi)$. The least squares approach minimizes the absolute squared deviation of the array response from the desired pattern, called the error. The error at a frequency Ω, an elevation angle θ and an azimuth angle ϕ is given by

$$e(\Omega, \theta, \phi) = P_d(\Omega, \theta, \phi) - \mathbf{w}^{\mathrm{H}}\mathbf{a}(\Omega, \theta, \phi) \; . \tag{2.31}$$

The squared error is obtained by squaring and expanding the brackets in (2.31). The squared error is decomposed into three terms,

$$\begin{aligned} e^2(\Omega,\theta,\phi) &= (P_d(\Omega,\theta,\phi) - \mathbf{w}^{\mathrm{H}}\mathbf{a}(\Omega,\theta,\phi))(P_d(\Omega,\theta,\phi) - \mathbf{w}^{\mathrm{H}}\mathbf{a}(\Omega,\theta,\phi))^* \\ &= |P_d(\Omega,\theta,\phi)|^2 \; + \; \mathbf{w}^{\mathrm{H}}\mathbf{R}(\Omega,\theta,\phi)\mathbf{w} \\ &\quad - |P_d(\Omega,\theta,\phi)\mathbf{a}^{\mathrm{H}}(\Omega,\theta,\phi)\mathbf{w}| \; - \; |P_d^*(\Omega,\theta,\phi)\mathbf{w}^{\mathrm{H}}\mathbf{a}(\Omega,\theta,\phi)| \; , \end{aligned} \tag{2.32}$$

where $\mathbf{R}(\Omega,\theta,\phi) = \mathbf{a}(\Omega,\theta,\phi)\ \mathbf{a}^{\mathrm{H}}(\Omega,\theta,\phi)$ is the steering matrix. The cost function ξ is the summation of the error squares over space and frequency.

$$\xi = \int_{\Omega}\int_{\theta}\int_{\phi} h(\Omega,\theta,\phi)e^2(\Omega,\theta,\phi)\phi d\theta d\Omega \; , \tag{2.33}$$

where $h(\Omega,\theta,\phi)$ is a weighting function that emphasis certain frequency bands or angle sectors. For a planar array lying on the $x-y$ plane, the pattern is plane-symmetric around $z = 0$. Hence it is sufficient to evaluate the cost function over the upper hemisphere where $\theta = [0, \pi/2]$. Substituting (2.32) into the error function results in

$$\begin{aligned} \xi &= \int_{\Omega}\int_{\theta=0}^{\pi/2}\oint_{\phi=-\pi}^{\pi} h(\Omega,\theta,\phi)e^2(\Omega,\theta,\phi)d\phi d\theta d\Omega \\ &= \; \mathbf{w}^{\mathrm{H}}\ \hat{\mathbf{R}}_{\mathrm{ls}}(\Omega,\theta,\phi)\ \mathbf{w} - \ \mathbf{w}^{\mathrm{H}}\ \hat{\mathbf{d}}(\Omega,\theta,\phi) \\ &\quad - \hat{\mathbf{d}}^{\mathrm{H}}(\Omega,\theta,\phi)\ \mathbf{w} \; - \; \mathbf{w}^{\mathrm{H}}\ \hat{\mathbf{d}}(\Omega,\theta,\phi) \\ &\quad + \int_{\Omega}\int_{\theta=0}^{\pi/2}\oint_{\phi=-\pi}^{\pi} h(\Omega,\theta,\phi)|P_d(\Omega,\theta,\phi)|^2 d\phi d\theta d\Omega \; . \end{aligned} \tag{2.34}$$

The Hermitian matrix $\hat{\mathbf{R}}_{\mathrm{ls}}$ is the summation of the steering matrices over all bands and directions at which the desired pattern $P_d(\Omega,\theta,\phi)$ is defined.

$$\begin{aligned} \hat{\mathbf{R}}_{\mathrm{ls}}(\Omega,\theta,\phi) &= \int_{\Omega}\int_{\theta}\oint_{\phi} h(\Omega,\theta,\phi)\mathbf{a}(\Omega,\theta,\phi)\ \mathbf{a}^{\mathrm{H}}(\Omega,\theta,\phi)d\phi d\theta d\Omega \\ \hat{\mathbf{d}}(\Omega,\theta,\phi) &= \int_{\Omega}\int_{\theta}\oint_{\phi} h(\Omega,\theta,\phi)|P_d(\Omega,\theta,\phi)\mathbf{a}^{\mathrm{H}}(\Omega,\theta,\phi)|d\phi d\theta d\Omega \end{aligned} \tag{2.35}$$

The cost function is quadratic w.r.t. $\mathbf{w}^{\mathrm{H}}$, which is a differentiable and a convex function. The minimum point can be found by differentiating the cost function w.r.t. $\mathbf{w}^{\mathrm{H}}$ then

finding the null space that represents the minimum value [15].

$$\frac{\partial \xi}{\partial \mathbf{w}^{\mathrm{H}}} = \hat{\mathbf{R}}_{\mathrm{ls}}(\Omega, \theta, \phi) \quad \mathbf{w} \quad - \quad \hat{\mathbf{d}}(\Omega, \theta, \phi) = 0 \; . \tag{2.36}$$

Hence the optimum weights that minimize the sum of the squared errors is

$$\mathbf{w}_{opt} = \hat{\mathbf{R}}_{\mathrm{ls}}^{-1}(\Omega, \theta, \phi) \; \hat{\mathbf{d}}(\Omega, \theta, \phi) \; . \tag{2.37}$$

The simplest representation of the desired response $P_d(\Omega, \theta, \phi)$ is binary, with a unit value over the passband in both spectral domain at which $\Omega \in [\Omega_L, \Omega_H]$, and spatial domains at (θ_0, ϕ_0), and zero value over stopband regions [37, 38], i.e.

$$P_d = \begin{cases} 1 & \text{if } (\Omega \in [\Omega_L, \Omega_H]) \cap (\theta \in \theta_0) \cap (\phi \in \phi_0) \\ 0 & \text{otherwise} \end{cases} \; , \tag{2.38}$$

where Ω_L and Ω_H are the lower and upper frequency limits respectively. When the desired beam pattern is defined as in (2.38), the steering matrix integral $\hat{\mathbf{R}}_{\mathrm{ls}}$ is defined over all directions and frequencies, while $\hat{\mathbf{d}}$ is only defined over the passband region, because of multiplication with P_d, as

$$\hat{\mathbf{d}}(\Omega, \theta_0, \phi_0) = \int_{\Omega_L}^{\Omega_H} h(\Omega, \theta_0, \phi_0) |\mathbf{a}^{\mathrm{H}}(\Omega, \theta_0, \phi_0)| d\Omega \; . \tag{2.39}$$

The definition of $\hat{\mathbf{d}}$ in (2.39) does not require the desired response P_d because it has been already used to define its integration limits i.e. Ω_H and Ω_L.

2.5.2 Eigenfilter

The eigenfilter approach was introduced in 1987 as an extension of the least squares approach to FIR filter design [39]. The eigenfilter approach has been applied to 1-Dimensional FIR filter design [40], 2-D FIR filters [41, 42], IIR Filters [43], and sensor arrays [23]. The eigenfilter approach requires the calculation of a Hermitian, semi-definite matrix instead of the steering matrix inversion required in least squares method.

The eigenfilter approach can also include additional spatial and spectral constraints [37].

Similar to the least squares definition, the eigenfilter cost function is the sum of the squared deviation from the normalized desired response,

$$\begin{aligned}\xi_g &= \int_\Omega \int_\theta \oint_\phi h(\Omega,\theta,\phi)\left|\frac{\mathbf{w}^{\mathrm{H}}\mathbf{a}(\Omega_0,\theta_0,\phi_0)}{P_d(\Omega_0,\theta_0,\phi_0)}P_d(\Omega,\theta,\phi) \;-\; \mathbf{w}^{\mathrm{H}}\mathbf{a}(\Omega,\theta,\phi)\right|^2 \; d\phi d\theta d\Omega \quad (2.40)\\ &= \quad \mathbf{w}^{\mathrm{H}}\,\hat{\mathbf{R}}_g\,\mathbf{w}\;,\end{aligned}$$

where $\hat{\mathbf{R}}_g$ is defined similar to $\hat{\mathbf{R}}_{\mathrm{LS}}$ in (2.35)

$$\hat{\mathbf{R}}_g = \int_\Omega \int_\theta \oint_\phi h(\Omega,\theta,\phi)\left|\frac{\mathbf{a}(\Omega_0,\theta_0,\phi_0)}{P_d(\Omega_0,\theta_0,\phi_0)}P_d(\Omega,\theta,\phi) \quad - \quad \mathbf{a}(\Omega,\theta,\phi)\right|^2 \; d\phi d\theta d\Omega\;. \quad (2.41)$$

The filter weights are obtained by solving the following optimisation problem [37]

$$\begin{aligned}\underset{\mathbf{w}}{\text{minimize}} \quad & \xi_g \\ \text{subject to} \quad & \mathbf{w}^{\mathrm{H}}\mathbf{w} = 1\;,\end{aligned} \quad (2.42)$$

where the term $\mathbf{w}^{\mathrm{H}}\mathbf{w} = 1$ prevents the trivial solution. The desired pattern $P_d(\Omega,\theta,\phi)$ is normalized by the factor $\frac{\mathbf{w}^{\mathrm{H}}\mathbf{a}(\Omega_0,\theta_0,\phi_0)}{P_d(\Omega_0,\theta_0,\phi_0)}$ so that the error value is zero at the reference frequency and the desired direction. Therefore, (2.42) can be formulated as a Rayleigh quotient [44], i.e.

$$\underset{\mathbf{w}}{\text{minimize}} \qquad \frac{\mathbf{w}^{\mathrm{H}}\,\hat{\mathbf{R}}_g\,\mathbf{w}}{\mathbf{w}^{\mathrm{H}}\mathbf{w}}\;. \quad (2.43)$$

The minimum and maximum values of the cost function in the numerator are reached when the weight vector $\mathbf{w}$ is equal to the eigenvector corresponding to the minimum and maximum eigenvalues of $\hat{\mathbf{R}}_g$ respectively.

The passband–stopband definition of the desired response $P_d(\Omega,\theta,\phi)$ in (2.38) can be utilised here. In addition, a region between the passband and the stopband can be left to allow for the transition of the response from the mainlobe to the sidelobe region. The desired pattern is consequently defined over the passband and stopband regions in

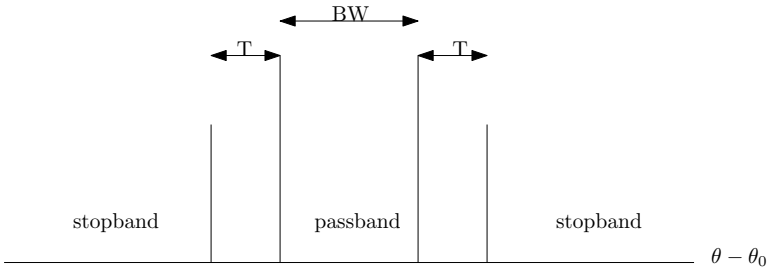

Figure 2.10: A diagram showing passband, stopband and transition regions for the elevation angle θ as an example. The passpand bandwidth is labeled as BW and the transition bandwidth is labeled as T.

both the spectral and spatial domains, but undefined over the transition regions:

$$P_d = \begin{cases} 1 & \text{if } (\Omega \in [\Omega_L, \Omega_H]) \cap (|\theta - \theta_0| \leq \frac{1}{2}\theta_{3db}) \cap (|\phi - \phi_0| \leq \frac{1}{2}\phi_{3db}) \\ 0 & \text{if } (\Omega \in [\Omega_L, \Omega_H]) \cap (|\theta - \theta_0| > \frac{1}{2}\theta_{3db} + \theta_T) \cup (|\phi - \phi_0| > \frac{1}{2}\phi_{3db} + \phi_T) \end{cases} .$$

Here, θ_{3db} and ϕ_{3db} are the half-power elevation and azimuth beamwidths respectively, θ_T and ϕ_T are the width of the transition regions in elevation and azimuth. The desired beam pattern is undefined at these angles and hence the array response is unconstrained in the transition regions. The transition band can be applied in the frequency domain but normally the wide separation between frequency samples provides a sufficient space for a transition. Figure 2.10 illustrated the three regions of constraints in (2.44) for the elevation angle as an example. The cost function $\hat{\mathbf{R}}_g$ can now be split into $\hat{\mathbf{R}}_p$ for the passband and $\hat{\mathbf{R}}_s$ for the stopband regions. The weighting function $h(\Omega, \theta, \phi)$ can be replaced by α for the passband region, and $1 - \alpha$ for the stopband region where $0 \leq \alpha \leq 1$. Now $\hat{\mathbf{R}}_g$ in the passband region is defined as

$$\hat{\mathbf{R}}_p = \alpha \int_\Omega \int_\theta \int_\phi (\mathbf{1} - \quad \mathbf{a}(\Omega, \theta, \phi))(\mathbf{1} - \quad \mathbf{a}(\Omega, \theta, \phi))^{\mathrm{H}} \; d\phi d\theta d\Omega \; , \tag{2.44}$$

where $\mathbf{1}$ is a column vector of the same size as $\mathbf{a}(\Omega, \theta, \phi)$. The stopband cost function is

$$\hat{\mathbf{R}}_s = (1 - \alpha) \int_\Omega \int_\theta \int_\phi \mathbf{a}(\Omega, \theta, \phi)\mathbf{a}^{\mathrm{H}}(\Omega, \theta, \phi) \; d\phi d\theta d\Omega \; . \tag{2.45}$$

Equations (2.44) and (2.45) are the Eigenfilter cost functions for the passband and

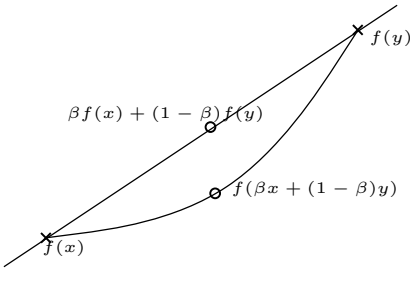

Figure 2.11: The convexity condition of a function f over a period $[x, y]$.

stopband, respectively, when the desired response P_d is defined as $P_d = \mathbf{1}$ for the passbandand and $\mathbf{0}$ for the stopband in (2.41).

2.5.3 Convex Optimisation

The array beam pattern can be designed more flexibly using convex optimisation methods if the problem and the constraints are modelled as convex quadratic or affine functions. Convex optimisation includes linear programming, like the least squares problem described in Section 2.5.1, and non-linear programming like the Quadratically Constrained Quadratic Programming (QCQP) problem. This section uses a combination of linear and quadratic functions to describe the array response.

A convex function f is one that satisfies

$$f(\beta x + (1-\beta)y) \leq \beta f(x) + (1-\beta) f(y) \quad \forall x, y \in R^n,\ \beta \leq 1\ . \tag{2.46}$$

A function f is convex over a period $[x, y]$ if all its values are on or below the affine line connecting $[f(x), f(y)]$ as shown in Figure 2.11. The standard convex optimisation problem of a convex objective function and constraints [36] is

$$\begin{aligned} &\text{minimize } f_0(x) && \\ &\text{subject to } f_i(x) \leq b_i && i = 1, \cdots, m \end{aligned} \tag{2.47}$$

The look direction is intended to attain the highest directivity or power concentration. The array response can be constrained to the unit value $\mathbf{w}^{\mathrm{H}}\mathbf{a}(\Omega_0, \theta_0, \phi_0) = 1$. If

the beam pattern is normalized w.r.t. the maximum directivity, then the unit value is the highest value as a constraint. A more relaxed constraint is required to allow ripple variations in the mainlobe region if it is defined over a range of angles rather than a single direction. This relaxation can be achieved by the Euclidean ball [36] where the equality is replaced by an inequality constraints.

$$|\mathbf{w}^{\mathrm{H}}\mathbf{a}(\Omega_0, \theta, \phi) - 1| \leq \gamma_{ml} \tag{2.48}$$
$$\gamma_{ml} = 10^{\sigma_r/20} ,$$

where γ_{ml} is a small positive value that allows spatial or spectral variations in power decibels σ_r, if more than one point is sampled in the mainlobe.

2.6 Applying Beamforming on Subarrays

Consider partial wideband arrays described in Section 2.4.2, the beamforming phase weighting is divided between the element-level phase shifters and subarray-level time delays. The three possible ways to distribute the phase of the beamforming weights between the elements and the subarrays are:

1. Location alignment.
2. Segregated subarrays.
3. Phase separation.

These will be discussed below in turn.

2.6.1 Location Alignment

In the location alignment approach, the steering vector is replaced by a virtual steering vector so that the subarrays phase centres are aligned with the desired direction. The virtual steering vector reflects the electronic response of the subarray instead of the physical one measured at the elements. The mth subarray virtual steering vector is calculated by replacing the location vector of its elements $\mathbf{r}_m$ with a vector $\hat{\mathbf{r}}_m$ defined

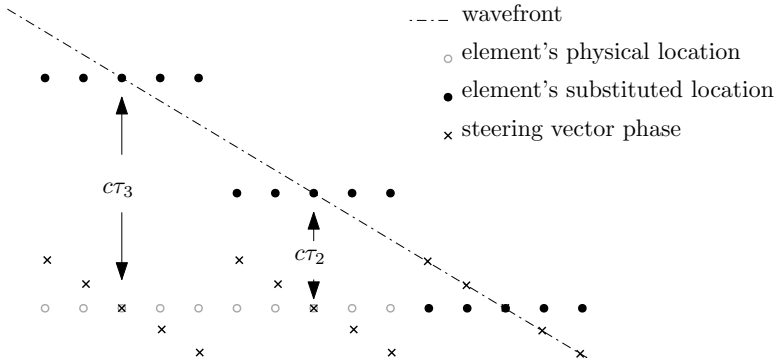

Figure 2.12: Location alignment of the subarrays along the plane of the wavefront .

as

$$\hat{\mathbf{r}}_m = \mathbf{r}_m - c\,\boldsymbol{\tau}_m(\theta_0, \phi_0)\ . \tag{2.49}$$

Here $\boldsymbol{\tau}_m(\theta_0, \phi_0)$ is the propagation delay vector experienced by the elements of the m^{th} subarray w.r.t. the desired direction (θ_0, ϕ_0) and $\mathbf{r}_m$ is the physical locations of the m^{th} subarray elements. Figure 2.12 illustrates how the steering vector uses the modified elements locations to include the subarray time delay.

2.6.2 Segregated Subarrays

In the segregated subarrays approach, wideband beamforming is applied to the subarrays separately. Beamforming is applied locally to the subarray and if subarrays are identical, then the elements weighting is identical to all subarrays. The subarrays have a wider bandwidth than the full array due to the smaller aperture size. The subarrays outputs are combined using time delay or TDL-based alternative like a fractional delay filter [45].

2.6.3 Phase Separation

In the phase separation approach, wideband beamforming is applied to the entire array. Then the phase term of the beamformer weights $\boldsymbol{\Phi}(\mathbf{w})$ is divided between the subarray-level time delay $\Omega\,\boldsymbol{\tau}_m$, and the element-level phase shift$(\boldsymbol{\Phi}(\mathbf{w}) - \Omega_0\,\boldsymbol{\tau}_m)$ as follows:

$$\boldsymbol{\Phi}(\mathbf{w}_m) = (\boldsymbol{\Phi}([\mathbf{w}]_m) - \Omega_0\boldsymbol{\tau}_m) + \Omega\boldsymbol{\tau}_m \tag{2.50}$$

where $[\mathbf{w}]_m$ is the initial beamforming weights assigned to the m^{th} subarray. The propagation delay to the phase center of each subarray is compensated by the subarray's TDU or TDL. This propagation delay is deducted from the elements' phase shifts. For example, If the phase center of the subarray is experiencing a propagation delay of 2.5 T_s w.r.t. an arbitrary steering angle, then the k^{th} element's weight within this subarray will be $\mathbf{w}(k) - e^{j2.5T_s\Omega}$ where $\mathbf{w}(k)$ is the complex valued weight assigned by the narrowband beamformer to the k^{th} element.

2.7 Comparison Between Subarray Beamforming Approaches

The wideband beamforming techniques described in 2.5.1 and 2.5.2 have been proposed for narrowband array structures. The convex optimisation technique in Section 2.5.3 is an iterative technique and can optimise the elements and the subarrays weighting separately. In this section we will explore the three different approaches to implement wideband beamforming on the partial wideband array. Eigenfilter is a suitable wideband beamformer to be used for the comparison, as it is a representative of the least squares beamformer because they are both derived from the same error definition. Convex optimisation bypasses the need to allocate the weights between the element level and the subarray level because both the elements weights and the subarrays weights can be optimisation variables.

In this comparison, the eigenfilter is applied to a 32-element uniform linear array. In addition to the narrowband and the wideband arrays, three different partial wideband configurations are used: 4 subarrays containing 8 elements each or 4:32 ratio, 8 subarrays with 4 elements each or 8:32 ratio, and an extreme case of 16 subarrays with 2 elements each or 16:32 subarray ratio. The subarray ratio is $M : K$ where M is the number of subarrays and K is the total number of elements as defined in Section 2.4.2. The beamformer frequency starts from zero frequency to half the spatial sampling frequency w.r.t. the elements spacing. The desired direction of the linear array is 45°. The desired response is defined as a passband-stopband as in equation (2.44). The mainlobe or passband region is set to be 3° wide. The transition region is 10° on each

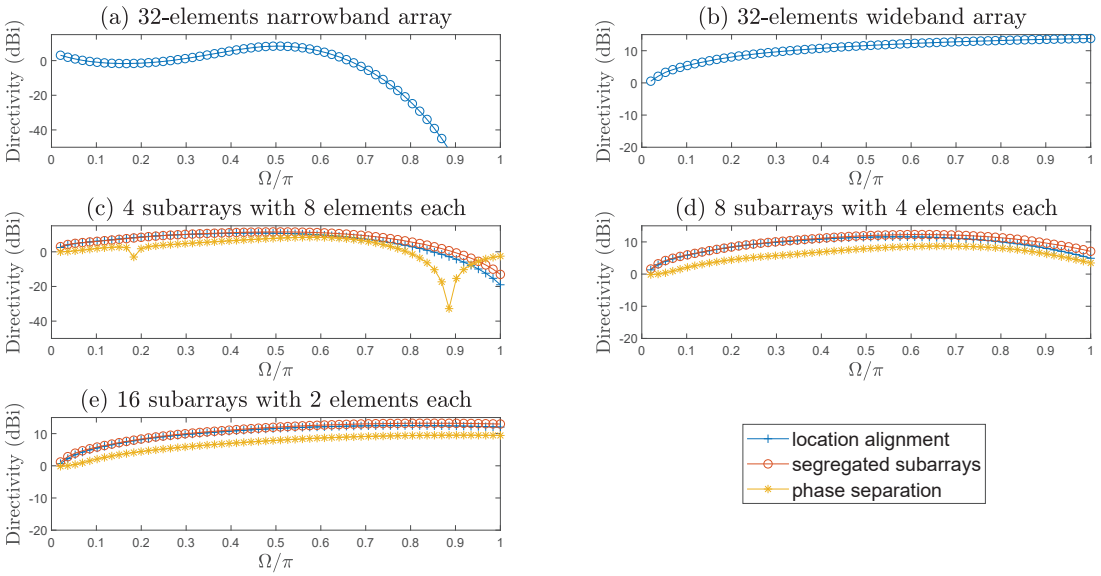

Figure 2.13: Directivity of a uniform linear array of 32 elements processed with wideband eigenfilter applied using the three application approaches described in section 2.6, for five different array architectures:(a) Narrowband array, (b) wideband array, and three partial wideband arrays in (c),(d) and (e).

side of the mainbeam. The sidelobe suppression starts 11° from the desired direction and is sampled with 1° spacing. In the following sections, the three subarray beamforming methods are examined in terms of directivity, beamwidth, beam squinting, and sidelobe level.

2.7.1 Subarray Directivity Comparison

Figure 2.13 shows that the segregated subarray approach maintains the highest directivity, which is defined in section 2.3.1, among all partial wideband structures. This is due to the relatively flatter amplitude tapering applied by individual subarray beamformer compared to the combined partial wideband array beamformer in the location alignment and phase separation methods. Notice that the subarray weighting application approaches do not apply to narrowband and wideband architectures in figure 2.13(a) and (b) respectively. The narrowband array has lowest directivity except at the center frequency which is the design frequency of the narrowband weights. While the wideband array has the highest directivity among other arrays.

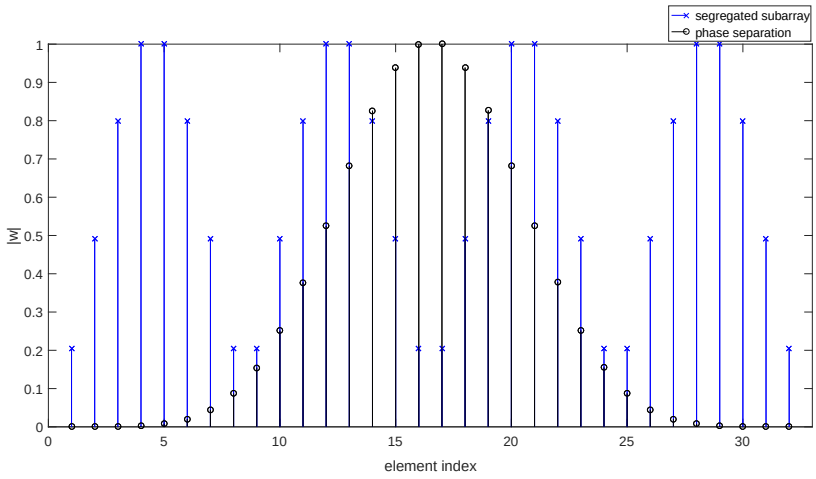

Figure 2.14: Eigenfilter amplitude weighting obtained using phase separation and segregated subarray approached for the partial wideband array with 4:32 subarrayratio.

Figure 2.14 shows the normalized amplitude weighting of the partial wideband array constructed with the 4:32 subarrayratio. The weighting of the phase separation method shown in figure 2.14 has a taper efficiency, — elaborated in Section 2.3.1 — of 0.42 while the segregated subarray has achieved 0.81. The location alignment approach has the same amplitude taper as the phase separation approach hence it is not shown here.

Notice that the directivity is unaffected by the subarray ratio, more clearly around the centre of the band. However, the flatness of the directivity across the frequency band degrades for lower subarray ratios. The directivity degrades further from the centre frequency due to drifting in elements phase shifts with frequency.

In theory, the bandwidth of a subarray that utilises true-time delay increases by a factor of M where M is the number of subarrays, compared to a narrowband array of the same size [34]. The directivity graphs in figure 2.13 show an improved directivity by 3 dB for every time the subarray ratio doubles, except at the lower frequency end of the 16:32 subarray. The low directivity near the zero frequency is because the signal wavelength is very large compared to the element spacing. Therefore, the array aperture size is very small w.r.t. the low frequency wavelength.

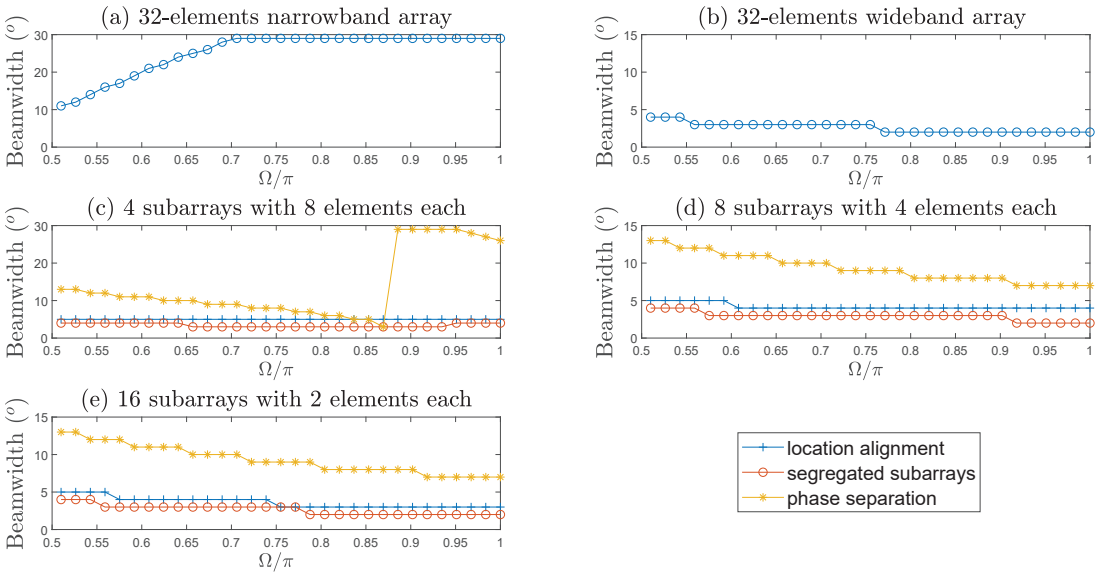

Figure 2.15: Beamwidth of a uniform linear array of 32 elements processed with wideband eigenfilter applied using the three application approaches described in section 2.6, on five different array architectures:(a) Narrowband array, (b) wideband array, and three partial wideband arrays in (c),(d) and (e). The beamwidth is calculated with a resolution of 0.1°.

2.7.2 Subarray Beamwidth Comparison

Figure 2.15 shows that the segregated subarray approach offers the narrowest beamwidth, followed closely by the location alignment method. This is expected due the high directivity of these two methods. When a sidelobe exceeds the mainlobe directivity, the beamwidth is measured for the newly formed mainlobe off the desired direction. This explains the sudden change in phase separation beamwidth in 4:32 subarray. This change is also apparent in the beam-squinting graph in figure 2.16(c). The beamwidth of a uniform linear array is $B_{3db} = \frac{.886}{\sin\theta_0}\frac{\lambda}{Nd}$ [46]. This means that the beamwidth is expected to reduce as the frequency increases. The beamwidth of the narrowband array is 10° at the centre frequency. But it broadens as the frequency increases. However the wideband array produces the narrowest beamwidth at the design frequency and narrows as the frequency increases.

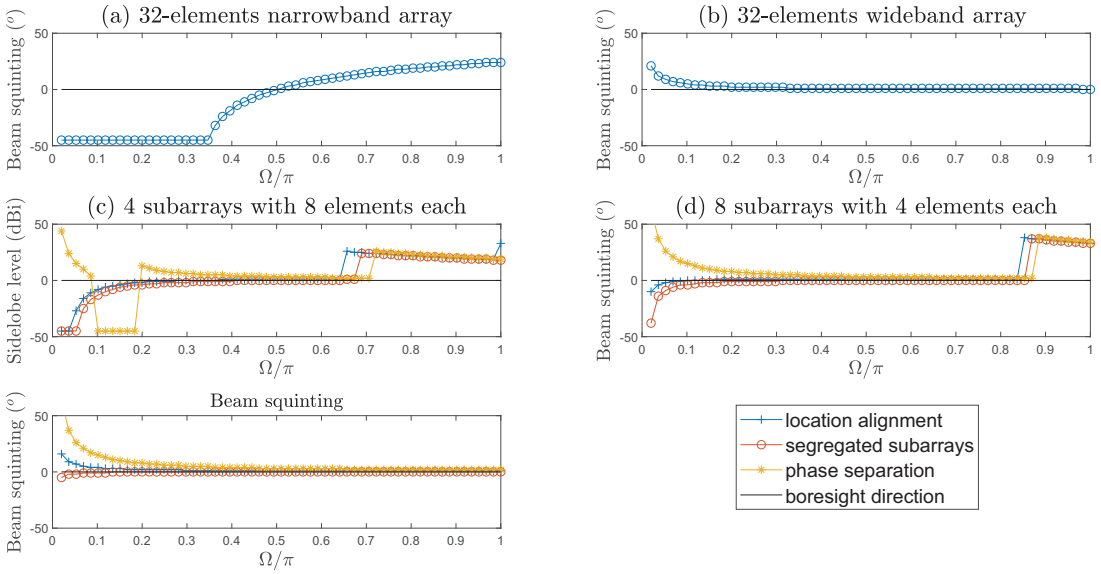

Figure 2.16: Beam squinting of a uniform linear array of 32 elements processed with wideband eigenfilter applied using the three application approaches described in section 2.6, on five different array architectures:(a) Narrowband array, (b) wideband array, and three partial wideband arrays in (c),(d) and (e).

2.7.3 Subarray Beam Squinting Comparison

Close to the upper frequency edge, a sudden drift in beam-pointing angle appears in figures 2.16(c)and 2.16(d) due to the appearance of a sidelobe that is higher than the mainlobe. Figures 2.16(c) and 2.16(d) show that at high frequencies, the sidelobe level exceeds the mainlobe level in the 4:32 and 8:32 subarray ratios, causing the sudden change in peak value from the desired direction to a sidelobe direction. The difference between narrowband and wideband arrays is obvious w.r.t. the beam squinting. The mainlobe of the narrowband array is aligned at the design frequency, but drifts away from the boresight direction as frequency changes. But, the wideband array is aligned to the boresight direction over the entire frequency band except around zero frequency.

In terms of comparison between subarray application approaches, the location alignment technique has the lowest beam squinting in most of the frequency band. The mainlobe in the phase separation technique drifts further away from the desired direction compared to the other methods, especially at low frequency.

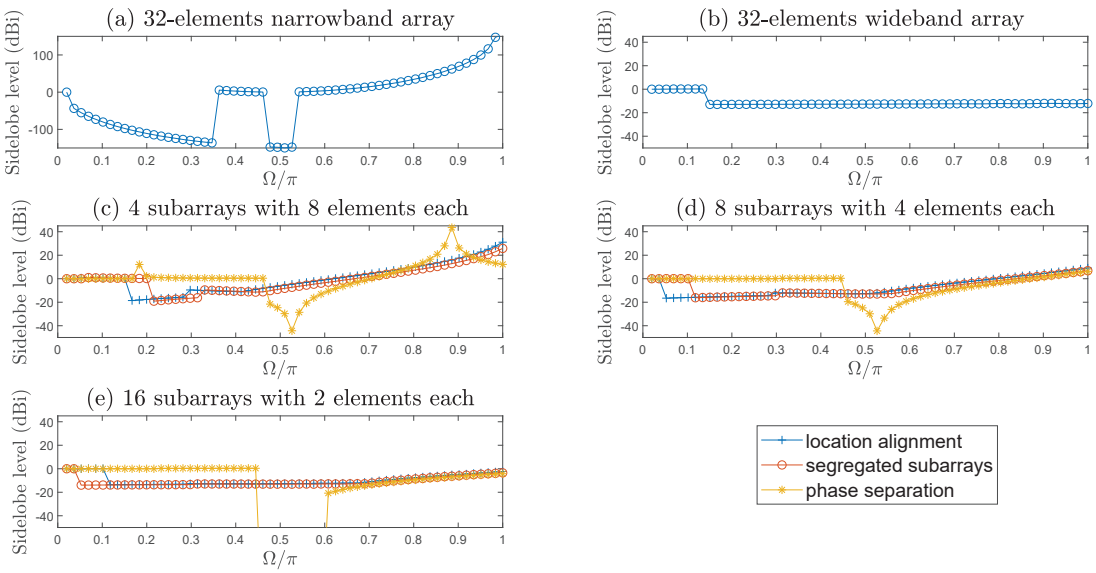

Figure 2.17: Sidelobe level of a uniform linear array of 32 elements processed with wideband eigenfilter applied using the three application approaches described in section 2.6, on five different array architectures:(a) Narrowband array, (b) wideband array, and three partial wideband arrays in (c),(d) and (e).

2.7.4 Subarray Sidelobe Level Comparison

As explained in section 2.3.1, a positive sidelobe level indicates that the response at the desired direction is lower than that of the sidelobe. Figure 2.17 shows that the phase separation method has achieved low sidelobe levels over a small bandwidth around the centre of the band. Exactly at the middle of the band, the sidelobes of all partial wideband arrays are at the same level of about -15dB. This level conforms with the theoretical level of a uniform linear array of side lobe level $(SLL) \approx 1/N$ [34]. Further away from the centre frequency, the sidelobe level increases with the increase in subarray ratio. Appendix A lists the frequency versus angle graphs for the different partial wideband arrays which are used to generate figures 2.13 through to 2.17. The sidelobe level of the narrowband array has a positive sidelobe level over frequencies above the centre frequency. This is due to the squint of the mainlobe. The wideband array has generally achieved a sidelobe level of -15dB which is close to the theoretical sidelobe level mentioned above.

The assessment in section 2.7 is based on a 32-elements linear array. Figure 2.18

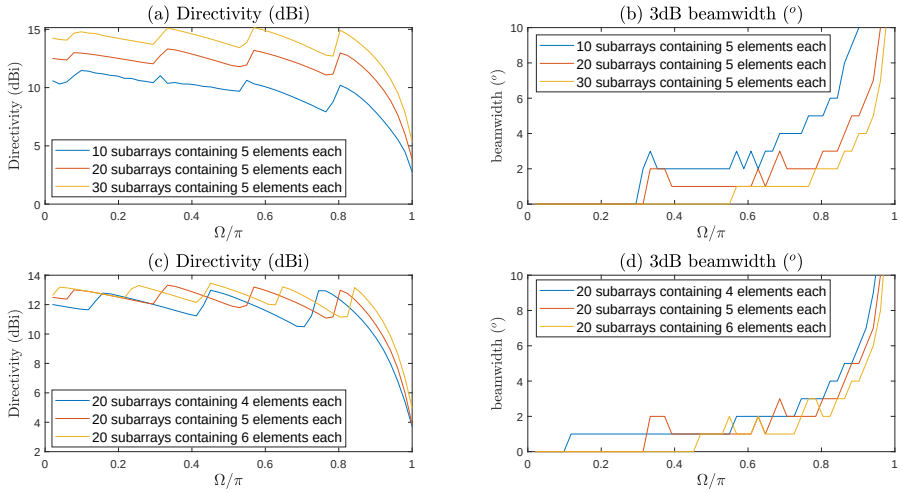

Figure 2.18: Pattern characteristics of partial wideband arrays of different sizes showing (a) directivity and (b) beamwidth of three partial wideband arrays with different number of subarrays, (c) directivity and (d) beamwidth of three partial wideband arrays with different number of elements per subarray.

shows the directivity and beamwidth of different sizes of partial wideband array. Figure 2.18(a) and (b) shows a partial wideband arrays with different numbers of subarrays but with the same subarray size. The increase in the number of subarrays shows to increase the directivity and narrows the beamwidth over the whole bandwidth $\Omega = [0, \pi]$, while it does not shift or scale the frequency response. This vertical improvement is due to the increase in number of elements irrespective of the subarray ratio. The stability of the frequency response is because of the fact that the addition of subarrays comes with an increase in the wideband weights, hence the subarray ratio is unchanged. Hence, the narrowband weights are limited to the same subarray aperture size.

In figure 2.18(c) and (d), the partial wideband array is shown for different subarray sizes but with the same number of subarrays. The directivity does not show any noticeable vertical improvement because the increase in the number of elements is very small compared to the array size. However, the frequency response shows a spreading or shifting caused by the increase in the subarray size while the number of subarray is unchanged. This means that the frequency response of the partial wideband array is mainly affected by the subarray size or subarray ratio.

2.8 Conclusion

This chapter presents the background knowledge required to demonstrate the contribution of this thesis. First, the general concepts of wave propagation and array architectures have been reviewed. Then, wideband data-independent beamforming techniques have been described and investigated. We also studied the application of these beamformers to partial wideband array and identified three possible approaches.

In location alignment, the steering vector used in the beamforming calculations is obtained by aligning the subarrays phase centres along the desired wavefront. This approach replaces the steering vector with a virtual vector that uses the elements locations w.r.t. subarrays' phase centres prior to the beamforming calculations. The segregated subarray approach applies the beamforming individually to each subarray. Then the subarrays outputs are steered using time delays. The phase separation method divides the phase of the beamformer weights between the elements and the subarrays. The subarrays are responsible for the time lag to the subarrays phase centres, and the elements are responsible for the steering phase between the elements and the subarray phase centre. These approaches are irrelevant when using iterative optimisation because the optimisation explores all possible value combinations of narrowband and wideband weights without the need to define the allocation of phase shift between the narrowband and wideband weights.

Applying beamforming on a partial wideband structure is demonstrated and evaluatedon a 32-elements linear array using the eigenfilter beamformer. The segregated subarray approach achieved a higher directivity and narrower beamwidthon uniform linear arrays compared to the other two methods, with a marginal advantage over the location alignment method. Both the segregated subarray method and the location alignment method have similar beam squinting results. The phase separation method has a poor performance in all beam pattern criterion except for its very low sidelobe level over a small bandwidth at the centre frequency.

This chapter aims to define many of the metrics related to wideband subbarrays, and investigate the methods of applying weights on elements and subarrays level. In

the remainder of this thesis, these metrics and methodology will be utilised to improve wideband subarray beamforming. Chapter 3 will apply time delays to subarrays using digital filters, and examine the choice of the centre frequency as a design point in wideband beamforming. Chapter 4 proposes applying a window function to the phase of the weights at the element level to maintain a flat frequency response. Then a noise cancellation filter is proposed which utilises an isolation effect of the phase window. Chapter 5 solves the manifestation of grating lobes inpartial wideband arrays by reducing rotational symmetry of subarrays shapes and elements distribution.

Chapter 3

Accurate Broadband Subarrays Beamforming

This chapter demonstrates the use of the fractional delay filter for spatial steering in the digital domain. Fractional delay filter (FDF) is applied to subarrays in partial wideband arrays to compensate for the propagation delay to the subarrays' phase centre. Three different FDF structures are introduced and compared in terms of bandwidth and flatness of delay value over frequency. An optimisation approach to a narrowband subarray structure is proposed to maintain the off-boresight look direction constraint as flat as possible across a given frequency bandwidth.

3.1 Introduction

Antenna arrays have been widely studied and utilised in narrowband signal transmission and detection. However, many applications require the arrays to operate over a wider bandwidth to enhance performance. In radar for example, the use of wideband waveforms increases range resolution and reduces peak power. In communication, wideband transmission can yield a higher information rate.

The propagation delay with which the wavefront impinges on the array must be compensated explicitly. For a wideband signal, compensation of the propagation delay requires a time delay instead of just the phase shift that sufficed in the narrowband

case. If the signals are transformed to the digital domain, then an approximation of the time delay can be achieved by sample delay [11]. But the samples are discretely timed, while the exact delay is not necessarily a multiple of the sampling period T_{s}. At half the sampling frequency, one sample delay can only provide a spatial steering step from 0^o to 90^o. While the digital structure favours integer delays, the precise delay of a wavefront that needs to be aligned across the sensor array is generally a fractional value of the sampling period. Fractional delays can be achieved by interpolating between signal samples, which is the approximation of a value within a set of known data points. Fractional delay filters are finite impulse response (FIR) implementations of the approximation theory.

Broadband beamforming requires each array element to be followed by a true time delay or a tapped delay line (TDL) to implement frequency-selective filters [47] like the FDF mentioned above. But for most radar applications this is not practical due to the small sensor spacing and limited weight, space and power. Instead, elements can be grouped into smaller subarrays within the array aperture. A compromise for broadband processing in state-of-the-art broadband radar hardware is to operate complex multipliers following the sensor elements. The subarray outputs are then fed into hardware time delay units (TDU), or equivalent digital implementation to reach an acceptable performance across the operating bandwidth [31]. FDF has been implement on subarrays in partial wideband arrays in [48, 49]. However, these sources focus on the implementation of FDF filters, where [48] deals with the digital implementation and [49] uses Farrow FDF structure and focuses on linear frequency modulation waveform.

This chapter explores the digital implementation of time delay using fractional delay filters, and instead of optimising sidelobe levels, the deviation in the beamformer's gain in look-direction is minimized. We demonstrate that the combination of fractional delay filters and optimisation of narrowband weight can provide an acceptable mainlobe performance.

The chapter is organized as follows: The fractional delay filter implementation using tap delay line structure is studied in Section 3.2. The FDF-based subarray architecture is defined in section 3.3. Section 3.4 reviews the standard construction

of the narrowband beamformers by means of designing optimisation at the centre, or median frequency point for wideband response. The FDF-based beamformer design is optimised for flat look-direction response in Section 3.5 and demonstrated in Section 3.6. Finally, conclusions are drawn in Section 3.7.

3.2 Fractional Delay Filters

The FDF filter aims to implement a general delay $\tau \in \mathbb{R}$, where $\mathbb{R}$ is the set of real numbers. In the array context of this thesis, we want it to compensate for the propagation delay T_m experienced by the collection of signals arriving at the m^{th} subarray referenced to the subarray's phase centre. The utilisation of a sample delay can reduce the FDF filter size by an amount of D_m. In this case, the sample delay D_m is the normalized delay rounded to the nearest integer, and fractional delay τ_m is the normalized remainder of this rounding, i.e.

$$\begin{aligned} D_m &= \lfloor \frac{T_m}{T_\mathrm{s}} \rceil \\ \tau_m &= T_m/T_s - D_m \ , \end{aligned} \tag{3.1}$$

where $\lfloor \rceil$ denotes the rounding function.

The ideal interpolation is a consequence of the sampling theory which states that a band-limited signal can be uniquely reconstructed from its discrete samples. The reconstruction requires a passband filtering which transforms to sinc function in time domain, $\mathrm{rect}(e^{j\omega}) \bullet\!\!-\!\!\circ \mathrm{sinc}(n)$, where n is the discrete time index. This implies that in order to approximate a value of a continuous signal from its discrete representation, it should be convolved with an infinite sinc function centred at time τ_m as

$$x(\tau_m) = \sum_{n=-\infty}^{\infty} x[n] * \frac{\sin(\pi[n-\tau_m])}{\pi[n-\tau_m]} \ , \tag{3.2}$$

where $x[n]$ is the discrete representation of $x(t)$. A common measure of a filter phase response is the group delay [50]. The group delay of a filter with phase response $\Phi(\Omega)$ is $G(\Omega) = -\frac{d\Phi(\Omega)}{d\Omega}$. Ideally, the FDF would have to be an infinite sinc function to have

a constant group delay. To obtain finite and causal FDF filter coefficients $v[n]$, the sinc function is shifted and truncated to the filter size J as

$$v[n] = \frac{\sin(\pi[n - \frac{J}{2} - \tau_m])}{\pi[n - \frac{J}{2} - \tau_m]} \ . \tag{3.3}$$

where τ_m is the desired time lag of the m^{th} subarray in a partial wideband array. The estimated signal value at the fractional delay τ_m is

$$x(\tau_m) = \sum_{n=0}^{J} x[n] * v[n] \ , \tag{3.4}$$

Applying a tapering window to the truncated sinc filter can reduces the ripples in frequency domain response [51, 52]. Von Hann window for an odd filter size is

$$\mathrm{w}_{Hann}[n] = 0.5 - 0.5\cos\left(\frac{2\pi n}{J}\right) \ . \tag{3.5}$$

Approximation can also be achieved by representing the given signal samples using polynomials such as the Lagrange interpolation technique [53]. The Lagrange coefficients $v[n]$ of a filter of order J are

$$v[n] = \prod_{k=0, n\neq k}^{J} \frac{\tau_m - k}{n - k} \quad , \qquad n = 0, \cdots, J \ . \tag{3.6}$$

Another common FDF is the Farrow filter structure which isolates the desired delay value from the filter coefficients [54]. However, the filter can only maintains an acceptably flat frequency response at low frequencies [52]. Hence, the use of the Farrow filter is not justified for the data-independent subarray structures discussed in this chapter.

The desired property of a fractional delay filter is its ability to apply frequency-invariant time lag to its input. Filters with constant lag across the frequency band of interest are called Linear phase. Linear phase filters have linear phase as a function of frequency, hence the name. The error metric defined in [52] will be used as a performance measure to compare the three fractional delay filters described above. The error function is the squared absolute difference between the Fourier transform of

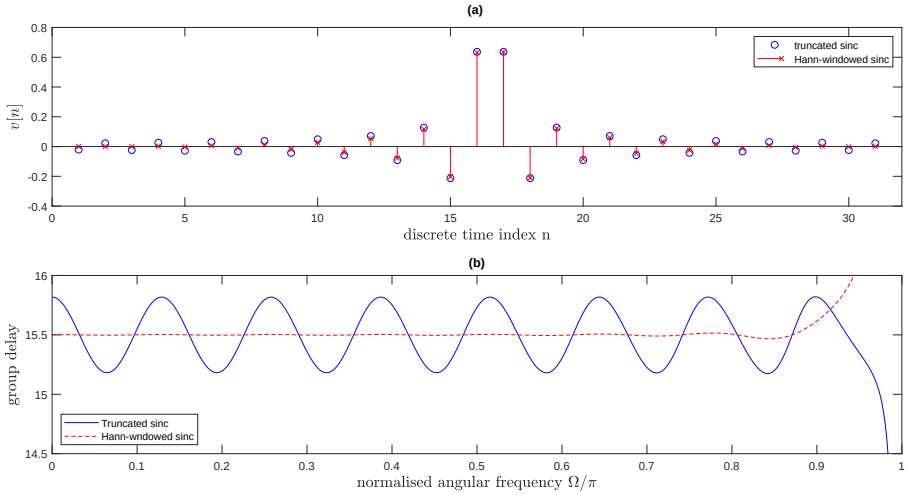

Figure 3.1: (a) Filter coefficients and (b) group delays for fractional delay filters constructed from sinc and windowed sinc functions for $J = 32$ and $\tau_m = 0.5$.

the FDF coefficients $V(\Omega)$ $\bullet\!\!-\!\!\circ$ $v[n]$ and the frequency response $e^{-j\Omega\tau_m}$ of an ideal sinc filter, i.e.

$$e_{gd}(\Omega, \tau_m) = |V(\Omega) - e^{-j\Omega\tau_m}|^2 \,. \tag{3.7}$$

Comparison Between Fractional Delay Filters

As a demonstration of the accuracy, the sinc and Hann-windowed sinc filters for the case $J = 32$ are depicted in figure 3.1(a) for $\tau_m = 0.5$. The fractional delay is approximately centred in the filter. The group delays for the two systems in figure 3.1(b) show the fluctuation of the truncated sinc, while the Hann-tapered window design exhibits a constant phase response at τ_m. The three FDF filters introduced in this chapter, the truncated sinc, the windowed sinc and the Lagrange filter, will be evaluated based on the squared deviation measure introduced in (3.7). For this comparison, each filter has $J + 1 = 51$ tabs, and the sample delay is employed to shift thecentre of the filter coefficients to the centre tap. Figure 3.2 shows the deviation measure of the three FDF structures. The truncated sinc filter in figure 3.2(a) has maintained a progressive increase in error towards the Nyquist frequecy limit which is higher than that of the Hann-windowed sinc. The truncated sinc FDF also suffers from high ripples along the frequency domain for all values of time lag. However, the error value of the truncated

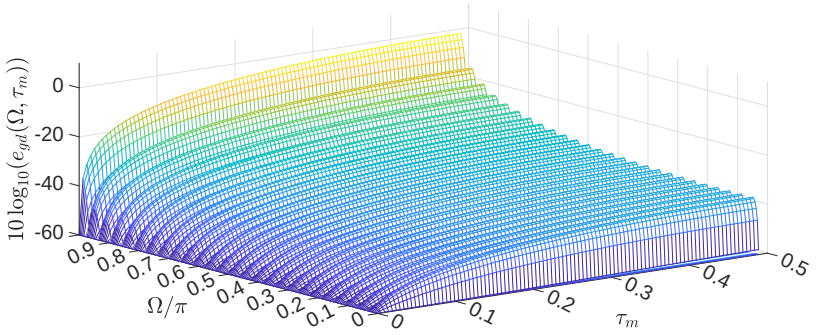

(a) Squared deviation of frequency response in truncated sinc FDF filter.

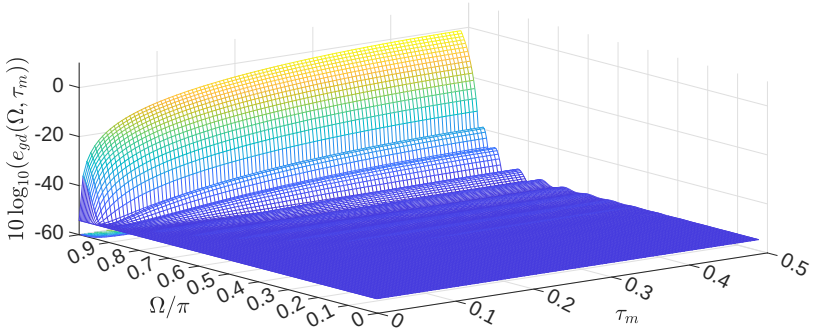

(b) Squared deviation of frequency response in Hann-windowed sinc FDF filter.

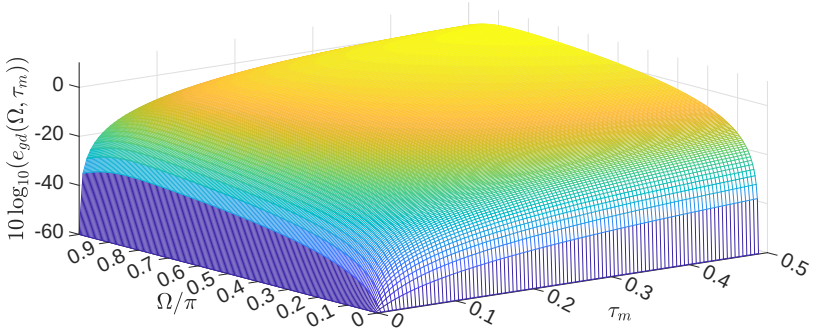

(c) Squared deviation of frequency response in Lagrange FDF filter.

Figure 3.2: The squared deviation of the time lag from the desired delay of a 51-tap filter using (a) truncated sinc, (b) Hann-windowed sinc and (c) Lagrange fractional delay filters.

sinc is maintained below -20dB from $\frac{\Omega}{\pi} = 0$ up to about $\frac{\Omega}{\pi} = 0.95$. The Hann-windowed sinc FDF in figure 3.2(b) has a slightly smaller bandwidth compared to that of the truncated sinc FDF, where the error is maintained below -20dB up to $\Omega/\pi = 0.9$.

However, the ripples in Hann-windowed sinc are only visible on the frequencies above $\frac{\Omega}{\pi} = 0.6$. Most importantly, the Hann-windowed sinc has the lowest error among the three filters across the bandwith $\frac{\Omega}{\pi} = [0\ 0.9]$. Finally, the Lagrange FDF filter has the highest error across the entire bandwidth and, despite the lack of frequency ripples, its error value is higher than -20dB across most of the frequency and time domains. If both bandwidth and group delay flatness are desirable, then the performance of the Hann-windowed sinc filter is balanced between wide bandwidth and low group delay deviation. The Hann-windowed sinc FDF coefficients are

$$v[n] = (0.5 - 0.5\cos(\frac{2\pi n}{J})) \cdot \frac{\sin(\pi[n - \frac{J}{2} - \tau_m])}{\pi[n - \frac{J}{2} - \tau_m]} \ . \tag{3.8}$$

In this rest of chapter, (3.8) will be used to align the subarrays' phase centres.

3.3 Array Configuration

The subarray configuration addressed in this chapter is shown in figure 3.3, where M subarrays each contains K sensors. The Kx2 sensors location matrix is $\mathbf{r}$ where the k^{th} row of $\mathbf{r}$ is the 2-dimensional $x - y$ location of the k^{th} sensor. If a signal arrives from the direction θ and ϕ, then the delay at the k^{th} sensor relative to the subarray phase centre is $\tau_k = \mathbf{r}_k \mathbf{k}_{\theta,\phi}$, where $\mathbf{r}_k$ is the k^{th} row of the location matrix $\mathbf{r}$ and $\mathbf{k}_{\theta,\phi}$ is the wavenumber vector derived from equation (2.2) as

$$\mathbf{k}_{\theta,\phi} = -\frac{\Omega}{cT_\mathrm{s}} \begin{bmatrix} \sin\theta\cos\phi \\ \sin\theta\sin\phi \\ \cos\theta \end{bmatrix} \ . \tag{3.9}$$

Subarray elements are followed by a narrowband complex weights w_k. The M antenna elements are identically configured and are identical across the M subarrays as suggested in the segregated subarray structure in Section 2.6.2, and is organised into the weights vector $\mathbf{w}$ as

$$\mathbf{w}^\mathrm{H} = \begin{bmatrix} \mathrm{w}_1 & \mathrm{w}_2 & \dots & \mathrm{w}_K \end{bmatrix} \ . \tag{3.10}$$

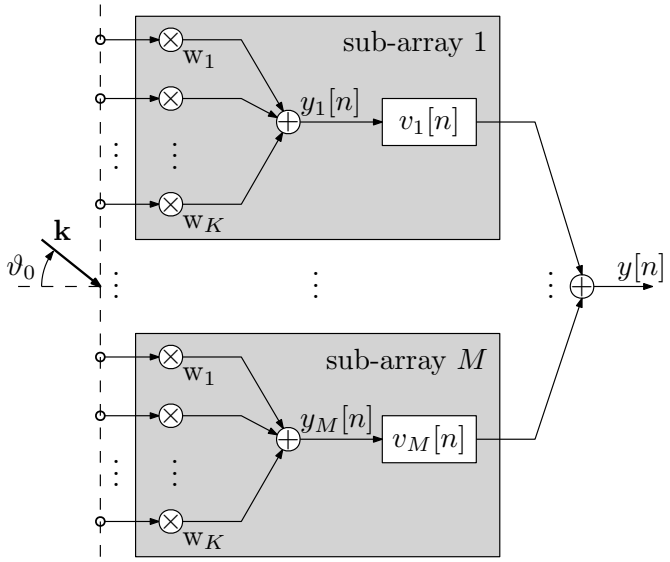

Figure 3.3: Uniform linear array divided into M narrowband subarrays of K sensors each, which are then combined via M filters with coefficients $v_m[n]$, $m = 1 \dots M$. The angle of arrival of an incoming far-field waveform is θ_0.

Each subarray feeds into one of the M TDLs where the m^{th} TDL has the coefficients $v_m[n]$. The purpose of this TDL processor is to coarsely align the subarrays' phase centres towards the desired direction. While the narrowband sensor weights $\mathbf{w}$ will fine-tune the spatial response at a specific frequency.

The proposed approach's aim is to firstly adjust the tap delay filters and secondly to optimise the narrowband coefficient over the operating frequency range to obtain a beamforming response with a constraint in a particular look direction.

3.4 Mainlobe Variation over Frequency

In this section we will analyse the look direction of a narrowband subarray beamformer when operated across a wide bandwidth. For this purpose, we define a steering vector $\mathbf{a}$ that characterises the phase profile of an incoming waveform with the wavenumber

vector $\mathbf{k}$ as

$$\mathbf{a}(\Omega,\theta) = \frac{1}{\sqrt{K}} \begin{bmatrix} e^{j\Omega\tau_1} \\ e^{j\Omega\tau_2} \\ \vdots \\ e^{j\Omega\tau_K} \end{bmatrix} , \tag{3.11}$$

The azimuth angle ϕ is omitted for the linear array. In addition, The dependency on the l.h.s. term the on elevation angle θ will also be omitted because it is fixed atthe desired angle θ_0.

Using the steering vector definition in 3.11, we aim to design a subarray beamformer $\mathbf{w}$ and study how the reference frequency influences the look direction when the overall beamformer is operating over a wider bandwidth. If the gain in the direction θ_0 is expected to be a unit value, then a frequency-dependent error e can be defined as

$$e(\Omega) = \mathbf{a}^{\mathrm{H}}(\Omega,\theta_0)\mathbf{w} - 1 , \tag{3.12}$$

and can be evaluated over a range of frequencies $\Omega \in [\Omega_l;\Omega_u]$, leading to an overall cost function

$$\xi = \frac{1}{2\pi} \int_{\Omega_l}^{\Omega_u} |e(\Omega)|^2 d\Omega . \tag{3.13}$$

Here, Ω_l and Ω_u are the lower and upper frequency bounds respectively. Array weights obtained from delay-and-sum beamformers, have been suggested for broadband partial wideband arrayss [32, 34, 55] using a Wiener-Hopf type solution [11, 56] as

$$\mathbf{w}_0 = (\mathbf{a}^{\mathrm{H}}(\Omega_0,\theta_0)\mathbf{a}(\Omega_0,\theta_0))^{-1}\mathbf{a}(\Omega_0,\theta_0) . \tag{3.14}$$

Assuming a unit value constraint in the look direction, the Wiener-Hopf solution of the normalised steering vector $\mathbf{a}(\Omega_0)$ folds back to a delay-and-sum solution, such that

$$\mathbf{w}_0 = \mathbf{a}^{*}(\Omega_0,\theta_0) . \tag{3.15}$$

Typically the median point of the frequency band $\Omega_0 = (\Omega_u + \Omega_l)/2$ serves as a suitable

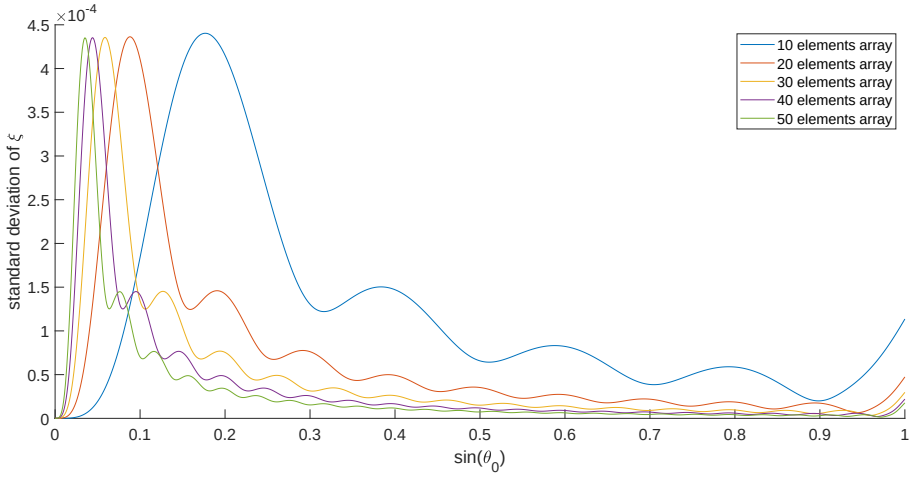

Figure 3.4: The standard deviation of the error function defined in (3.13) calculated over the frequency $\Omega = [0, \pi]$ over all desired angles $\sin\theta_0$ for different sizes of linear narrowband arrays.

reference point to synthesize the beam pattern and frequency response, as suggest e.g. in [47], [32] and [57]. However, the aim here is test the assumption that choosing the median frequency leads to the least frequency-dependent response at the desired direction. The cost function in (3.13) is a measure of the deviation of the mainlobe response from unit value. Figure 3.4 shows the standard deviation of the cost function described in (3.13). The graph is obtained for different array sizes and directions of arrival θ_0. the graph also shows high mainlobe deviation for large arrays close to the boarsight direction. As the the array decrease in size, the peak value of the cost function moves further away from the boarsight direction. The cost function however reduces as the direction approaches $\sin\theta_0 = 1$.

3.5 Proposed Broadband Subarray Design

The analysis in Section 3.4 indicated that computing the subarray weights at the median frequency does not always lead to the lowest response error in the look direction. Therefore, this section will attempt to optimise thenarrowband weights $\mathbf{w}$. Given that $\mathbf{a}(\Omega, \theta_0)$ is the steering vector in the look direction θ_0 at an arbitrary normalised angular frequency Ω. The error defined in (3.12) is the deviation from unit gain in a

beamformer with weights $\mathbf{w} \in \mathbb{C}^K$.

The cost function ξ defined in (3.13) is evaluated over a range of frequencies $\Omega \in [\Omega_l; \Omega_u]$. The optimisation problem for thenarrowband weights $\mathbf{w}$ can be stated as

$$\mathbf{w}_{\text{opt}} = \quad \arg \ \min_{\mathbf{w}} \xi. \tag{3.16}$$

The solution to (3.16) is given by the Wiener-Hopf solution, which can be also derived using the analysis in section 2.5.1, as

$$\mathbf{w}_{\text{opt}} = \mathbf{R}^{-1}\mathbf{p} \ , \tag{3.17}$$

with the covariance matrix $\mathbf{R}$ derived similar to (2.35) as

$$\mathbf{R} = \frac{1}{2\pi} \int_{\Omega_l}^{\Omega_u} \mathbf{a}(\Omega, \theta_0)\mathbf{a}^{\mathrm{H}}(\Omega, \theta_0) d\Omega \ ,$$

and

$$\mathbf{p} = \frac{1}{2\pi} \int_{\Omega_l}^{\Omega_u} \mathbf{a}(\Omega, \theta_0) d\Omega \ .$$

This solution can be approximated by a numerical integration over a specified number of frequency bins. The problem is reformulated as a discrete approximation over a set of $N+1$ frequencies $\Omega_n = \Omega_l + n(\Omega_u - \Omega_l)/N$, $n = 0 \dots N$, i.e.

$$\hat{\mathbf{e}} = \begin{bmatrix} e(\Omega_0, \theta_0) \\ e(\Omega_1, \theta_0) \\ \vdots \\ e(\Omega_N, \theta_0) \end{bmatrix} = \begin{bmatrix} \mathbf{a}^{\mathrm{H}}(\Omega_0, \theta_0) \\ \mathbf{a}^{\mathrm{H}}(\Omega_1, \theta_0) \\ \vdots \\ \mathbf{a}^{\mathrm{H}}(\Omega_N, \theta_0) \end{bmatrix} \cdot \mathbf{w} - \underline{1} = \mathbf{A}^{\mathrm{H}}\mathbf{w} - \underline{1} \ . \tag{3.18}$$

The discretized cost function becomes $\hat{\xi} = \hat{\mathbf{e}}^{\mathrm{H}}\hat{\mathbf{e}}$. Differentiating $\hat{\xi}$ w.r.t. $\mathbf{w}^*$ yields

$$\frac{\partial \hat{\xi}}{\partial \mathbf{w}^*} = \mathbf{A}\mathbf{A}^{\mathrm{H}}\mathbf{w}_{\text{opt}} - \mathbf{A}\underline{1} = \underline{0} \ . \tag{3.19}$$

Therefore, the optimum narrowband weights vector is

$$\mathbf{w}_{\text{opt}} = (\mathbf{A}\mathbf{A}^{\text{H}})^{-1}\mathbf{A}\underline{1} = \mathbf{A}^{\dagger}\underline{1}\,, \tag{3.20}$$

where $\mathbf{A}^{\dagger}$ is the pseudo-inverse of $\mathbf{A}$.

3.6 Simulations and Results

The weights optimization and FDF application approach proposed in this chapter is simulated over all steering angles $\sin\theta_0$. A total of 32 sensors are used to produce five different array architectures. A narrowband array architecture with 32 elements, a partial wideband architecture of 3 subarrays with 12 elements each, 4 subarrays with 8 elements each, 16 subarrays with 2 elements each and a 32 elements wideband array with wideband weights only. The fractional delay is achieved using a Hann-windowed sinc function of order $J = 50$. Figure 3.5 quantifies the flatness of the mainlobe response of the five different array architectures, measured as the standard deviation of the absolute value of the main lobe response $std(|P(\Omega, \theta_0)|)$. Figure 3.5 shows a varying degree of deviation in the mainlobe among array architectures. In the narrowband array, the narrowband weights optimisation does not show an improvement over the the weight calculation based on the centre frequency. In the wideband array, only the wideband FDF weights exist, hence the narrowband weights optimisation does not apply, as apparent in Figure 3.5(e) where both weights calculations coincide. The wideband array produces the lowest deviation from the mainlobe, which is what is expected from frequency-independent weights behind each antenna element. The closest architecture to the wideband array is the 16-subarray architecture in Figure 3.5(d) which maintains a steady deviation over the desired angle range of $[-80°,80°]$. For the partial wideband weights, the optimisation of the narrowband weights have generally achieved lower variations over the mainlobe response. Both narrowband weights calculation methods, i,e, the weights optimisation or the beam-steering w.r.t. centre frequency, are identical around the partial wideband array boarsight. This is due to the lower phase difference between array elements. There are various locations where the

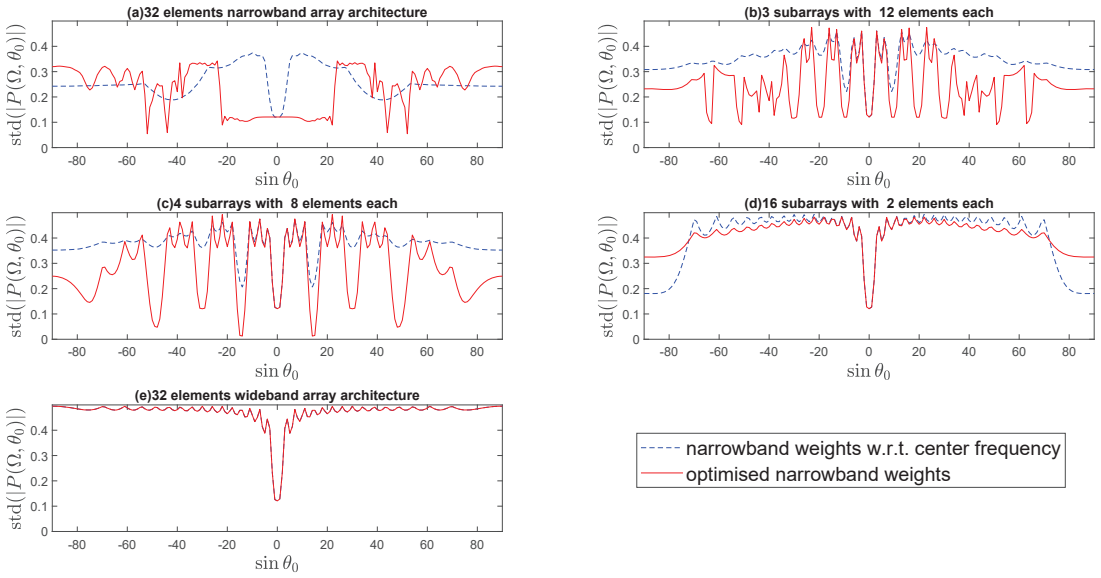

Figure 3.5: Standard deviation of the absolute response in the mainlobe over the entire frequency bandwidth $\Omega = [0, \pi]$, obtained from five different architectures: (a) Narrowband array architecture with narrowband weights only, (b)partial wideband architecture of 3 subarrays with 12 elements each, (c) partial wideband architecture of 4 subarrays with 8 elements each, (d) partial wideband architecture of 16 subarrays with 2 elements each and (e) wideband array architecture with wideband weights only.

weights optisation method generate more variation over the mainlobe. However these locations are limited in width and amplitude value. For most of the desired directions, the weights optimization method have improved the mainlobe flatness over the entire bandwidth when compared to beam-steering w.r.t. the centre frequency.

A partial wideband array containing 4 subarrays with 8 elements each is used here to demonstrate the narrowband weights optimisation. The subarrays are followed by TDL employing Hann-windowed sinc FDF filters of order $J = 50$. The desired bandwidth is one octave between $\Omega_l = \frac{\pi}{2}$ and $\Omega_u = \pi$. Noting that the fractional delay filters are imperfect at frequencies $\Omega \longrightarrow \pi$, the performance at the upper limit of the frequency operating range is not highly accurate. The beam patterns of the two weights calculation methods are shown below for two directions of arrival. Figure 3.6 shows the beamformer normalised beam pattern $P(\Omega, \theta)$ where the TDL filters are designed as FDF filters for an angle of arrival of $\theta_0 = -30°$. As a benchmark, figure 3.6 uses a steering vector for θ_0 and the centre frequency of the interval $[\Omega_l;\ \Omega_u]$. In contrast,

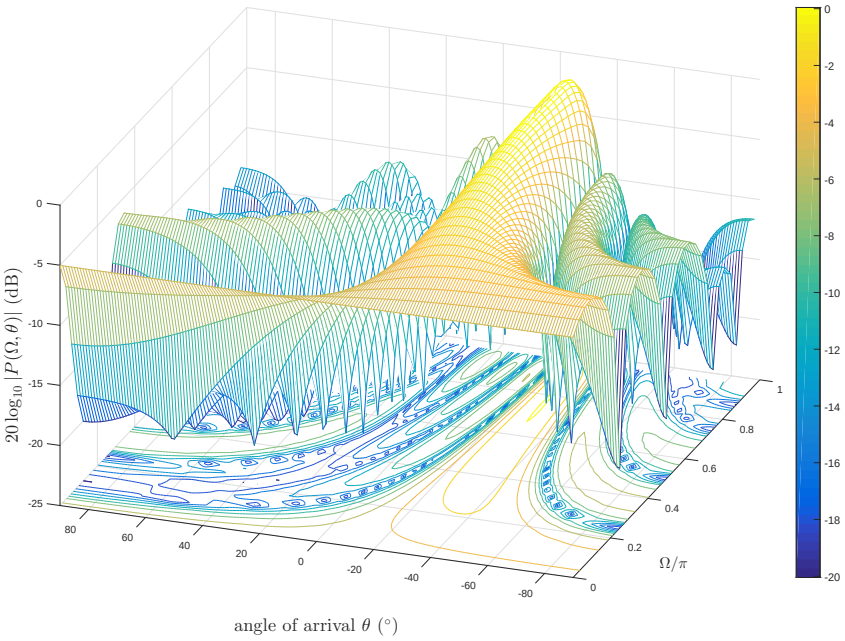

Figure 3.6: Subarray architecture pointing towards $\theta_0 = -30°$ with narrowband beamformers selected w.r.t. centre frequency.

figure 3.7 shows the array response for the case of a narrowband filter design according to (3.20). Sidelobes with a level as high as -0.1 dB appear across the frequency band, but the response in the look direction $\theta_0 = -30°$ has less variations over frequency when compared with the case of figure 3.6.

The same array configuration is used to implement a look direction of $\theta_0 = 60°$. In this case, the beam squinting and variation of the steering vector $\mathbf{a}(\Omega, \theta)$ over the operating frequency range is greater than that of the previous example, and the error is higher. The result for the subarray architecture and a narrowband design at the centre frequency of the interval $[\Omega_l \ ; \ \Omega_u]$ is shown in figure 3.8. The introduced error is such that the desired unit gain in the look direction cannot be maintained.

For the proposed optimised design of the narrowband beamformer, the resulting directivity pattern is shown in figure 3.9. There is a significant improvement over the standard case in figure 3.8, as the unit valued gain in the look direction is maintained across the band. A small deviation towards $\Omega = \pi$ is due to the inaccuracies of the

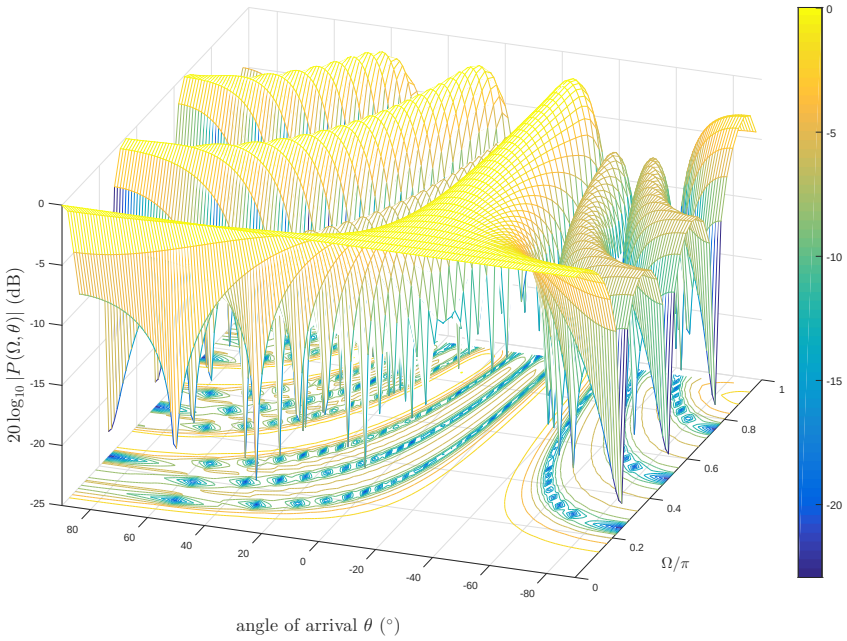

Figure 3.7: Subarray architecture pointing towards $\theta_0 = -30°$ with narrowband beamformers obtained using the optimisation in (3.20).

fractional delay filters as shown in figure 3.2(b).

As a drawback of the proposed design, figures 3.7 and 3.9 exhibit stronger sidelobes compared to the benchmark approach in figures 3.6 and 3.8. A reason for this is that multiple frequency constraints also applies to off-mainlobe directions due to the correlation between spatial and spectral domains. Another reason is the way the optimal design in Section 3.5 tapers the weights and therefore restricts the aperture illumination at the array edges, as shown in figure 3.10, which shows the coefficients for the case of $K = 8$ for a look direction $\theta = 60°$.

The taper efficiency in (2.17) is a measure of the weighting amplitude effect on the directivity. It is equivalent to the aperture efficiency in the absence of all other factors like blockage and current distribution. The taper efficiency of the delay-and-sum weights is 0.3 while the proposed weighting achieves 0.2. This is a slight reduction of spatial resolution in the proposed optimised design compared to the improvement in frequency flatness.

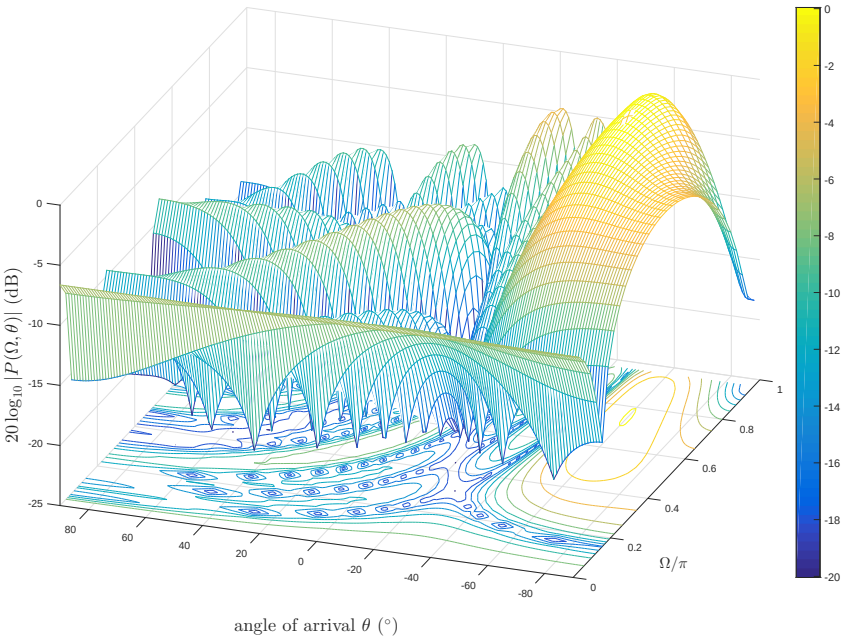

Figure 3.8: Subarray architecture pointing towards $\theta_0 = -60°$ with narrowband beamformers selected w.r.t. centre frequency.

3.7 Conclusions

This chapter studies the use of FDF filters to simulate a frequency-independent time delays at the subarray level which, by similarity with TDU-based subarrays, can improve the bandwidth by a factor of the number of subarrays, and maintain a unit response on the look direction over the entire frequency band, at the cost of a high sidelobes level.

Three FDF types are presented and evaluated in this chapter. The truncated sinc FDF filter is a truncation of the ideal reconstruction filter known in the sampling theory. The truncated sinc has maintained a low deviation up to $\Omega = 0.95\pi$ frequency, but the filter's group delay has high ripples across the band causing distortion to wideband signals. The Hann-windowed sinc filter maintains low deviation from the desired lag and have a flat group delay response across the band, albeit at a slightly lower bandwidth. The Lagrange filter has the highest deviation from the desired group delay compared to the truncated sinc and Hann-windowed sinc.

Additionally, a subarray architecture was proposed where fractional delay filters

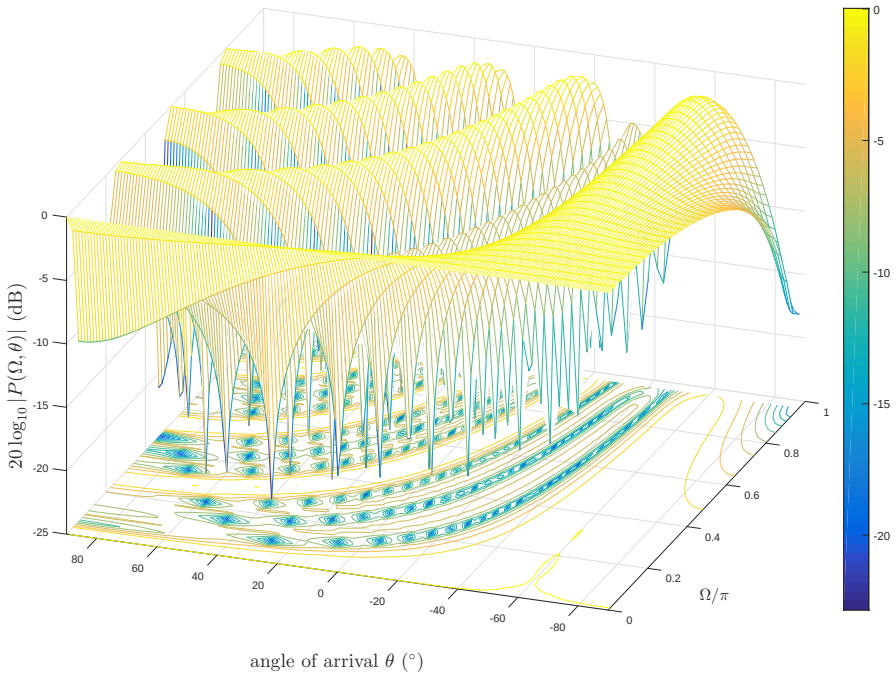

Figure 3.9: Subarray architecture pointing towards $\theta_0 = -60°$ with narrowband beamformers optimised w.r.t. (3.20).

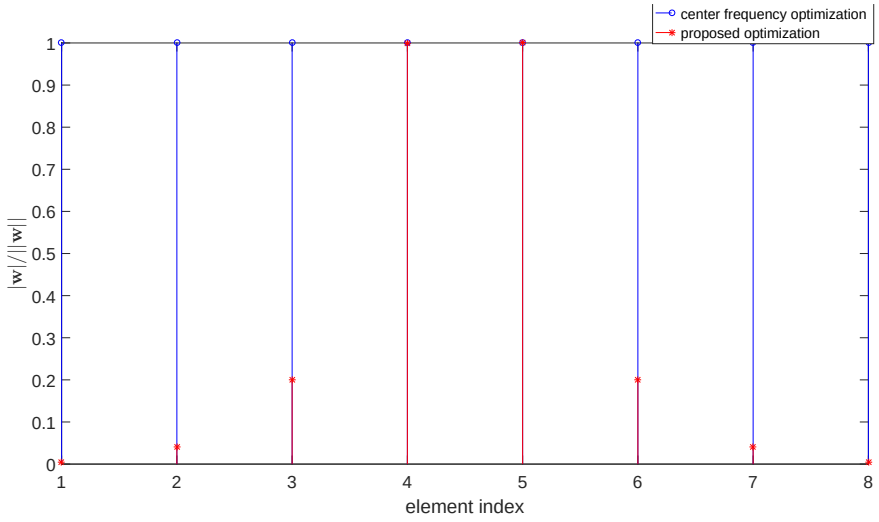

Figure 3.10: Normalized amplitude of the narrowband elements coefficients $\mathbf{w}$ within a subarray designed for the look direction $\theta = 60°$. The blue graph is for the delay-and-sum beamformer designed at the centre frequency, while the red graph represents the proposed optimisation.

coarsely align subarrays in time. The implementation utilise windowed sinc functions of moderate order, which can demonstrate sufficient accuracy close to half the sampling rate. A finer tuning for every subarray is performed by narrowband weights applied to the elements within subarrays. If defined as phase shifts, these narrowband weights can only provide an accurate beamforming at one given frequency, and are likely to generate an error in the look direction gain at other frequencies.

Therefore, an error minimization for the subarray gain deviation in the look direction is required. When operating a partially wideband array in a very wide bandwidth, the centre frequency is commonly adopted to design the array weights, this has shown here to generally yield sub-optimal results. For the delay-and-sum beamformer, this assumption has been challenged in this chapter and shown to cause a higher response error at angles away from boresight direction. Instead, we have proposed a weight optimisation that can accurately impose the desired constraint, albeit at the cost of sidelobes due to a waste of the narrowband beamformer aperture, which is a by-product of the optimisation procedure.

Chapter 4

Mainlobe Alignment in Wideband Subarrays

This chapter explores the elimination of the beam squinting caused by the elements' phase shifting in linear subarrays by windowing the elements' phase. Then, this phase windowing is applied to a partially adaptive subarray structure, which is shown to provide a level of isolation between the subarray outputs. This isolation is then used to implement a subband adaptive noise cancellation (ANC) system to improve the wideband interference suppression.

4.1 Introduction

For planar arrays, the elevation angle has the same effect on the steering vector as the signal frequency. The steering vector described in (2.6) is shown here for a planar array lying in the x–y plane.

$$\mathbf{a}(\omega, \theta, \phi) = e^{-j\frac{\omega}{c}\mathbf{r}[\sin\theta\cos\phi\ ,\ \sin\theta\sin\phi]^{\mathrm{T}}}\ . \tag{4.1}$$

For a fixed steering vector, the angular frequency ω and the elevation direction $\sin\theta$ are inversely proportional, and satisfy the relation $\frac{\omega}{\sin\theta}$ =constant. Therefore, the pairs of frequency and elevation angles cannot be discriminated. An incident signal from an elevation angle θ_1 and a frequency f_1 can produce the same response as another signal

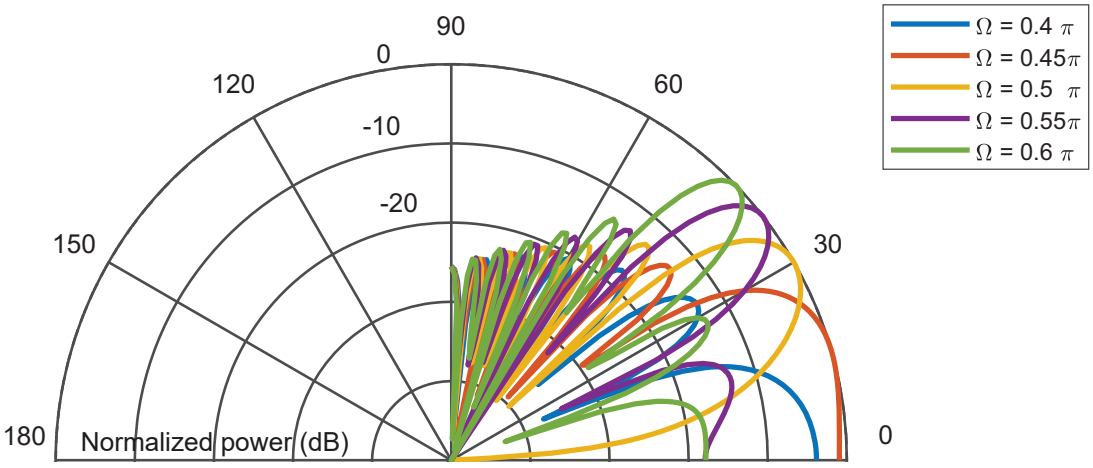

Figure 4.1: The squinting effect of frequency on a narrowband linear array containing 30 elements. The narrowband weights are beam-steered towards $\theta_0 = 30°$ w.r.t. $\Omega_0 = 0.5\pi$.

from an elevation angle θ_2 and a frequency f_2 if they satisfy the condition

$$\frac{f_1}{f_2} = \frac{\sin\theta_2}{\sin\theta_1} \ . \tag{4.2}$$

Given a reference parameter pair (f_0, θ_0), this results in a beam direction θ that changes with frequency f as

$$\theta = \sin^{-1}\left(\frac{f_0}{f}\sin\theta_0\right) \ . \tag{4.3}$$

Figure 4.1 demonstrates the deviation of the mainlobe over frequency. The figure shows the elevation pattern of a narrowband linear array containing 30 elements. The array is beam-steered towards the angle $\theta_0 = 30°$ w.r.t. the center frequency $\Omega_0 = 0.5\pi$. The mainlobe is sampled at five frequencies within the frequency range $\frac{\Omega}{\pi} = [0.4, 0.6]$. The figure shows squinting and widening, or shrinking, of the mainlobe as a function of the operating frequency.

In the remainder of this chapter, the phase shift windowing approach is introduced in Section 4.2. Section 4.3 develops the phased-windowed array weighting and derives the array response for a generic Hamming window function. Section 4.4 studies the correlation between the spectral components of the desired wideband signal when applying phase windowing to a subarray. Section 4.5 describes a structure that combines

phase-windowed subarrays with a subband adaptive noise cancellation to improve the signal to interference plus noise ratio(SINR). Then, the phase windowed subarray and the subband ANC are demonstrated in examples and discussed in Section 4.6. Finally, conclusions are drawn in Section 4.7.

4.2 Phase Shift Windowing

Phase shifting in phased arrays compensates for the propagation delay between the wavefront of the desired direction and the array elements. However, phase shifting is not a linear phase, meaning its time lag depends on frequency. Several solutions exist for the frequency dependency of the phase shifting in wideband arrays. True-time delay (TTD) [58, 59] simulates a propagation delay rather than a phase shift. TTD is commonly constructed using switched optical delay lines or a subband phase shift structure. However,hardware for true-time delay is larger and heavier than a phase shifter [32], hence it is commonly not feasible for an individual array element. Fractional delay filters (FDF) [5,60] are the digital realization of a time delay based on interpolation filtering. FDFs interpolate the sampled input and approximate its value at delays that are not necessarily an integer multiple of the sampling period. Section 3.2 has covered some of the theory and methods of FDF filters. However, FDF requires Analog to Digital Conversion (ADC), which complicates the system if applied to array elements.

The contiguous subarray solution [59,61] provides a trade-off by using phase shifting at the element level and a TTD at the subarray level. Wideband beamforming of the contiguous subarray commonly combines a simple beam-steering at the element level [60] and digital adaptive beamforming at the subarray level [62]. In beam-steering, the array weights are the conjugate of the steering vector towards the desired direction θ_0 at frequency ω_0 as demonstrated in equation (3.15). In a uniform linear array, the wideband beam pattern with beam-steering is

$$P(\omega,\theta) = \frac{h(\omega,\theta)}{\sqrt{N}} \frac{\sin \frac{1}{2} N \frac{d}{c}(\omega \sin\theta - \omega_0 \sin\theta_0)}{\sin \frac{1}{2} \frac{d}{c}(\omega \sin\theta - \omega_0 \sin\theta_0)} , \tag{4.4}$$

where $h(\omega, \theta)$ is the amplitude tapering. The use of phase shifts leads to the displacement of the array pattern as the frequency changes. From (4.4), both ω and $u = \sin\theta$ have the same effect on the array amplitude response.

Wideband beamforming techniques do not address beam squinting directly. At best, they consider the directivity variation as a cost function to be minimized. The inverse DFT method defines two auxiliary frequency terms to control the frequency over a fixed elevation angle [24,63] or uses auxiliary terms that represent both the frequency and the elevation [47]. The inverse DFT method assumes a given fixed elevation angle, requires uniform elements spacing, and applies an approximation that leads to a deviation from the desired response.

The Least Squares and Eigenfilter approach [37,39,41] minimizes the deviation from the desired pattern. The deviation is averaged over the bandwidth and can include a weighting function to emphasise some frequency bands over others. Eventually, a single frequency is represented in the steering vector at which the pattern is synthesised. If no frequency weighting is employed, the median of the bandwidth becomes the design frequency.

Iterative optimisation techniques like minimax optimisation [64], convex optimisation [36,57] and SRV constrained pattern [18] searches the set of complex weights from the solution space that minimizes the objective function. Optimisation techniques implicitly address phase shift deviation over frequency. However, optimisation techniques are computationally complex and require the constraints and the objective functions to be convex. In the next section, we present a simple phase windowing approach that reduces pattern squinting over frequency.

4.3 Phase-Windowed Array Response

When steering an array towards a direction $u_0 = \sin\theta_0$, the phase shift is calculated based on a single frequency, which is commonly the centre of the operating band. However, the steering vector at frequencies across the band will vary in phase, causing the response at the edges of the band to drift off-direction or even outside the beamwidth.

This drift is even higher for wider bandwidths or narrower beamwidths. We suggest applying a window function to the elements' phase shifters in a subarray structure, then apply subband adaptive noise cancellation at the subarrays' outputs. The window will allow the subarrays to steer towards the desired direction at different frequencies.

4.3.1 Phase-Windowed Weights and Window Limits

The phase window function $g(k)$ is applied to the elements' weights of the uniform linear array as

$$\mathrm{w}(k) = \frac{h(k)}{\sqrt{K}}\, e^{j\omega_0 g(k) r(k) \frac{1}{c} \sin\theta_0} \ , \tag{4.5}$$

where $r(k) = (k - \frac{K-1}{2})d$ is the location of the k^{th} element and $h(k)$ is the amplitude tapering function. The array factor of a linear array, beam-steered at frequency ω_0 toward a direction θ_0 and phase window $g(k)$ is

$$P(\omega, \theta) = \sum_{k=0}^{K-1} \frac{h(k)}{\sqrt{K}} e^{-j\ (k-\frac{K-1}{2})\ \frac{d}{c}\ (\omega \sin\theta - g(k)\omega_0 \sin\theta_0)} \ . \tag{4.6}$$

The window function can be any type of the common window functions$f(k)$, but it should be truncated around the frequency limits . The window edges should extend beyond the points where the weights gradient is perpendicular to the steering vector phase at the desired direction and at edge frequencies $\Phi(\mathbf{a}(\omega_L^H, \theta_0))$. The lower window limit can be described by the equality

$$[g(k)]_{\omega_L} \leq \{g(k) \mid (\Phi(\mathbf{w}(k+1)) - \Phi(\mathbf{w}(k))).\Phi(\mathbf{a}(\omega_L, \theta_0)) = -1\} \ . \tag{4.7}$$

The same limit applies to the upper frequency limit ω_H since the window function is an even function around $\frac{K}{2}$. For a small bandwidth or near the boresight direction, the windowing has minor effect because the beam squinting is negligibly small.

Table 4.1: Window types generalized by (4.8). The variable F_1 in truncated Taylor window is called the pedestal.

window type	A	B
Cosine Window	0	1
Hamming window	0.54	0.46
von Hann window	0.5	0.5
Truncated Taylor	$\frac{1+F_1}{2}$	$\frac{1-F_1}{2}$

4.3.2 Generic Hamming Window Array Response

The generic Hamming function $g_h(k)$ is representative of the cosine, modified Taylor, von Hann, and Hamming windows [65], and can be described as

$$g_h(k) = A + B\cos\left[\pi(\frac{k}{K-1})/K\right] . \tag{4.8}$$

Table 4.1 shows the window types that can be obtained by specifying the values A and B in the generic window definition in (4.8). The response of a linear array after applying the generalized Hamming phase window is

$$P(\omega,\theta) = \sum_{k=0}^{K-1} \frac{h(k)}{\sqrt{K}} e^{-j(2k+K+1)\frac{d}{c}\left(\omega\sin\theta + A\omega_0\sin\theta_0 + B\omega_0\sin\theta_0\sin[\pi\frac{2k+1}{2K}]\right)} . \tag{4.9}$$

The derivation of (4.9) can be found in Appendix B. Equation (4.9) shows the response of a linear array where the phase windowing approach is combined with beam-steering.

4.4 Spectral Isolation in Phase Windowing

In this section, it will be shown that applying phase windowing to a partial wideband array can partially isolate the frequency components of a wideband signal between the subarray outputs. This spectral decomposition is then used to improve the signal SNR using an ANC filters at the subarrays' processors.

For simplicity, a signed rectangular window is applied to a partial wideband array containing two subarray ($M = 2$). The signed rectangular window is not applicable to more than two subarrays because its integral, which is a triangular function, only

have two slopes. The window is applied to all array elements including the subarrays, where K is the number of elements in the array. Each subarray is subjected to a segment of the window. Consequently, this partial wideband array employing a signed rectangular window across all its narrowband weights, has two subarrays each being steered a quarter of the bandwidth to either side of the centre frequency.

The lower and higher frequency limits in (4.7) are $\omega_L = \hat{\omega}_L + \frac{1}{4}BW$ and $\omega_H = \hat{\omega}_H - \frac{1}{4}BW$, where $\hat{\omega}_L$ and $\hat{\omega}_H$ are the lowest and the highest operating frequencies, respectively. The window function is now defined as

$$g(k) = 1 + \text{sgn}(k - \frac{(K-1)}{2})\frac{\omega_H - \omega_L}{4\omega_0} \ , \quad k \in [0, \cdots, K-1] \ . \tag{4.10}$$

where sgn() is the sign function and K is the number of elements in the array including all subarrays. Note that since sgn(0) = 0, the element at $k = \frac{K-1}{2}$ has a unit valued window function. Hence it will support both subarrays because it will be steered at the frequency ω_0 which is the median of the frequency limits ω_L and ω_H. The elements of the weight vector in (4.5) become

$$\text{w}(k) = \frac{h(k)}{\sqrt{K}} e^{j(\omega_0 + \text{sign}(k - \frac{(K-1)}{2})\frac{\omega_H - \omega_L}{4})r_k \frac{1}{c}\sin\theta_0} \tag{4.11}$$

The response of the upper band subarray $k \in [\frac{K}{2}, (K-1)]$ to a lower band signal at frequency $\omega_0 - \frac{\omega_H - \omega_L}{4}$ arriving from θ_0 is

$$\begin{aligned} P(\omega, \theta) &= \mathbf{w}_t^{\text{H}} \ \mathbf{a}\big(\omega_0 - \frac{\omega_H - \omega_L}{4}, \theta_0\big) \\ &= \sum_{k=\frac{K}{2}}^{K-1} \frac{h(k)}{\sqrt{K}} e^{-jr_k \frac{1}{c}\sin\theta_0 \left[(\omega_0 - \frac{\omega_H - \omega_L}{4}) - (\omega_0 + \frac{\omega_H - \omega_L}{4})\right]} \\ &= \sum_{k=\frac{K}{2}}^{K-1} \frac{h(k)}{\sqrt{K}} e^{jr_k \frac{1}{c}\sin\theta_0 \frac{\omega_H - \omega_L}{2}} \quad . \end{aligned} \tag{4.12}$$

Figure 4.2 shows the isolation between the subarrays in a partial wideband array containing two subarrays with 15 elements each. The isolation is calculated using (4.12) for all angles and all bandwidths $(\Omega_H - \Omega_L)$, where P_1 in the figure is the normalised

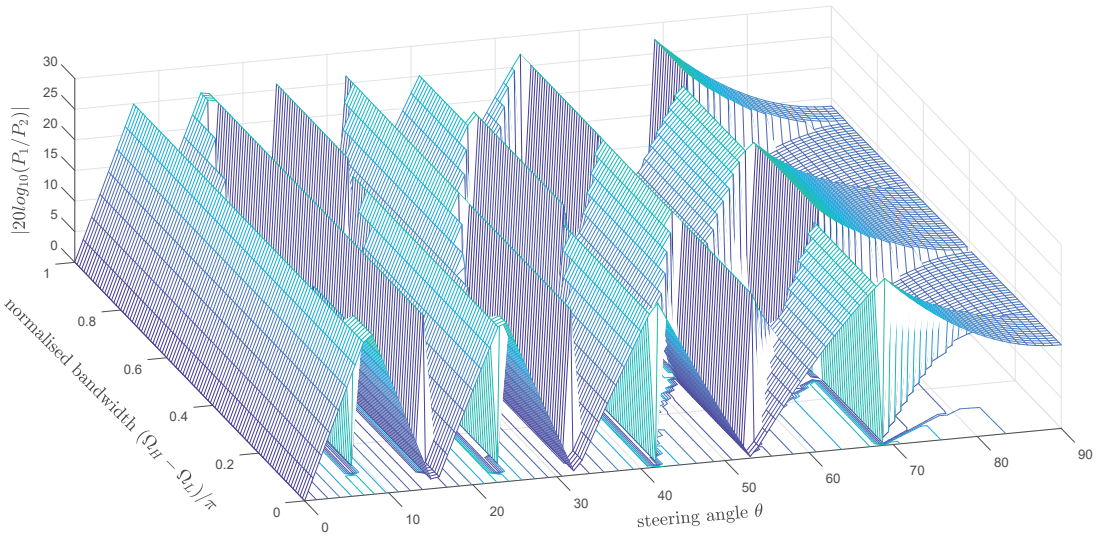

Figure 4.2: Isolation between subarrays in a partial wideband array, using the signed rectangular window in (4.10).

response of the low band subarray and P_2 is the normalised response of the high band subarray. Graphs of both P_1 and P_2 are shown in Appendix C in real and imaginary values. The signed rectangular window described in (4.10) is used with a uniform tapering function, $h(k) = 1$. The figure shows that for the signed rectangular window, the isolation between the subarrays ranges from 0dB, meaning that the subarrays's responses are identical, to 27dB in power ratio. In general, this graph shows that there are ranges of bandwidths and directions where the subarry outputs can maintain a level of isolation between them. The subarrays' isolation can be further improved with more subarrays or by applying window functions with more curvature so that the steering frequencies of of the edge subarrays exceeds the bandwidth edges.

4.5 Interference Suppression in Phase-Windowed Subarrays

This section combines the phase windowing with adaptive noise cancellation on the partial wideband architecture. This adaptive noise cancellation is a local deviation from the data-independent theme of the thesis. The phase windowing will enable sampling the target wideband signal at various frequencies. Then, using the beam squinting

phenomenon, subband adaptive noise cancellers are used to suppress the wideband interference.

4.5.1 Phase Windowing on a Subarray Structure

The proposed array structure is a linear partial wideband array similar to the structure suggested in [31–34] and described in Section 2.4.2. The partial wideband array is partially adaptive, meaning only the subarray outputs are accessible by digital processing. The array contains M subarrays, each containing K elements. The subarrays are steered using FIR-based fractional delay filters. Figure 4.3 illustrates the phase windowing on a linear partial wideband array. The proposed phase windowing differs from the conventional beamspace beamforming described in section 2.4.3 in that the phase windowing can be applied to the partial wideband architecture, while the beamspace processor requires a set of narrowband weights for each synthesised beam. For example, the generalised sidelobe canceler (GSC) and the postbeamformer interference canceler (PIC) [11] apply a main and an auxiliary beamforming to the array elements directly. However, the elements in the architecture described in Figure 2.8 are only accessible by one set of weights.

An FDF filters shift the subarray's phase centre (dotted line in Figure 4.3) to the wavefront of the desired direction (dashed line in Figure 4.3). The elements' phase shifts apply the phase-windowed weights (solid line in Figure 4.3). The partial wideband array is beam-steered using the wideband weights towards the desired direction θ_0. However, at each subarray, the phase shifts are tuned at different frequencies depending on the window gradient. This arrangement can lead to a spatial isolation between subarray outputs, particularly at the edges of the array aperture. With the elements'narrowband weights are modified to include the phase window as in (4.5) and the subarray steering vector is defined by $\mathbf{a}_m(\Omega, \theta)$, the mth subarray response is

$$P_m(\Omega, \theta) = \mathbf{w}_m^{\mathrm{H}} \mathbf{a}_m(\Omega, \theta) e^{j\Omega\tau_m} \ , \tag{4.13}$$

where τ_m is the time delay w.r.t. the mth subarray's phase centre. The phase windowing

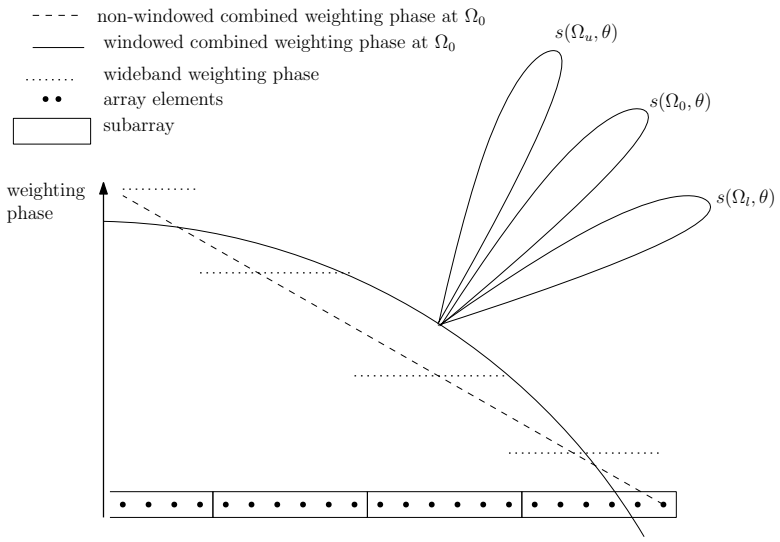

Figure 4.3: Demonstration of the phase shift window method and its effect on beam pattern at the centre and edges of the frequency band. The window is shown in solid line. The wavefront is shown as dashed line and the subarray FDF delay is shown as dotted line.

is imposed by the weights term $\mathbf{w}_m$. Notice the use of the normalised angular frequency Ω to suit the discrete signal representation.

4.5.2 Subband Adaptive Noise Cancellation

The phase window, if suitably designed, can maintain a level of isolation between the subarray outputs, as demonstrated in Section 4.4. Subband decomposition of the subarray outputs can isolate the signal's frequency components while containing a correlated estimate of the noise and unwanted wideband interference. The mth subarray output, assuming only one source of interference, is

$$y_m[n] = P_m(\Omega, \theta_0)s[n] + P_m(\Omega, \theta_i)s_i[n] + v[n] \,, \tag{4.14}$$

where $s[n]$ is the signal of interest, θ_i and $s_i[n]$ are the angle of arrival and the waveform of the interference signal, respectively, and $v[n]$ is a spatially uncorrelated noise.

Figure 4.4 shows the proposed combined partial wideband and subband ANC structure. The subarray outputs are digitally delayed using a fractional delay filter (FDF) to align the subarrays' phase centres. The FDF outputs are divided into M frequency

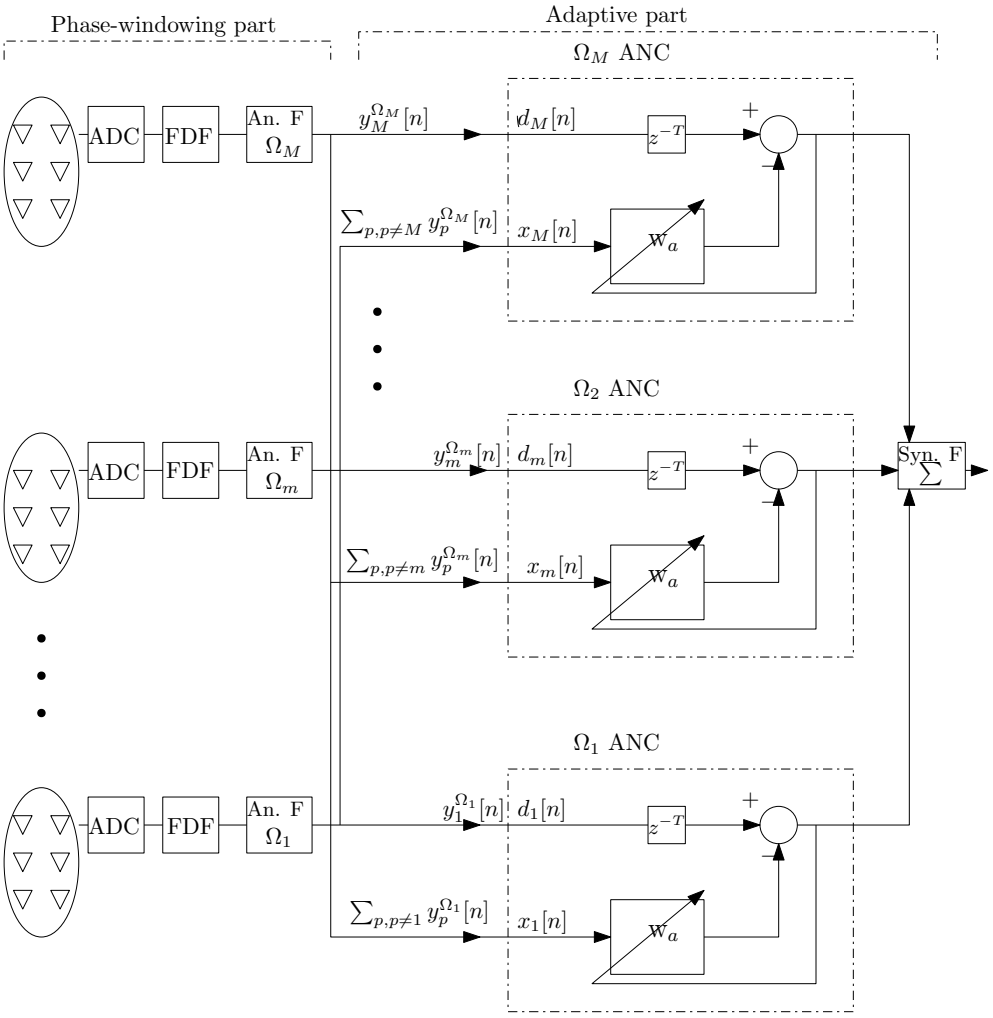

Figure 4.4: The proposed subband ANC structure attached to the subarrays' outputs of a partial wideband array.

components using an analysis filter bank [66]. The m^{th} ANC filter receives the m^{th} subband of the m^{th} subarray's output as its signal input $d_m[n]$, and delays it to an equivalent of the adaptive filter order T. The ANC filter also receives the sum of the m^{th} frequency components of the remaining subarrays' outputs as its noise input $x_m[n]$. Many types of adaptive filters can realize the ANC structure, such as the Affine Projection Algorithm (APA), Recursive Least Squares (RLS), or Normalised Least Mean Squares (NLMS).

The signal bandwidth is divided into M subbands using analysis filters banks. The subarrays are attached to analysis filter banks that decompose the entire bandwidth

into M bands each connected to its associated ANC filter. Note that both subarrays and bands share the same indexing letter m. This is because each subarray is allocated a band in the phase windowing approach. The m^{th} ANC filter accepts the mth frequency component of the mth subarray output $d_m[n] \circ\!\!-\!\!\bullet\, Y_m(e^{j\Omega_m})$ as the signal input. It also takes $x_m[n] \circ\!\!-\!\!\bullet\, \sum_{p,p\neq m} Y_p(e^{j\Omega_m})$, which is the the sum of the remaining subarray outputs, as the noise input or reference signal. Finally, the subband ANC filter outputs are combined using a synthesis filter bank to produce the output of the adaptive part of the combined partial wideband array and ANC structure.

4.6 Results and Discussion

In this section, the phase windowing is applied to a partial wideband array employing the delay-and-sum beamformer and compared to the same array but without the application of the phase windowing. Then the subband noise cancellation is demonstrated using a broadband multi-carrier signal active over 5 subbands. The design alignment of the mainlobe across the the operating frequency band is evaluated using the sum of the squared deviations from the steering angles θ_0 across the operating bandwidth $\Delta\Omega$ as

$$\xi_{ss} = \sum_{\Omega_l}^{\Omega_u} |\theta|_{P_{max}(\Omega,\theta)} - \theta_0|^2 \tag{4.15}$$

where $\theta|_{P_{max}(\Omega,\theta)}$ is the measured mainlobe direction.

The proposed phase window is applied to a linear partial wideband array with 5 subarrays of 12 elements each. The narrowband elements' weights are obtained using (4.5) for all steering angles θ_0 and center frequencies Ω_0 over a bandwidth of $\Delta\Omega = 0.2\pi$. Figure 4.5 shows the sum of squares of the mainlobe deviation ξ_{ss} defined in (4.15). The amplitude taper applied is a Hamming function, and the phase window is a Gaussian function with a constant $\sigma = 0.8$. In Figure 4.5(a) the array is beam-steered using a delay-and-sum beamformer as a benchmark, while in Figure 4.5(b) the array is using the proposed phase windowing in addition to beam-steering. Figure 4.5 demonstrates the role of phase windowing in improving the mainlobe alignment on this array example. The mainlobe deviation is generally lower near the boresight direction.

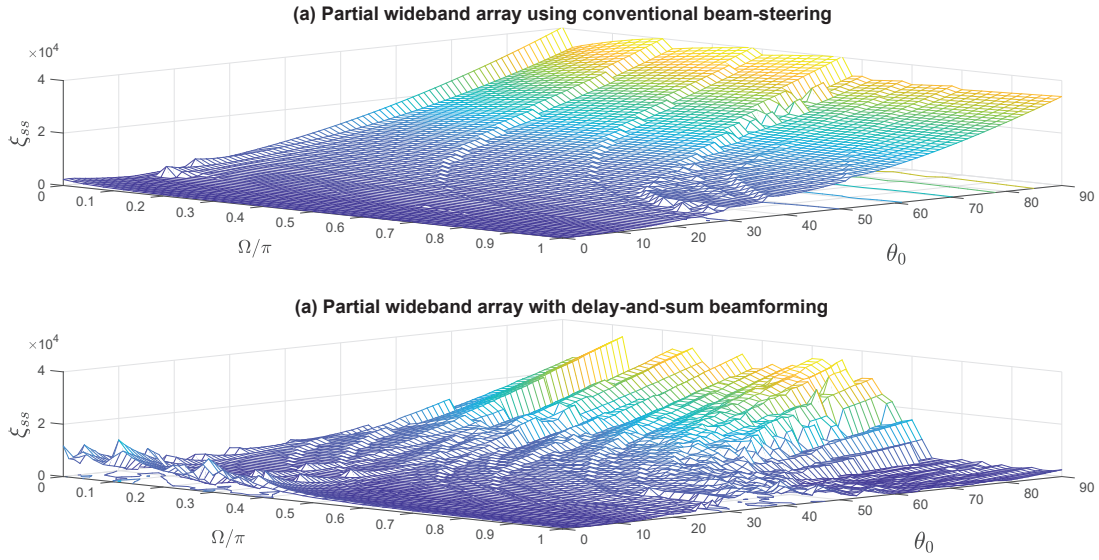

Figure 4.5: Sum of squares of the mainlobe deviation ξ_{ss} for a partial wideband array containing 5 subarrays with 12 elements each (a) using a delay-and-sum beamformer. (b) using the proposed phase windowing on the conventional beam-steering.

At higher steering angles, the conventional beam-steering progressively increases the mainlobe deviation in both arrays. However the proposed phase windowing maintains the low deviation from $\Omega = 0.75\pi$ up to the upper frequency limit. For the rest of the band, the phase windowing approach generally maintains lower deviation compared to the conventional beam-steered array.

As an example, Figures 4.6 and 4.7 show a partial wideband array array response at a specific steering angle of 30° or $u = 0.5$. The array is slightly larger with 6 subarrays of 30 elements each. Figure 4.6 shows the response of the combined outputs of the phase-windowed partial wideband array. Figure 4.7 shows the same array steered using conventional beam-steering.

The array's mainlobe in Figure 4.6 is aligned with an acceptable beamwidth over the frequency band $[0.25\pi; 0.75\pi]$, except at the transitions between the subbands, which can be improved by increasing the number of subarrays. By contrast, the conventional beam steered partial wideband array in Figure 4.7 shows a drifting mainlobe across the frequency band. The sidelobes are not significantly different between the two cases.

The subband ANC filter structure is also tested on an array containing 5subarrays with 20 elements each. The subarray outputs are aligned to the desired wavefront using

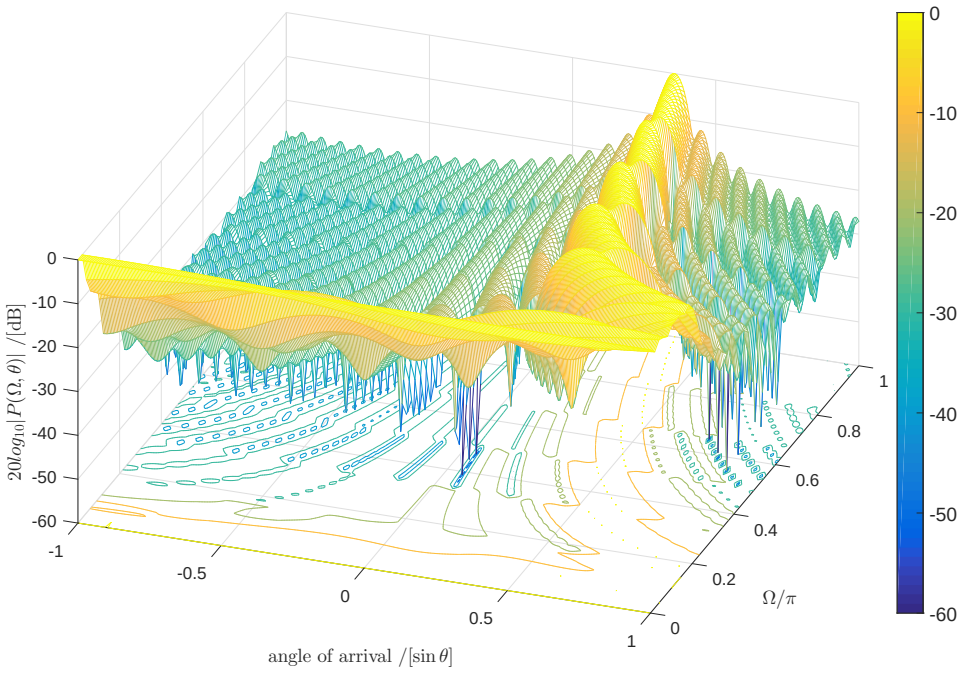

Figure 4.6: Phase-windowed subarrays' response with 6 subarrays of 30 elements each and a desired angle of 30°.

81-tap windowed sinc FDF filters [51]. The desired multi-carrier signal comprises of 5 subbands or frequency components covering a normalised bandwidth of $[0.5\pi;\pi]$ with an angle of arrival 30°. The input is a multi-carrier signal with a signal to noise ratio of 28 dB. The input interference has the exact waveform as of the desired signal, but shifted in frequency by an amount of $+0.1\pi$ to allow for comparison, and arrives from $\theta = 60°$ AOA. A band-limited noise is added to the the received signal, in the form of a spatially distributed clutter. The noise power is -30dB w.r.t the signal power. The ANC is implemented using 51-tap RLS filters.

Figure 4.8 shows the power spectral density (PSD) of the signal and the interference at various points in the proposed structure. Figure 4.8(a) shows the desired signal with an angle of arrival of 30°, and Figure 4.8(b) illustrates the interference with angle of arrival of 60°. Figure 4.8(c) depicts the combined subarray output prior to the subband ANC filters. Finally, Figure 4.8(d) shows the resulting waveform after combining the outputs of the ANC filters. Figure 4.9 quantifies the signal to interference plus noise

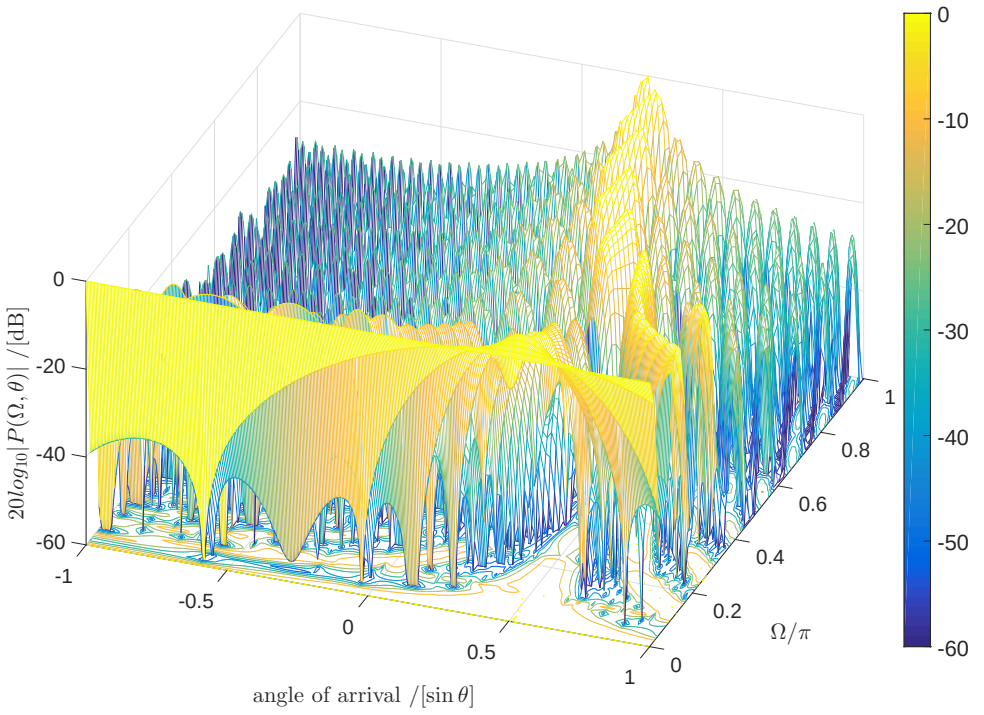

Figure 4.7: Response of a partial wideband array containing 6 subarrays of 30 elements each beam-steered towards direction of $\theta = 30°$ or $\sin\theta = 0.5$.

ratio (SINR) at the outputs of the phase-windowed part and the adaptive parts shown in figure 4.4. The component at 0.85π has experienced a small increase in SINR of about about 0.1dB. This can be due to the alignment of frequency and angle where the change in frequency and angle of arrival has the same effect on the response according to (4.2). Apart from the 0.85π component, the SINR at the output of the adaptive part has improved across the spectrum. Although the interference is not completely rejected, the figure shows an interference reduction, with the exception of the 0.85π component, ranging from 2.5dB for the 0.7π component to 15dB for the 0.7π component. The strong response at the 0.8π component can be due to the relative flatness of the window function at the centre subarray, leading to a better phase alignment of the frequency components at the center of the subband.

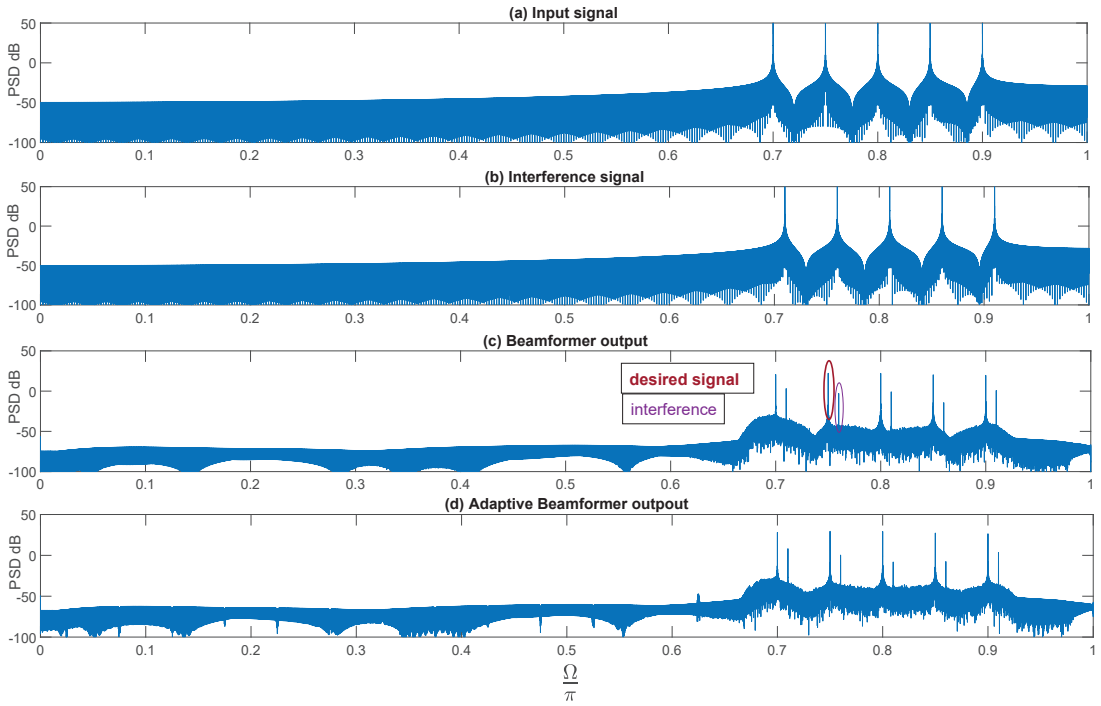

Figure 4.8: Power spectral density of the broadband signal arriving from angle 30° as it propagates through the proposed system. (a) The desired signal arriving from $\theta = 30°$, (b) the interference signal arriving from $\theta = 60°$, (c) the combined subarray output and (d) the subband ANC output.

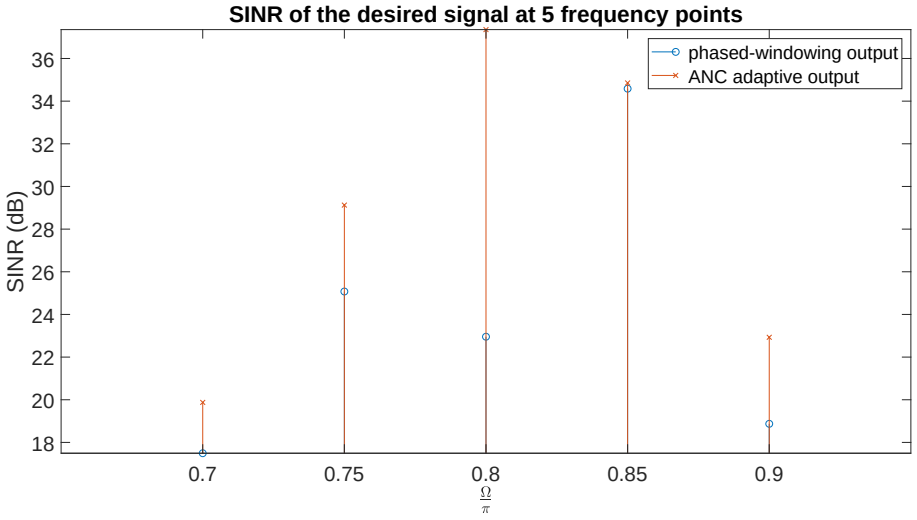

Figure 4.9: SINR values at the outputs of the phase-windowing and the adaptive parts in figure 4.4 for the 5-subcarrier signal and interference example.

4.7 Conclusion

The previous chapter proposed an optimisation approach to maintain a flat frequency response over the mainlobe without considering its effect on the sidelobes. This chapter attempted to remedy the underlying cause of mainlobe variation with frequency, and then use a by-product of that treatment to improve the interference suppression in partial wideband array using subband ANC filters.

First, the chapter studied beam squinting in wideband arrays, analyzed the relationship between frequency and elevation angle in linear arrays, and described beam squinting as a function of frequency. A phase windowing was then proposed on the elements' phase shifts in a partially adaptive subarray to remove the drifting of the mainlobe over frequency. The phase-windowed response of a linear array was derived for a generic Hamming window, which is representative of many other window types. The window function is truncated around the points where the tangent of the phase is perpendicular to the angle of arrival at the edge frequencies. The phase window was tested on a partial wideband array containing 6 subarrays with 30 elements each. The resulting weights was able to align the mainlobe over a normalised bandwidth of $[0.25\pi; 0.75\pi]$, albeit beam drifting appears at subband transitions.

A subband adaptive noise cancellation was proposed to remove the wideband interference from the subarrays' outputs using subband ANC filters to improve the signal to interference plus noise ratio. The subarrays are divided into frequency subbands using analysis filter banks. At the m^{th} subarray, the m^{th} subband is used as the signal input $d_m[n]$ in the m^{th} ANC filter since it contains a frequency component of the desired signal. In contrast, the remaining subbands are fed to the remaining ANC filters as noise inputs $x_p[n],\ p \neq m$.

A phase-windowed partial wideband array containing 5 subarrays with 20 elements each was then used to demonstrate the subband adaptive noise cancellation structure. The subband ANC filter structure consists of 5 RLS filters with 51 taps. The simulation showed improved SINR in most of the frequency components, although the SINR in one frequency component was unaffected. The subband ANC can be further improved

by increasing the size of the FDF filters and considering subarray spatial decorrelation techniques like null placement in the frequency domain or applying an additional blocking matrix to the edge subarrays.

Chapter 5

Rotationally Tiled Subarray

This chapter proposes a structural array design that reduces grating lobes and modularizes the subarray structure.

5.1 Introduction

To avoid spatial aliasing in uniform sensor arrays, element spacing should be shorter than half the wavelength of the maximum observed frequency. If the element spacing exceeds this limit, grating lobes appear in the visible region of the array response. For wideband arrays, increasing the upper frequency limit will require smaller element spacing leading to increased risk of mutual coupling. More importantly, spacing reduction leads to a higher number of sensor elements needed to satisfy a fixed aperture size.

Many solutions have been suggested towards grating lobe reduction and elimination. In thinned arrays [2, 17], random array elements can be removed without significantly affecting the beam pattern performance. This arrangement can maintain the original beamwidth but the gain degrades and the sidelobe level increases because of the reduced total number of elements per unit area combined with inefficient aperture illumination.

Grating lobe suppression has also been applied to subarrays. At the subarray level, the grating lobes are reduced but not eliminated since each subarray output still suffers from grating lobes that, when not considering the sine of the angle from the array boresight, are equal to the level of the main beam. However, the subarray

position or shape ensures that grating lobes do not necessarily coincide. One popular subarray approach is to construct subarrays with random shapes [67, 68] resulting in randomly spaced phase centres. Another solution is to slightly twist the subarray by different angles [69, 70] or randomly displace their location in one dimension [71] or two dimensions [69]. These techniques are likely to complicate the array design and manufacturing because random subarray outline and element distribution require unique assembly, components and programming for each subarray. The distribution network and subarray processing will also need tailoring to suit each subarray.

Array architecture design in practice is a balance between the performance objectives on one side, and physical, technological and economical constraints on the other side. Performance objectives such as gain, sidelobe level, beamwidth and bandwidth are dictated by the aperture size and shape, elements distribution and the instantaneous bandwidth of the system. On the hand, physical, technological and economical constraints affect the array maximum aperture size, manufacturing processes and technologies employed such as time delay versus phase shift.

The solutions for grating lobe reduction listed earlier require additional design, assembly and verification processes to manage randomness in the elements or the subarrays location and structure. These architectures also increase data management complexity, increase production variance, hence contributing to quality loss [72]. These outcomes are discouraged by quality control theories like statistical process control (SPC) and six sigma [73]. Modularization is called "the goal of good design" [74].

Therefore, this chapter proposes two novel designs of planar arrays from identical subarrays that can fit by translation (displacement) and rotation. These new array outline designs suppress grating lobes and provides expandable array size. The modular partial wideband array can also include time delay units, down conversion and analog to digital conversion (ADC). We will show that this arrangement minimizes the subarray external interconnections allowing simple and reliable system integration and testing.

This chapter is organized as follows: Section 5.2 analyses the formation of grating lobes in standard uniform arrays and rotationally tiled arrays. Section 5.3 introduces plane tiling, isometry operations, tiling design notations and limitations to be consid-

ered when applying tiling to arrays and subarrays. Section 5.4 further elaborates on the relationship between tiling and subarray design and offers performance measures, symmetry detection and an approach to explore tile-design combinations. Sections 5.5 and 5.6 demonstrate grating lobes reduction and other attributes using two examples of subarrays constructed using tiles and designs found in the literature on geometry. Finally, discussions and conclusions are drawn in Section 5.7.

5.2 Analysis of Grating Lobes

5.2.1 Grating Lobes in Rotationally Tiled Arrays

Partial wideband array with suppressed grating lobes can be constructed with isohedral subarrays. Isohedral tiling is a plane tiling based on a single shape of tile, where the overall array can be constructed by placing rotated and displaced subarrays. While displacement does not affect the subarray response w.r.t. its phase centre, rotation changes the azimuth angle of arrival by an amount equal to the rotation angle ψ. Consider a rotationally tiled array that has M subarrays and an order of rotation L, — to be further elaborated in Section. 5.3 — the M subarrays will rotate at L different angles. If the array is steered towards $\mathbf{k}_0(\omega_0, \theta_0, \phi_0)$, the response of the rotationally tiled array w.r.t. a signal characterised by the wavenumber $\mathbf{k}(\omega, \theta, \phi)$ is

$$P(\omega, \theta, \phi) = \frac{1}{\sqrt{N_x N_y}} \sum_{l=0}^{L-1} \sum_{\substack{m \\ m \in M_l}} \frac{\sin(\frac{1}{2}\mathbf{r}_{\max} \operatorname{diag}\{\cos\psi_l, \sin\psi_l\}\, \Delta\mathbf{k}))}{\sin(\frac{1}{2}\mathbf{r}_{\min} \operatorname{diag}\{\cos\psi_l, \sin\psi_l\}\, \Delta\mathbf{k})} , \tag{5.1}$$

where M_l is the set of subarrays that share the same rotation angle ψ_l. As an illustration, the design shown in figure 5.4(c), have 30 subarrays ($M = 30$), six rotation angles ($L = 6$) and size (M_l) $= 5$ subarrays sharing the same rotation angle ψ_l. The peaks of the response in (5.1) are located at the zeros of the denominator. For a partial wideband array with subarrays that have the same orientation, the subarrays rotation angles are $\psi_l = 0^\circ \; \forall \; l = 1, .., L$. In this case the response folds back to (2.21) and the grating lobes occur at $\Delta\mathbf{k} = [p_x; p_y]\frac{2\pi}{d} \;\; \forall \; p_x, p_y \in \mathbb{Z}$. However, for a rotationally tiled array with subarrays rotated at angles ψ_l, each subarray group $m \in M_l$ has grating lobes forming at

a periodicity of $\Delta\mathbf{k}_l = 2[(p_x\pi(d\cos\psi_l)^{-1}\ ;\ p_y\pi(d\sin\psi_l)^{-1})]^{\mathrm{T}}\ \ \forall\ p_x, p_y =\in \mathbb{Z}$. The sum of periodic functions is also periodic with a period equal to the least common multiple $LCM()$ [75]. The overall array grating lobes are the result of the alignment of the grating lobes of all the subarrays, which is where the grating lobes of all subarrays coincide in the $\mathbf{k}$ space. As the order of rotation L increases, the separation between overall array grating lobes will increase by a factor of $[LCM((\cos\psi_l)^{-1})\ ;\ LCM((\sin\psi_l)^{-1})]\ \forall l$ in the $\mathbf{k}$ 2-dimensional space. Minor grating lobes are the contribution of subarrays groups $m \in M_l$ sharing the same rotation angle. If the tile and design have no symmetry alignment then the upper limit of minor grating lobes is $\frac{M_l}{K} = \frac{1}{L}$. This is because only M_l out of K subarrays share the same element spacing in any given direction.

There are cases where the subarray tile is rotationally symmetric at one of the design rotation angles such as the hexagonal tile that will later be discussed in figure 5.4(b). If this is the case, and the elements lattice is also symmetric at these angles then subarrays are said to be congruent and will have an aligned grating lobes. A rectangular lattice has a second-order symmetry, and the isosceles triangular lattice have only one, while equilateral triangular lattice has a third-order rotational symmetry. A brief introduction to rotational symmetry can be found in [76].

5.3 Plane Tiling for Subarrays

5.3.1 Tiling

In geometry, tiling or tessellation is the problem of finding a countable family of shapes that can tile a plane without overlaps or gaps [77]. The closed set of tiles that can fill the plane in such a fashion is described as

$$\mathfrak{T} = \{T_1 \cdots, T_m, \cdots T_M\}\ . \tag{5.2}$$

Specifically, isohedral tiling allows only congruent tiles $T_1 \cdots, T_m, \cdots T_M$ to populate the array aperture. Congruent tiles are of the same shape but have been displaced or rotated differently. The subarray outline is defined by the tile shape.

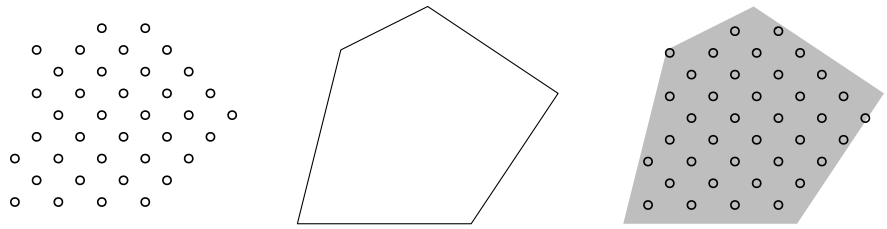

Figure 5.1: Defining subarray tile as (a) a separate motif and (b) polygon outline, or (c) as a combined complex structure.

There are two possible definitions of the subarray tile. The first definition is where the subarray outline and the elements are defined separately. Subarray elements can be defined as points on the Euclidean space forming a motif as shown in figure 5.1(a). Then, the subarray outline is defined as a polygon as shown in figure 5.1(b). Both the elements and the subarray outline are superimposed on each other to form the subarray. The second definition is that the subarray tile is a complex shape that includes a polygon outline and a point grid representing element locations in figure 5.1(c). Unlike the closed tile which is only defined by its closed curve outline e.g. a polygon, a motif can have any arbitrary shape [78].

The difference between these tile definitions is that, instead of using the combined motif definition in figure 5.1(c), the array elements and the subarray outline are separated in 5.1(a) and 5.1(b), respectively, to simplify the geometric structure. The separate definitions of the element lattice and the subarray outline make it geometrically easier to transform and measure the motif which represents the element lattice, and the motif outline which represents the subarray outline. The combined motif definition is more difficult to transform and measure. For example, for a polygon with v vertices, the rotational symmetry detection and order calculation requires v steps, while complex combined motif requires $v \log v$ steps [79].

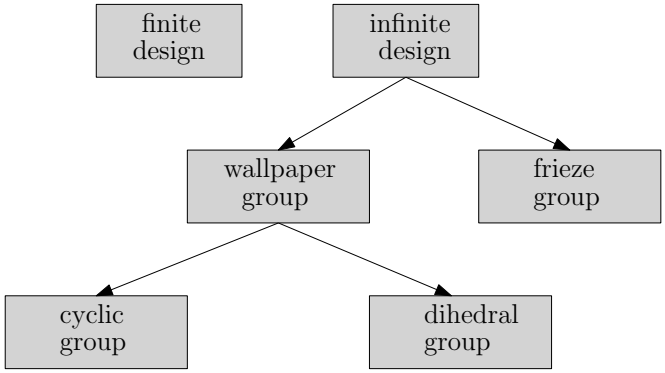

Figure 5.2: cyclic groups classifications.

5.3.2 Design

Design is the arrangement of tiles, or the way tiles fit together to cover a Euclidean plane. For an isohedral tiling, the design is the set of transformations applied to the generating tile to fit to the plane $\mathfrak{T}$. The designis represented by the transformation set $\{\sigma_1, \cdots, \sigma_M : \mathfrak{T} = \sum_1^M \sigma_m T_0\}$. The tile T_0 is the generating or base tile and it is not necessarily part of the design. In other words, the m^{th} tile can be obtained by transforming the base tile using the m^{th} transformation, i,e, $T_m = \sigma_m T_0$. Designs can be finite or infinite. Infinite designs are periodic [80], meaning that they can fill an infinite plane by periodic repetition. If the repetition extends over one dimension, then the pattern is called a frieze group. If it extends over the entire plane, then it is called a wallpaper group. There are two distinct groups of wallpaper class, the cyclic group, which is denoted as *cn* and dihedral group, which is denoted as *dn* where *n* denotes the number of rotation angles. For example cyclic group with a second-order symmetry is denoted *c2*. Cyclic symmetry group applies rotation and transition transformations only. The dihedral group, also, includes reflection and glide reflection transformations. Finite patterns are dihedral groups, meaning they always include reflection or glide reflection. This research is only concerned with infinite cyclic groups because reflective transformations are not applicable to subarrays due to their aperture being fixed to one face. Figure 5.2 shows the hierarchy of cyclic groups. Finite designs can attain the characteristics of other groups, hence left outside the hierarchy in figure 5.2.

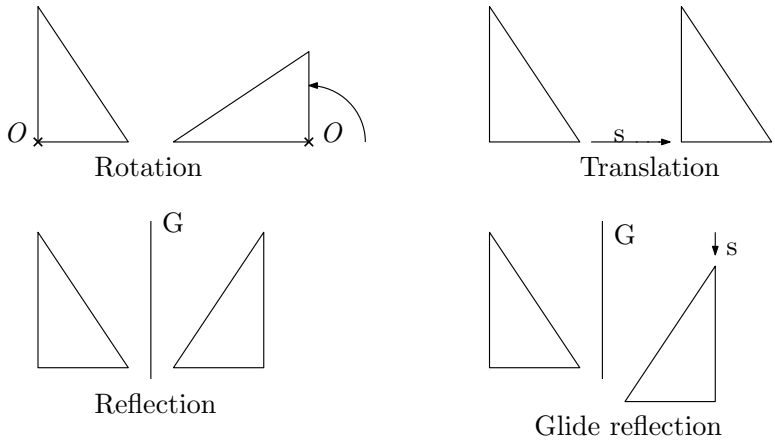

Figure 5.3: The four isometries, rotation, translation, reflection and glide reflection.

5.3.3 Tile Isometry

Isometry, also called rigid motion, is any transformation in Euclidean space $\sigma : R^2 \rightarrow R^2$ that maps the tile T onto itself while preserving all distances [77]. Direct isometry additionally preserves the orientation [80]. For any two polygons for example, if all distances between vertices remain the same, then both tiles are said to be congruent. The symmetry transformation $T' = \sigma T$ has four types, called symmetry groups or isometry operations:

1. **Rotation**: A tile rotate around a centre of rotation O with angle θ. The number of angles that tiles rotate within a design is called the order of rotation n and the design is said to have n-fold order of rotation.

2. **Translation** is the displacement by a distance s in the Euclidean space.

3. **Reflection** is the 180^o rotation around any axis line of reflection G that lies on the tile Euclidean plane.

4. **Glide reflection** is the combination of reflection along the line G and translation along a path parallel to G.

Figure 5.3 shows the four isometry operations on an asymmetric triangle. The first two operations in figure 5.3 are direct isometries because they preserve the sequence of vertices. The third and forth operations are called indirect or reflective.

Table 5.1: Four-symbol notation of the International tables for Crystallography that describes tiling design.

Symbol	Value	Description
1	p,c	p = **primitive** used primitively without reflection on itself c = **centred** tiles reflected along its edges prior to translation
2	1 ... 6	The order of rotation n
3	m , g , 1	m = reflection axis normal to x-axis g = glide reflection axis normal to x-axis 1 = no reflective symmetries normal to x-axis
4	m , g , 1	m,g,1 = similar to the third symbol above but at an angle α from x-axis, where α is a design rotation angle indicated in symbol 2 above.

5.3.4 Notation

One of the most commonly used tessellation notations is the international tables for crystallography [81]. This international notation has four symbols to describe the unit cell and the design symmetries that are described in Table 5.1. It is common to omit the last two symbols in Table 5.1 for non-reflective designs when the last two digits in the notation are 1. If the tile order of rotational symmetry equals the design order of rotation then the order of rotation n falls back to 1. For example if the hexagonal tile in figure 5.4(b) is used in a $p611$ design, the tiles will rotate back to the original shape. Making the design equivalent to $p111$. Notice that primitive designs p are non-reflective. Figure 5.4 shows three examples of non-reflective designs.

5.3.5 Subarray Limitations

The choice of subarray outlinesis limited to convex polygons. A convex polygon has reflex interior angles that are less than 180 degrees. Only rotation and translation can be applied to subarray tiling when generating congruent tiles. Therefore, reflective operation, reflection and slide reflection are not applicable to subarray tiles due to the aperture orientation. Hence, only a limited number of patterns in the literature are applicable to subarrays. These are identified by their notation $pn11$ for $n = 2, 3, \ldots$ indicating non-reflective configuration. The parameter n is the tile's order of rotation, which is different from the design order of rotation L in Section 5.2.1 above, which is

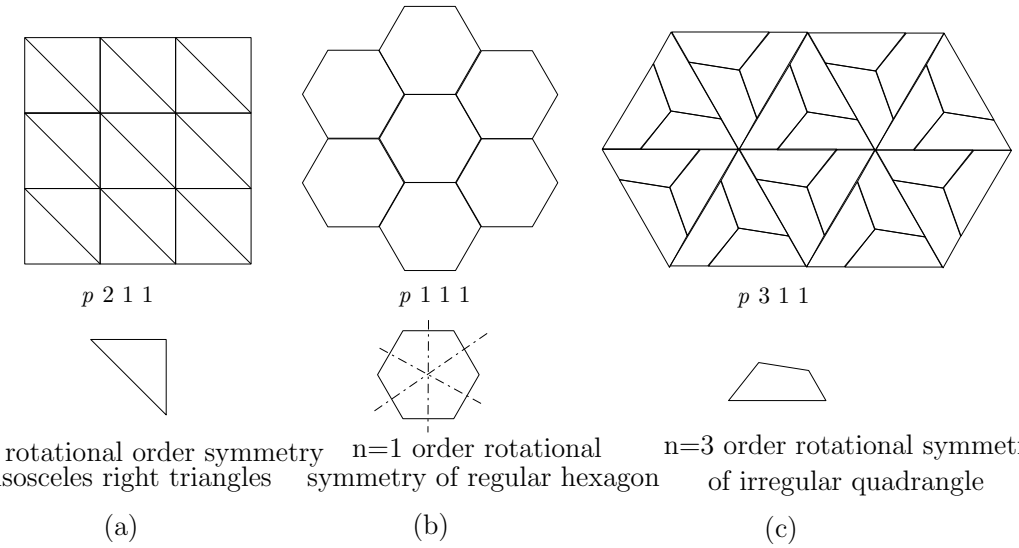

Figure 5.4: Examples of non-reflective tiling: (a) a simple $n = 2$ rotational design with rotationally asymmetric tile, (b) $n = 1$ design with 6-order rotationally symmetric tile and (c) $n = 3$ design with rotationally asymmetric tile.

the number of angles by which the base tile T_0 is rotated in a design. Non-rotational designs, where $n = 1$ in $p111$, have regular or equilateral polygons with uniform subarray spacing. These designs suffer from high grating lobes due to their rotational symmetry.

5.4 Tiling and Design Approach

There are three geometric aspects that affect grating lobes level and aperture efficiency in tiled arrays. These are the elements distribution, the subarray shape and the design, which is the way subarrays fit together. This section investigates these factors individually and introduces some performance measures.

5.4.1 Lattice Selection

The grating lobe locations follow the same pattern as the element lattice. The grating lobes derived in Section 5.1 belong to a square lattice. Another common lattice distribution is the Isosceles triangular lattice where every alternate row or column is shifted by half the element spacing. The elements in the Isosceles triangular lattice are located at $x = n_x d$, $y = n_y d$ for odd n_x and $y = (n_y - .5)d$ for even n_x. Figure 5.5 shows the

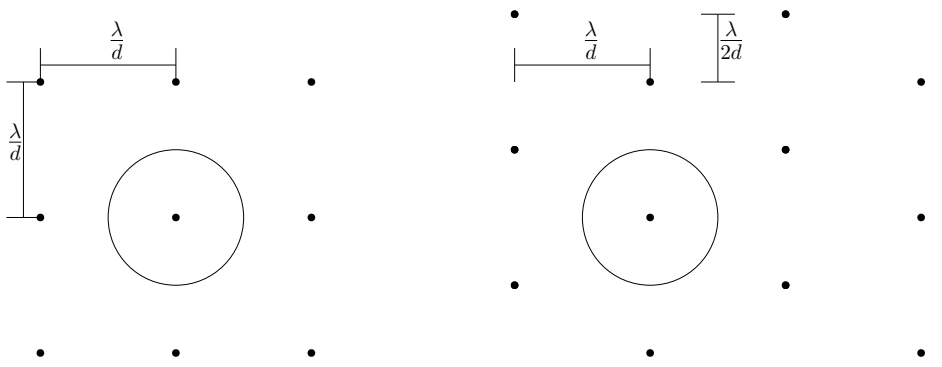

(a) Grating lobe locations in square lattice (b) Grating lobe locations in triangular lattice

Figure 5.5: Locations of grating lobes, shown as dots, and the visible region, shown as a circle, for (a) square and (b) Isosceles triangular lattices.

square and Isosceles triangular lattice with the element spacing in x and y axes. The array response of a planar array with a triangular lattice is

$$P(\omega,\theta,\phi) = \sum_{n_x=0}^{N_x-1}\Bigg[\sum_{\substack{n_y \\ 2n_y+1\in\mathbb{Z}}} \mathrm{w}(n_x,n_y)e^{-j[n_x-\frac{N_x-1}{2},n_y-\frac{N_y-1}{2}]\frac{\omega}{c}d\Delta\mathbf{k}} + \sum_{\substack{n_y \\ 2n_y\in\mathbb{Z}}} \mathrm{w}(n_x,n_y)e^{-j[n_x-\frac{N_x-1}{2},n_y-\frac{N_y}{2}]\frac{\omega}{c}d\Delta\mathbf{k}}\Bigg]. \tag{5.3}$$

An important aspect to consider when choosing the lattice is the rotational symmetry of the lattice itself. A rectangular lattice has a second-order symmetry with symmetry angles π and 2π. A square lattice has a forth-order symmetry at angles $\frac{\pi}{2}, \pi, \frac{3\pi}{2}, 2\pi$. The Isosceles triangular lattice described in figure 5.5 is rotational asymmetric hence it has a first-order of symmetry at 2π. An equilateral triangular lattice has a third-order rotational symmetry at angles $q\ \frac{2\pi}{3} \quad \forall\ q = 1, 2, 3..$ The rotational symmetry order of any equilateral polygon equals the number of its vertices and its symmetry angles are $\Psi_{lattice} = p\frac{2\pi}{v} \quad$ for $p = 1, \cdots, v$ where v is the number of vertices.

5.4.2 Tile Selection

All triangles and quadrilaterals can tile a plane [82]. But there are only 15 convex pentagons and three hexagons that can tile a plane without gap or overlap [83]. The

Table 5.2: Known convex isohedral polygons that can tile a plane.

polygon	known isohedrals	highest order of symmetry
triangular	all	3
quadrilateral	all	4
pentagonal	15	5
hexagonal	4	6
heptagonal&higher	none	> 6

most recent discovery in isohedral tiling is the 15th convex pentagon that can tile a plane, by Mr and Mrs Mann [84] in 2015. There are no known convex polygons beyond hexagons that can tile a plane. In fact, Ivan Niven [85] proved that there are no convex n-gons with n$\leq$ 7 that can tile a plane. Table 5.2 list the number of all known types of convex polygons that can tile a plane. The "highest symmetry" column indicates the highest order of rotational symmetry of the regular polygon.

When choosing a tile, the base tile should have the lowest rotational symmetry order possible. High rotational symmetry produces congruent tiles when the design rotates at one of the tile symmetry angles. Regular polygons should be avoided since they have the highest rotational symmetry order. The set of angles at which the base tile is symmetric is noted Ψ_{tile}. The order of rotational symmetry of a polygon can be obtained by finding the rotation angles that fulfills the congruency condition $\mathbf{V}\cdot\mathbf{R}_\theta = \mathbf{V}$ where $\mathbf{R}_\theta$ is the 2-D rotation matrix at angle θ, and $\mathbf{V}$ is the matrix of the vertices location.

The internal space of the tile should be sufficiently wide to contain subarray hardware and interconnections. This space can be characterized by the diameter of the incircle, which is the largest circle contained inside the tile, i.e. $c_{in} \geq \alpha_{in}$, where c_{in} is the incircle diameter and α_{in} is the minimum width to allow sufficient internal space.

5.4.3 Design Selection

The design is characterised by the set of transformations applied to the base tile to populate the plane. For periodic designs, these transformations are finite and defined by the closed set $\{\sigma_m\ , m = 1, \cdots, M\}$, and create the design as $\mathfrak{T} = \sum_{m=1}^{M} \sigma_m T_1$. The set of rotation angles in the closed set $\sigma_m,\ m = 1..M$ is $\{\Psi_{\text{design}} = \psi_l\ \ , \ l = 1, \cdots, L\}$

where L is the design order of rotation. An edge-to-edge tiling, also called isogonal, is where tiles vertices only meet other vertices. For tiled subarrays, edge-to-edge tiling provides a simpler structural frame and fewer joints between subarrays.

5.4.4 Survey of tiles suitable for array tiling

This section is a huristic attempt to create new array geometries based on properties of existing results from the tilling literature. The 15 convex pentagons that can admit isohedral tiling have been surveyed for suitability to antenna array by eliminating tiles that have reflective designs, have low order of rotation or have high rotational symmetry. Only pentagonal tiles are considered in the survey. Triangles and quadrangle are ignored due to the large number of possibilities for isoedral tiling, and due to the fact that higher order polygons have larger internal area, represented by the size of their incircles. Hexagons are also ignored because there are no convex polygons above pentagons that can admit an isohedral tiling higher than 3rd-order of rotation. Table 5.3 lists all known types of convex pentagons that admit an isohedral tiling. The pentagon angles are designated by capital letter A-E sequenced in counter-clockwise rotation. The pentagon edges are designated by small letters a-e sequenced in counter-clockwise rotation. Figure 5.8 demonstrated a model pentagon for reference. Notice that the i-block transitive in the third column is where the rotation order applies to i symmetric tiles instead of one, where i is number of tiles (blocks) acting transitively on each other as defined in [84].

From the review in table 5.3, type 1 and type 5 pentagons are possibly the most suitable tiles for antenna array design. These two types of pentagons will be further analysed for rotational symmetry, and instantiated to generate a new array designs in sections 5.5 and 5.6

5.4.5 Aperture Efficiency

The effective area of an antenna is the ratio between the power captured by the antenna to the total incident power [88]. Instead of calculating losses and power density, it is more convenient to compare the aperture of a tiled array with that of a circular array.

Table 5.3: Review of the 15 types of convex pentagons applicable for isohedral tiling.

Pentagon type	definition	highest order of rotation	design reference	comment
type 1	D+E=180°	6	[82]	suitable for array tiling
type 2	C+E=180° , a=d	2	[82]	low rotation order
type 3	A=C=D=120°, a=b, d=c+e	3	[80]	high rot. symmetry
type 4	A=C=90°, a=b, c=d	4	[80]	high rot. symmetry
type 5	C=2A=90°, a=b, c=d	6	[80]	suitable for array tiling
type 6	C+E=90°, A=2C, a=b=e, c=d	[1]	[86]	low rotation order
type 7	2B+C=360°, 2D+A=360°, a=b=c=d	2-block transitive	[86]	reflective designs only
type 8	2A+B=360°, 2D+C=360°, a=b=c=d	2-block transitive	[86]	reflective designs only
type 9	2E+B=360°, 2D+C=360°, a=b=c=d	2-block transitive	[87]	reflective designs only
type 10	E=90°, A+D=180°, 2B-D=180°, 2C+D=360°, a=e=b+d	3-block transitive	[84]	low rotation order
type 11	A=90°, C+E=180°, 2B+C=360°, d=e=2a+c	2-block transitive	[87]	reflective designs only
type 12	A=90°, C+E=180°, 2B+C=360°, 2a=c+e=d	2-block transitive	[87]	reflective designs only
type 13	A=C=90°, 2B+D=2E+D=360°, c=d, 2c=e	2-block transitive	[87]	reflective designs only
type 14	D=90°, 2E+A=360°, A+C=180°, b=c=2a=2d	2-block transitive	[84]	reflective designs only
type 15	A=60°, B=135°, C=105°, D=90°, E=150°, a=2b=2d=2e	2-block transitive	[84]	reflective designs only

Aperture efficiency is measured here as

$$\eta = \frac{K_{\text{tiled}}}{K_{\text{cpa}}} , \tag{5.4}$$

which is the ratio between the number of elements of a tiled array K_{tiled}, to that of a uniform circular array K_{cpa}, which has the same size as the circle enclosing the tiled array, or excircle. The excircle ratio is directly proportional to the effective area and hence the directivity. The circular array aperture size can be approximated as $K_{\text{cpa}} = \pi(\frac{D}{2d})^2$ where D is the circular array diameter.

5.4.6 Problem Formulation

Many combinations of tiles and designs can be found in the tessellation literature. Alternatively, tiling can be synthesised through a geometric optimisation approach. The geometric design can be obtained through an optimisation approach to find a polygon that tiles a plane without gaps or overlaps. In addition to the tiling constraint, the polygon is constrained to be rotationally asymmetric at lattice symmetry angles Ψ_{lattice} or the design rotation angles Ψ_{design}. The optimisation problem

$$
\begin{aligned}
\underset{V_i}{\text{minimize}} \quad & \frac{1}{L} && (5.5)\\
\text{subject to} \quad & \sum_{i=1}^{M} \text{Conv}(V_i) = \text{Conv}\big(\sum_{i=1}^{M} V_i\big) && \text{(no gaps)}\\
& \text{Conv}(V_i) \cap \text{Conv}(V_j) = \emptyset, \ \ \forall \ \ i \neq j && \text{(no overlaps)}\\
& (\Psi_{\text{tile}} \cap \Psi_{\text{lattice}}) \cap \Psi_{\text{design}} = \emptyset && \text{(no alignments)}\\
& \eta \leq 0.7 && \leq \text{(70\% aperture efficiency)}
\end{aligned}
$$

is an example of a subarray geometric design that minimizes the grating lobes level by maximizing the design rotation angles, while avoiding rotational symmetry of the tile or the lattice at these angles. The variable V_i , $i = 1 \cdots M$ is the set of vertices of the polygon tile T_i and $\text{Conv}(\sum_{i=1}^{M} V_i)$ is the convex hull of all tiles vertices. Notice that $\sum_{i=1}^{M} \text{Conv}(V_i)$ excludes the area between the internal circle and the external circle which is included in the convex hull defined by $\text{Conv}(\sum_{i=1}^{M} V_i)$. Although the geometric outline of the base tile is convex, finding a tiling design introduces concave constraints to leaves no gaps or overlaps. The edge-to-edge alignment of the tiles, to avoid gaps or overlaps, is external the convex tile outline, making it a non-convex constraint. The

design rotation angles and the tile's rotational symmetry constraint are transformation operations and have no effect on the problem convexity. Due to the difficulty of solve such optimisation problem, we will rely on the current literature to derive candidate array structures. This chapter is a heuristic attempt to create new array geometries based on properties of existing results from the tilling literature.

5.4.7 Symmetry Detection and Measurement

Section 5.2.1 pointed out that the base tile and the elements lattice should not be rotationally symmetric at any of the design rotation angles. It is not always obvious if a tile is rotationally symmetric and at what angles. But there are many algorithms in computational geometry and image processing that can detect and compute an image symmetry. For example, the scale-Invariant Feature Transform (SIFT) identifies and describes features in an image, then matches pairs of symmetric features [89]. Gradient Vector Flow (GVF) is used in [90] to obtain the directional derivatives of all points in an image to extract symmetric constellations. These methods can resolve multiple symmetric features in an image but suffer from high computational complexity. A simplified approach adapted from [76] is applied here to the subarray outline and elements lattice to detect and measure rotational symmetry, which is comprised of the following steps:

1. Locate the centre of rotation or centroid.
2. Apply frieze expansion around the centroid.
3. Obtain the autocorrelation to the frieze model.

When applied to subarray tiling, symmetry detection is tested on the base tile instead of the entire design. Hence there is only one centre of rotation in the image. The base tile is represented by its edges as a polygon. The centre of rotation C of a polygon is its centroid [90] which is calculated as $C = \frac{1}{v}[\sum_{i=1}^{v} \mathbf{v}_x, \sum_{i=1}^{v} \mathbf{v}_y]$, where $\mathbf{v}_x$ and $\mathbf{v}_y$ are the x and y components of the vertices location matrix $\mathbf{V}$.

Frieze expansion is the transformation of the image from the Cartesian coordinates to the polar domain around the centre of rotation. The frieze expansion of the polygon

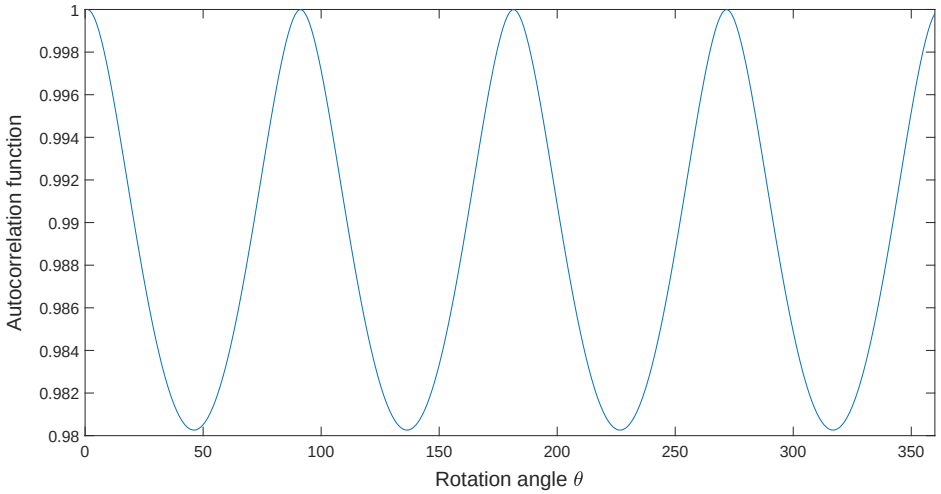

Figure 5.6: Autocorrelation of the frieze model of a square tile. The square tile is rotationally symmetric at $90°, 180°, 270°$ and $360°$.

is

$$\mathbf{v}_r = \sqrt{(\mathbf{v}_x - C_x\mathbf{1})^2 + (\mathbf{v}_y - C_y\mathbf{1})^2} \tag{5.6}$$
$$\mathbf{v}_\theta = \tan^{-1}((\mathbf{v}_y - C_y\mathbf{1})/(\mathbf{v}_x - C_x\mathbf{1}))\ ,$$

where $\mathbf{1}$ is a column vector of size v, and $\tan^{-1}$ is the four-quadrant inverse tangent. Finally, the frieze model is correlated with a translated copy of itself to obtain the autocorrelation function $\mathbf{A}_r(\theta) = [\mathbf{v}_\theta, \mathbf{v}_r]$. Rotational symmetry exists if the autocorrelation function has peaks other than $\mathbf{A}_r(0)$ and the symmetry angles are the location of these peaks, i.e.

$$\Psi_{\text{tile}} = \{\theta_i\ ,\ \mathbf{A}_r(\theta_i) = \mathbf{A}_r(0)\}\ . \tag{5.7}$$

Figure 5.6 shows the autocorrelation of a frieze model of a simple square with vertices at $(0,0), (0,1), (1,0)$ and $(1,1)$.

5.5 Design case 1: Rice Tile with a sixth-order Design

To demonstrate grating lobe suppression, we use the type 5 pentagon tile and design introduced by Marjorie Rice [80] shown in figure 5.7. The tile is rotationally asymmetric

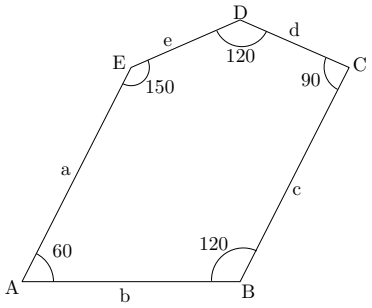

Figure 5.7: A pentagon that can tile a plane without gaps or overlaps. The tile is rotationally asymmetric, i.e. its rotated copies are not congruent to the original tile.

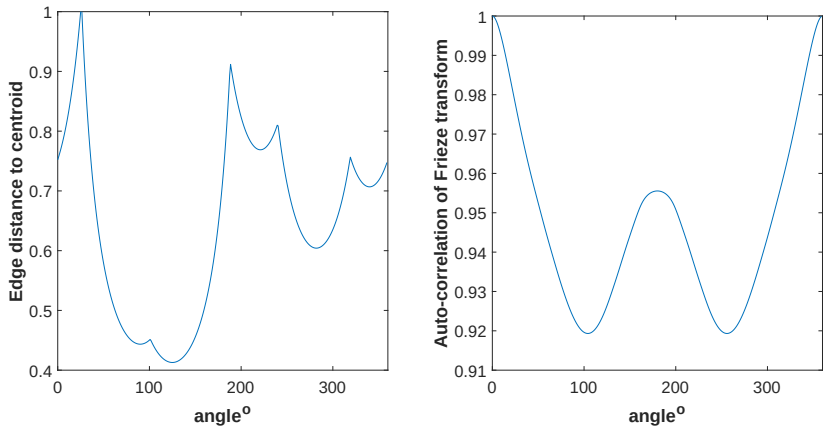

Figure 5.8: Rotational symmetry analysis of the tile in figure 5.7. The tile is rotationally asymmetric but have partial symmetry at 180^o. (a) Frieze expansion of the tile edges (b) Autocorrelation of the frieze expansion.

but has partial symmetry at 180 ^{o} rotation angle.

The array contains 18 subarrays with 50 elements each. The design has 6 rotation angles $L = 6$. Hence, there are three subarrays sharing the same rotation angle. Figure 5.9 shows 18 Rice's subarrays tiled into a star-shaped aperture. The different colours are to help distinguish subarrays. The tiled array is compared to a circular planar array of the same number of elements and the same element spacing and lattice. The red circle encloses all elements of the tiled array plus a margin of a half element spacing. The blue circle is the size of a circular planar array containing the same number of elements. The tiled array has an excircle diameter of $18.15d$ while the

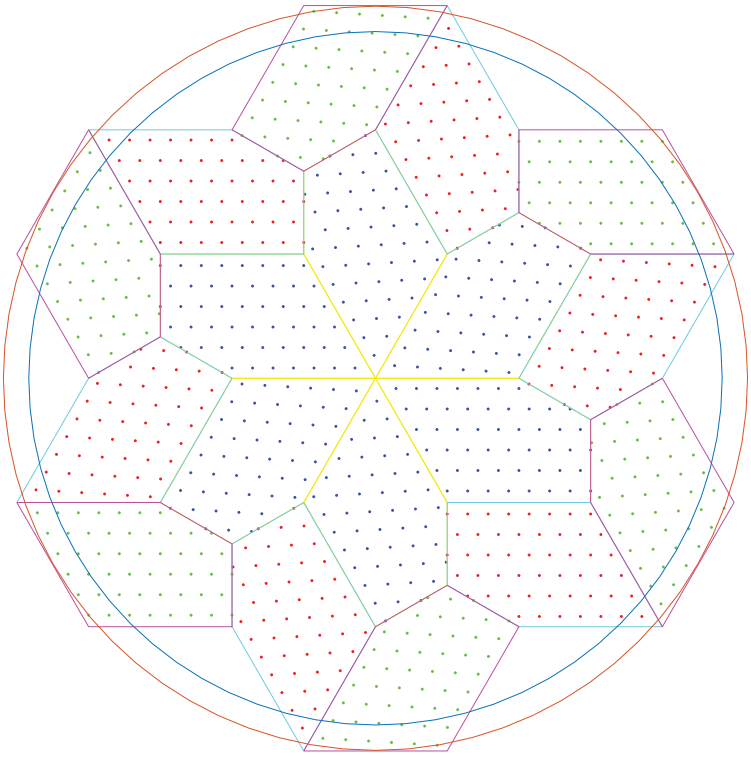

Figure 5.9: Tiled array constructed using 18 subarrays shaped like Rice's tile. The red circle encloses all tiled array elements, while the blue circle encloses the circular array which have the same number of elements.

circular uniform array excircle is $16.88d$. The grating lobes are shown for the circular planar array in figure 5.10, and for the tiled array in figure 5.11. Grating lobes locations in a triangular lattice have a triangular distribution. Both arrays follows the same locations and distribution of grating lobes. However, the tiled array has lower grating lobe levels and more dispersed gain around the grating lobe locations and on the lines connecting these locations. Figure 5.12 shows the grating lobes of both arrays across the horizontal dimension of the $\Delta\mathbf{k}$–axis where $\Delta\mathbf{k} = \mathbf{k} - \mathbf{k}_0$ and $\mathbf{k}$ is the wavenumber vector defined in (2.18).

The reduction in grating lobe levels is not significant because the 180^o rotational symmetry of the element lattice coincides with the design rotation angle of 180^o. This reduces the grating lobes limit to a third or -10.9dB. However the response shows an additional -7.7dB grating lobe next to the expected -10.55dB grating lobe at $\Delta\mathbf{k} =$

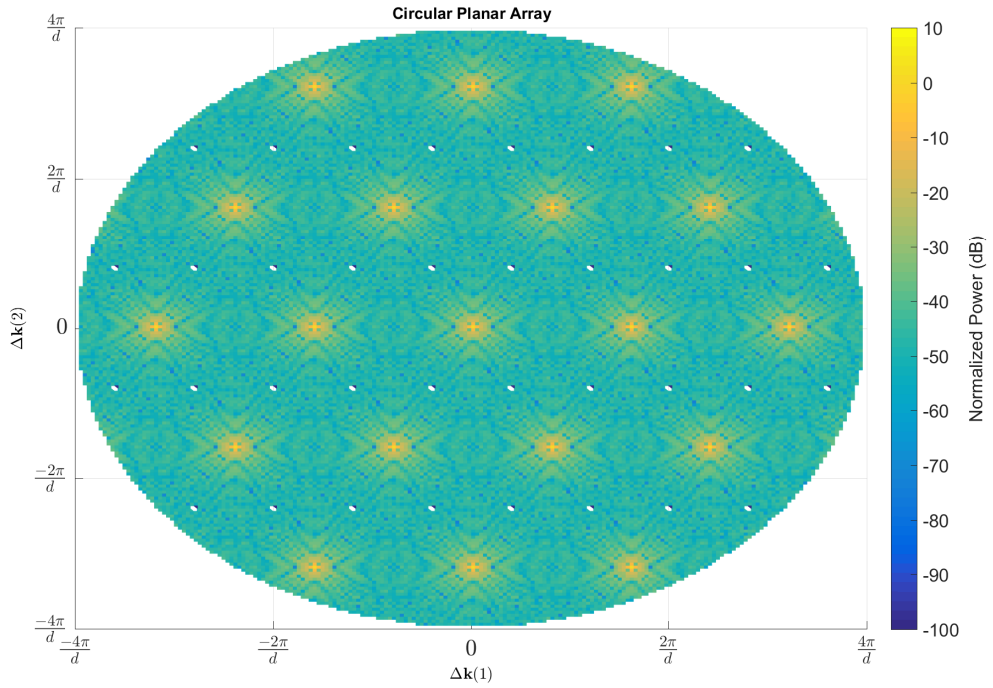

Figure 5.10: Grating lobes of the circular array containing 900 elements distributed uniformly on a triangular lattice.

Table 5.4: Comparison summary between the tiled array and the uniform circular array of design case 1.

property	tiled array	circular planar array
number of elements	900	900
diameter	$18.15d$	$16.88d$
grating lobe level	-7.7dB	0dB
beamwidth	7°	7°
directivity	31.08dBi	31.42dBi

$\pm\frac{2\pi}{d}$. This indicates that the array response at the minor grating lobes is not only the contribution of the grating lobes from a subset of the subarrays, but also the sidelobes of the remaining subarrays,

Table 5.4 summarizes the sizes and the beam pattern characteristics of the tiled array and the benchmark circular planar array. By examining the tiled array response in figure 5.11, the grating lobes formation is more dispersed than that of the uniform

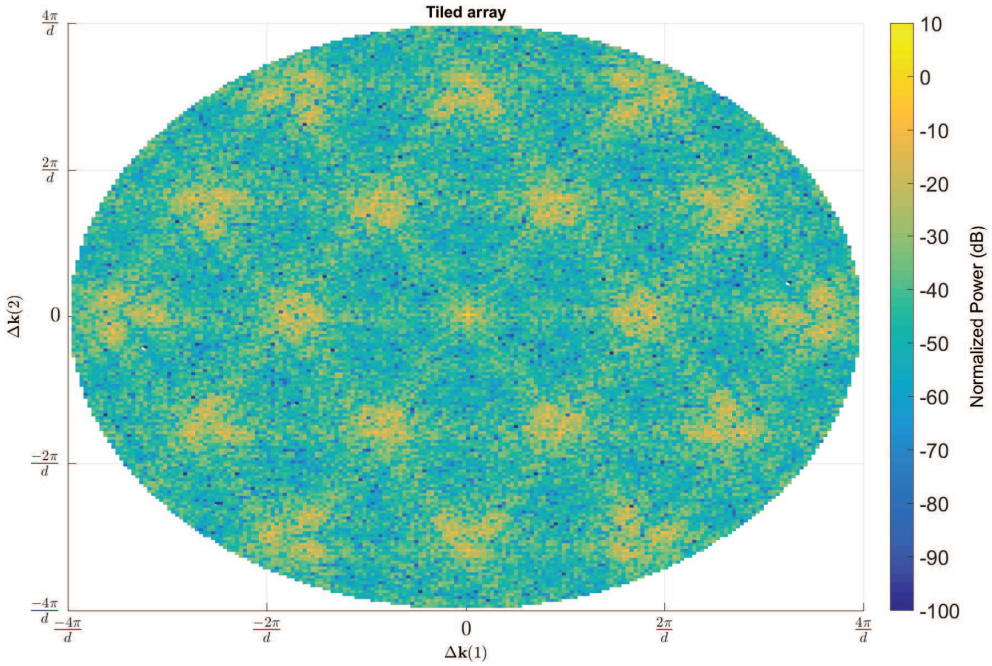

Figure 5.11: Grating lobes of the tiled array built using Rice's tile. The array contain 900 elements distributed uniformly with triangular lattice.

circular array. There are also lines of high gain that connect the grating lobes. This could be due to an interaction between the subarrays grating lobes and the random subarrays spacing which slightly shifts the location of the subarray grating lobes without changing the spacing between its peaks.

5.6 Design case 2: Equilateral Pentagon Subarray

The tiling concept for subarrays is further demonstrated using an aperiodic pattern suggested by [82] based on a type 1 equilateral pentagon as described in [80]. Shown in figure 5.13 is an equilateral pentagon that has interior angles of $\alpha = 140°$, $\beta = 60°$, $\gamma = 160°$, $\delta = 80°$ and $\epsilon = 100°$ respectively. A type 1 equilateral pentagon has one degree of freedom derived from the equality $\delta+\epsilon = 180°$. The angle ϵ can take any value between 60^o and 120^o. Beyond this range the polygon loose its convexity. This tile is an opportunity to study the effect of design parameters, like the angles and the edges' lengths, on the rotational symmetry. The rotational symmetry strength is represented by the auto-correlation of the frieze transform. It is shown for this tile in figure 5.14

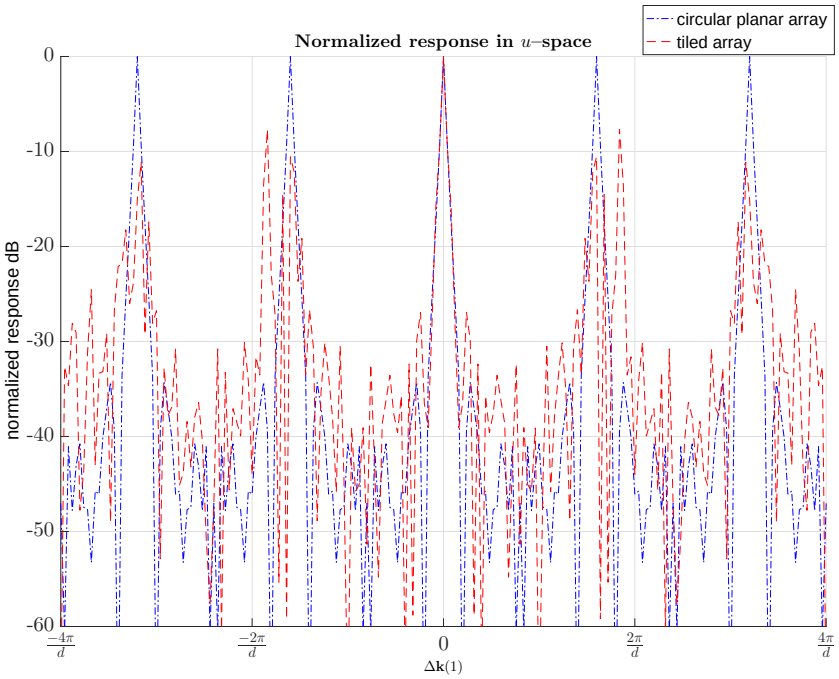

Figure 5.12: Grating lobes along u-space for both arrays of example 1. The tiled array have a lower grating lobe level at -7.7dB. The bandwidth shown in the graph is four times wider than the bandwidth allowed by the element spacing.

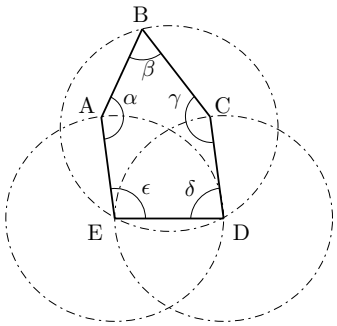

Figure 5.13: Type 1 equilateral pentagon with $\delta + \epsilon = 180°$. Vertices A, B and C can be moved along the circles while maintaining parallel sides AE and CD. ABC is an equilateral triangle and ACDE is a rhombus.

for values of ϵ ranging from 90^o to 120^o. Varying ϵ from 90^o to 60^o is omitted because it produces a reflection symmetry w.r.t. values from 90^o to 120^o. Figure 5.14 shows that low rotational symmetry can be obtained for$\epsilon + \delta = 90^o$. This however may come at the cost of the design's rotation order. Also, many designs require a specific values of ϵ such as the design used in design case 2. In figure 5.15, 18 pentagons of the type

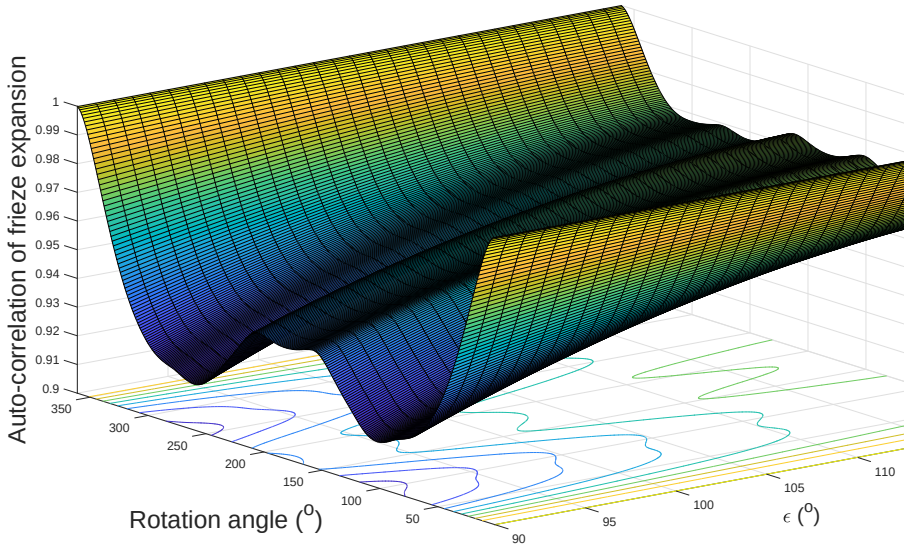

Figure 5.14: The rotational symmetry strength of the equilateral polygon in design case 2 computed w.r.t to ϵ. Notice that at rotation angles 0^o and 360^o the tile does not rotate hence rotational symmetry is a unit value.

shown in figure 5.13 construct an approximately circular array. Each subarray contains 42 array elements arranged on a square lattice, whereby the element spacing d is half the wavelength at the operating frequency f_c. Therefore, across the 18 subarrays the total number of array elements is 756.

The tiled array requires a small separation between subarrays as seen in figure 5.15 to account for subarrays boundaries. Also, the tiled array circumference is a series of straight edges that does not constitute a perfect circle. It can however be inscribed in a circle of radius $15.62d$. We compare the tiled array in figure 5.15 with a uniform circular array having square elements lattice as shown in figure 5.16. Both the circular array and the tiled array contain the same number of elements.

Due to the lack of internal subarray boundaries, the circular array is smaller in diameter compared to the tiled array. The uniform circular array of figure 5.16 has a $15.51d$ radius vs. $15.62d$ for the tiled array, if both arrays are circumscribed by a circle.

Figure 5.17 demonstrates that spatial aliasing occurs when the uniform array op-

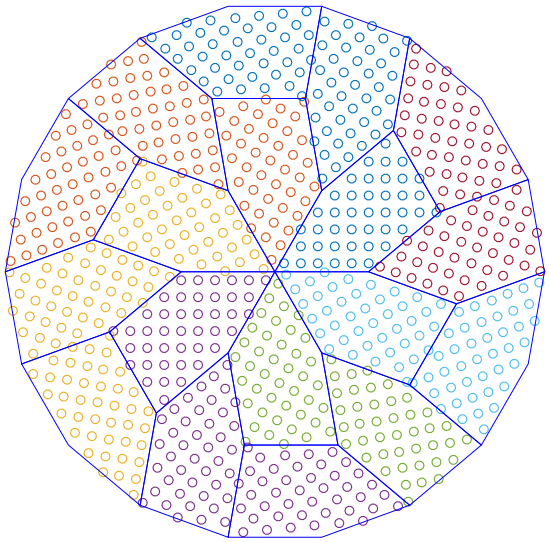

Figure 5.15: Tiled array constructed by rotation and displacement of 18 pentagon subarray tiles each containing 42 sensor elements. The array is contained within an outer circle of radius 15.62 d.

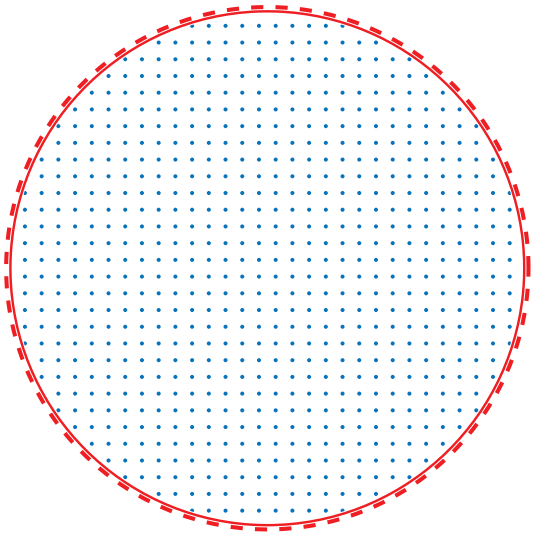

Figure 5.16: A uniform circular array containing 756 elements. Solid and dashed circles circumscribe the uniform circular array and the tiled array, respectively. Notice how the tiled array is slightly larger than the circular array.

erates beyond the maximum frequency where the element spacingis half the signal wavelength. This leads to the grating lobes appearing at integer multiples of $\frac{2\pi}{d}$ in both u and v directions, as shown in (2.21) for a uniformly spaced array.

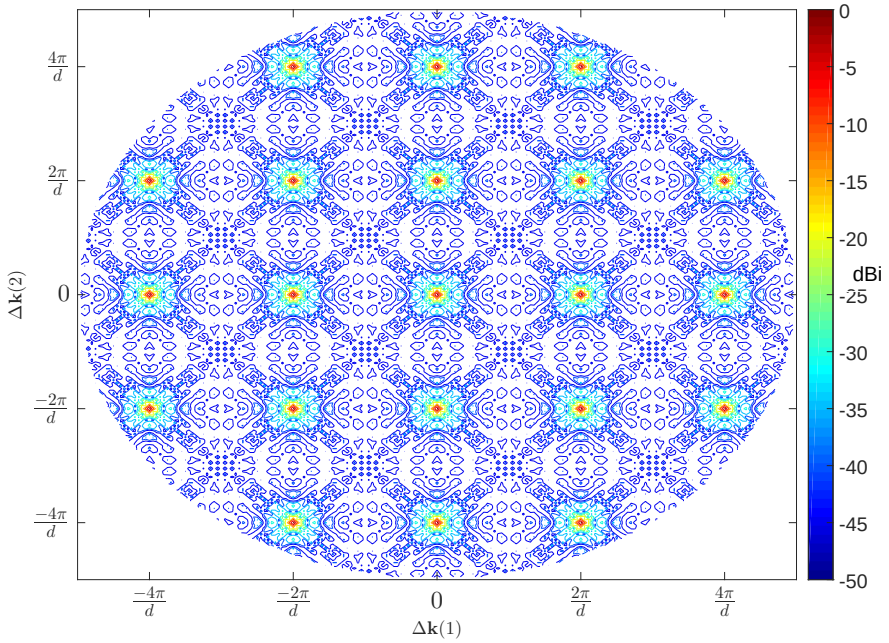

Figure 5.17: Grating lobes of the uniform circular array from design case 2.

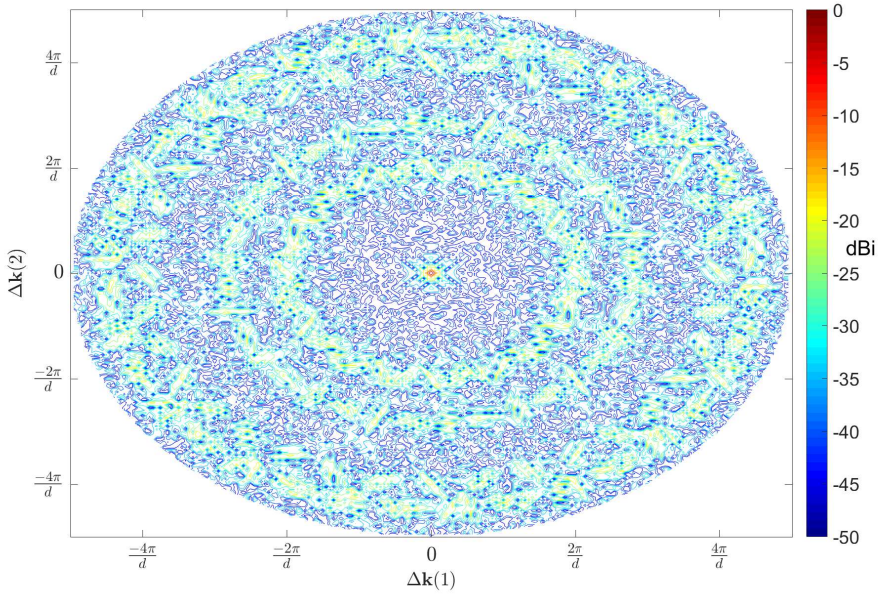

Figure 5.18: Grating lobes of the tiled array of design case 2 showing the dispersion and reduction of grating lobes compared to the circular array characterised in figure 5.17.

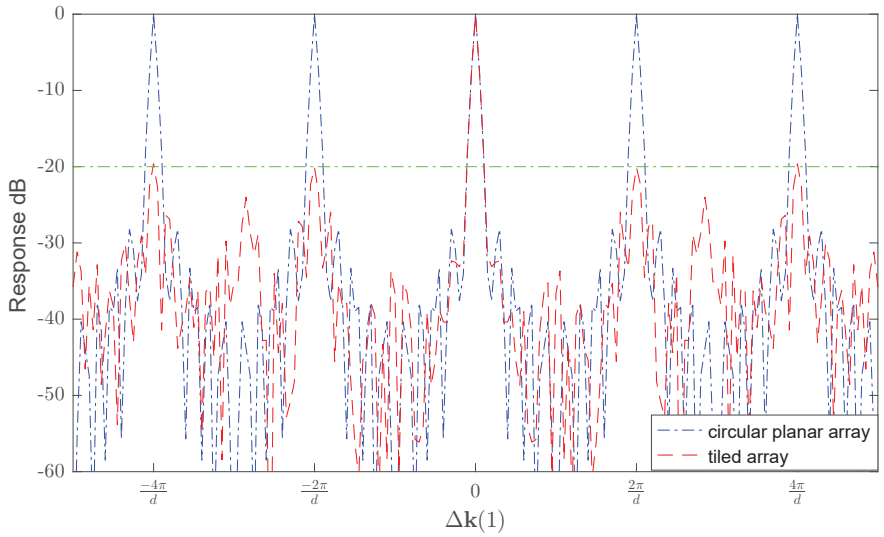

Figure 5.19: Grating lobes along the $u = \sin\theta$ domain of both the circular array in blue dot-dash line, and the tiled array in red dashed line. The tiled array shows 20 dB reduction in grating lobes.

By contrast, the gain response of the tiled array in figure 5.18 shows the destructive superposition of subarray grating lobes. The distance between minor grating lobes and the mainlobe is unchanged at $\frac{2\pi}{d}$ because the element spacing is the same across subarrays. But the subarray rotation by the angles ψ_l in (5.1) causes grating lobes to rotate by the same angles around the mainlobe.

To directly compare the two gain responses, a cross-section of the first component of $\mathbf{\Delta k}$ for both the uniform circular and proposed tiled array are shown in figure 5.19. The graphs show the grating lobes of the uniform circular array with a periodicity of $\frac{2\pi}{d}$ and a level of 0dB. By contrast, the gain response of the proposed tiled array has a reduced grating lobe level at -20dB. The mainlobe beamwidth is approximately the same in both cases. Table 5.5 summarizes the comparison between the uniform circular array in figure 5.16 and the proposed tiled array in figure 5.15.

As the analysis in Section 5.2 indicated, the grating lobes of the tiled array decreases with the increase of design rotation angles. However, a high rotational symmetry of the subarray or the element lattice may cause grating lobes from subarrays to coincide. The tiled array response in figure 5.19 is suppressed by -20dB or to one-tenth of the mainlobe level. This can be traced to the rotational symmetry of the square lattice w.r.t. 180°,

Table 5.5: Comparison summary between the tiled array and the uniform circular array of design case 2.

property	tiled array	circular planar array
number of elements	756	756
diameter	15.62 d	15.51d
grating lobe level	-20 dB	0 dB
beamwidth	7°	7°
directivity	30.6 dBi	30.7 dBi

which is a design rotation angle at $3\beta = 180°$. The number of unique design rotation angles in figure 5.15 is 9. This is due to the rotational symmetry of the square lattice around 180° which is a design angle. Therefore grating lobe suppression is expected to be around $\frac{1}{9}$. Table 5.5 shows that the grating lobes have reduced significantly while the directivity and beamwidth are unaffected. This is expected because both directivity and beamwidth depend only on the number of sensors and their separation only.

5.7 Conclusion

Previous chapters have dealt with the beamforming of uniformly spaced arrays. In contrast, this chapter has proposed a novel planar array design that can reduce grating lobesby rotational tiling without introducing randomness or variations in the elements placement or the subarrays outline.

Utilising rotational tiling in array design can introduce variance in both subarray phase centres and sensors locations. This variance results from the rotation and placement of rotationally asymmetric subarrays into a pattern that leaves no gaps or overlaps. Rotationally tiled subarrays can significantly reduce grating lobes by disrupting the alignment of subarrays grating lobes. This potentially allows spacing the elements further apart to avoid mutual coupling, or utilising fewer elements while maintaining the same aperture size. Rotational tilling, however, increases the array size due to the potentially irregular outer edges of the array and the clearance required for subarray boundaries.

The tiling literature is rich in tile outline and design combinations that can tile a

plane without gaps or overlaps. In this chapter, these combinations have been reviewed and two tile outlines have been found to be most suitable for antenna array design. Geometric tools and measures are introduced to assess symmetry alignments. The grating lobes are calculated for an isohedral pentagon tile and design to demonstrate the rotational tiling. Additionally, we have formulated the geometric design as an optimisation problem that can be used to discover a tile and design combination that can be tailored to specific requirements such as shape and density of the subarrays and the outline of the overall array. However, the optimization of problem is found to be difficult to solve due to the lack of convexity in the problem objective function and constraints.

Finally, two cases of tiles from the literature are used for the subarray design. The highest grating lobe of the first design case is -7.7dB below the main lobe which is higher than the expected reduction of -9.5dB or $\frac{1}{3}$ below main lobe. The grating lobes level of the second design case is -20dB. This is close to the expected -19dB or $\frac{1}{9}$ reduction for a design with 9 unique rotation angles. The expectation of overall array grating lobe levels are based on the subset of subarrays which coincide in their grating lobes locations. Therefore, the difference between the calculated and the expected levels can be due to the gain contribution of the rest of the subarrays.

Compared to a circular uniform array containing the same number of sensors, the beamwidth and directivity of the tiled design in both case studies are nearly unaffected, because the aperture and the number of elements are comparable.

The tiled array has the same directivity as a uniform array of the same size, but the power that used to be in the grating lobes is re-distributed so that the grating lobes of the subarrays do not necessarily add up constructively. Therefore, it is possible to design arrays with an element spacing that is wider than half the wavelength of the maximum frequency, be it to reduce cost or eliminate mutual coupling between sensor elements, or to operate an existing array at a wider bandwidth without incurring spatial ambiguity.

Grating lobe formation limits the bandwidth of uniformly spaced wideband arrays buy limiting the maximum operable frequency [91]. The tiled array only addresses

the grating lobe issue. When tiling is combined with the signal processing techniques introduced in Chapter 3, the array bandwidth can approach that of a wideband array with only M TDLs or TDUs instead of N, where M and N are the number of subarrays and the number of elements respectively.

Chapter 6

Summary and Future Work

6.1 Summary

In this thesis, we have investigated wideband data-independent beamforming techniques for partial wideband arrays. The general structure of the partial wideband array was a linear or a planar array consisting of a plurality of subarrays. The array elements are attached to a narrowband complex-valued weight consisting of a scalar multiplier and a phase shifter. Subarrays can be virtually defined, as in section 4.2, or attached to either time delay units, as in section 2.6, or fractional delay filters, as in chapters 3 and 4. The partial wideband array structure in this study gradually progressed in complexity and sophistication from a linear array structure with narrowband optimized weights at the look direction only in chapter 3, through an partial wideband array with wideband mainlobes alignment and adaptive noise cancellation in chapter 4, to the full structural design and integration of subarrays that suppresses grating lobes in chapter 5.

In chapter 2, we have prepared the background for the research by reviewing antenna array geometries, architecture and pattern characteristics. We then presented wideband beamforing and frequency-invariant components and reviewed wideband beamforming techniques. Three ways to implement wideband beamforming on partial wideband arrays were subsequently investigated, where location alignment, segregated subarrays and phase separation were discussed. These approaches were applied using eigenfilter

beamformers and evaluated against directivity, beamwidth, beam squinting and sidelobe level. We concluded that applying wideband beamforming separately to individual subarrays leads to higher gain and lower sidelobe levels compared to the other methods. The bandwidth of all methods is approximately M times wider than the narrowband array equivalent, where M is the number of subarrays.

In chapter 3, we investigated the use of fractional delay filters in delay-and-sum beamformers. We have demonstrated, using a uniform linear array, that choosing the median frequency of the band of interest for beam-steering does not always leads to the flattest mainlobe response across the band. After that the fraction delay filter was combined with the narrowband elements weights to minimize the variation of the mainlobe response. This resulted in a flat mainlobe spectral response but with increased sidelobe level.

In chapter 4, we have proposed tapering the element phase shifts of a partially adaptive subarray to reduce beam squinting. The results showed that when combining the FDF filtered subarrays outputs, the mainlobes are aligned toward the desired direction but with a slight deviation of the mainlobe around the subband transitions. Then we investigated the signal decorrelation between subarrays when phase windowing is applied to the overall array with a signed rectangular window. The subarrays outputs showed a level of isolation between the spectral components of the signal. Building on the subarrays isolation, a subband adaptive noise cancellation is proposed using the subbands other than the those containing the desired signal in the subarrays outputs.

In chapter 5, we reviewed the tiling, as a field of geometric tessellation, and applied the tilling concept to the subarray outline, the elements lattice and the integration into the array aperture. The aim was to reduce the grating lobe level while maintaining modularity and aperture efficiency. The problem was then formulated into a geometric optimisation problem that can be used to achieve specific requirements. However the optimisation problem is modeled with a non-convex objective function and constrains, hence has been challenging to solve. A measure of the rotational symmetry of tiles and tessellations was introduced, to identify the grating lobe distribution of arbitrary subarray shapes. This analysis was underpinned by two illustrative examples, in

which, at a minimal cost to aperture efficiency, grating lobes were shown to be reduced substantially.

6.2 Future work

The novel aspects of combining narrowband subarrays with wideband processing, as well as the construction of tiled subarrays has opened several routes for further research. Two of these appears particularly promising and are briefly discussed below. The subband adaptive noise cancellation that follows a phase-tapered linear subarray from Chapter 4, and the exploration of new tiles that can tile a finite aperture without gaps or overlaps in Chapter 5.

Section 4.5.2 proposes a subband adaptive noise cancellation that benefits from the cross-frequency signal isolation between subarrays outputs as demonstrated in Section 4.4. The subband adaptive noise cancellation structure offers a wideband array that offers flat wideband gain and noise rejection.

However, the proposed structure suffers from signal cancellation at some channels due to high correlation between subarrays output and the subarray output intended as the noise source. To be able to avoid signal cancellation, we suggest pursuing the following treatments:

- Increase the phase window curvature by changing the window type or increasing the truncation limits.
- Increase the number of subarrays. This increases the spatial channels and hence improves the spectral decomposition of the subarray output.
- Create orthogonality between the subarrays by minimizing gain outside the subarray band while maintaining a unit response at the subarray frequency. This is only required for the subarrays intended as noise sources. For example, the first subarray gain $P_1(\omega, \theta)$ which is intended to cover the lowest subband centred at

ω_1 can be further processed to meet the condition:

$$\text{minimize } P_1(\omega, \theta_0) \ \ , \omega \in [\omega_L \ , \ \frac{\omega_L + \omega_H}{2}]$$
$$\text{subject to } P_1(\omega_1, \theta_0) = 1 \ .$$

Likewise, the last subarray can have a similar condition on the lower half of the frequency band.

Chapter 5 demonstrates rotational tiling using two examples found in the Geometry literature. New subarray outlines and aperture designs, that minimizes grating lobes while maintaining high elements density, can be found. The exploration efforts in the field of Geometry are not concerned with increasing rotation order or with elements distribution. A guided search in the field of antenna array design can lead to new useful congruent tiles and designs for subarrays. Alternatively, Section 5.4 provides a numerical optimisation guide and a tool for detecting and measuring congruency in complex tiles that can be used to create new tiles and designs suitable for antenna arrays.

Appendix A

Graphs of Wideband Beamforming Application on Subarrays

This appendix lists the graphs where wideband eigenfilter beamforming is applied on different subarray configurations in Section 2.6. These graphs are used to obtain Figures 2.13 to 2.17 and the subsequent conclusions. These graphs are the array responses in angle versus frequency for three subarray structures and three subarray beamforming methods.

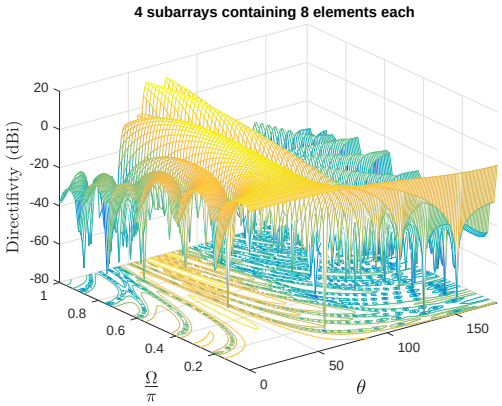

(a) Eigenfilter beamformer applied using location alignment.

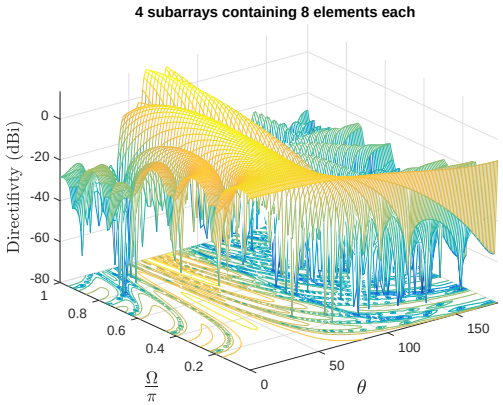

(b) Eigenfilter beamformer applied using segregated subarrays.

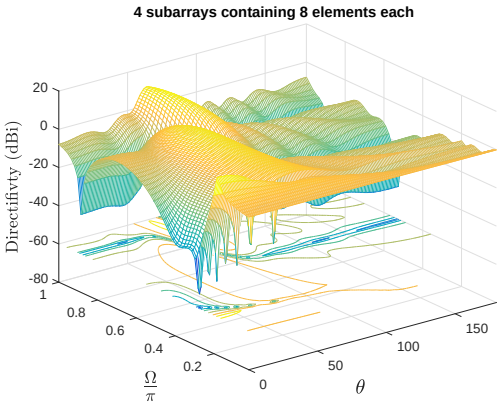

(c) Eigenfilter beamformer applied using phase separation.

Figure A.1: linear array response using Eigenfilter beamformer using the three approaches on an array containing 4 subarrays each containing 8 elements. The angle of arrival is 45^o.

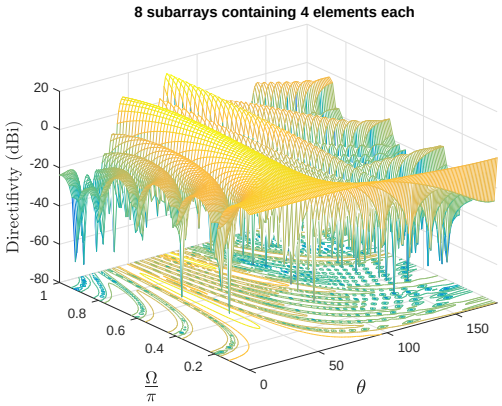

(a) Eigenfilter beamformer applied using location alignment.

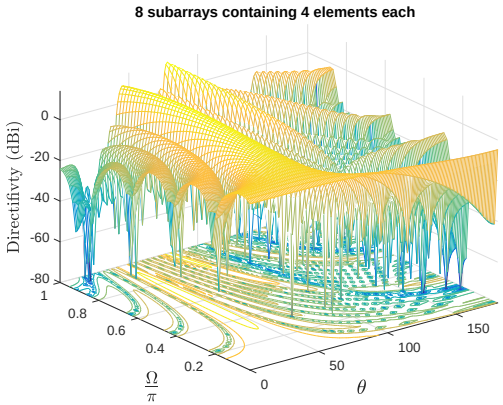

(b) Eigenfilter beamformer applied using segregated subarrays.

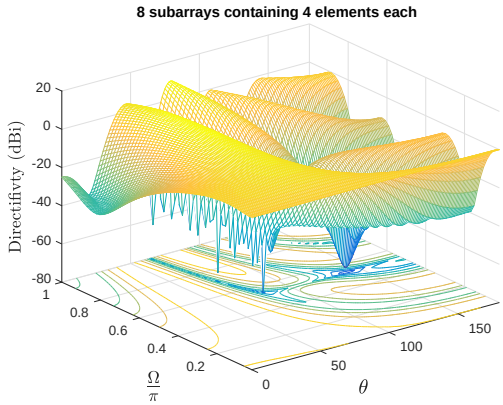

(c) Eigenfilter beamformer applied using phase separation.

Figure A.2: linear array response using Eigenfilter beamformer using the three approaches on an array containing 8 subarrays each containing 4 elements. The angle of arrival is 45^o.

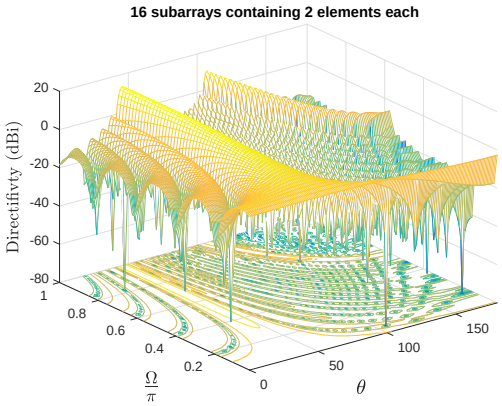

(a) Eigenfilter beamformer applied using location alignment.

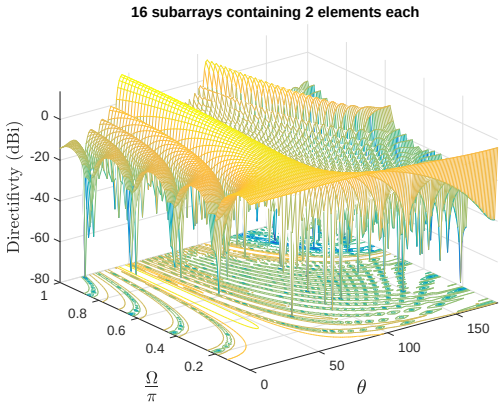

(b) Eigenfilter beamformer applied using segregated subarrays.

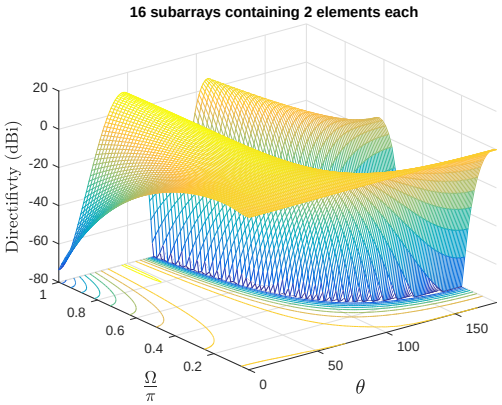

(c) Eigenfilter beamformer applied using phase separation.

Figure A.3: linear array response using eigenfilter beamformer using the three approaches on an array containing 16 subarrays each containing 2 elements. The angle of arrival is 45^o.

Appendix B

Phase-Windowed Linear Array Response Derivations

This appendix shows the derivation of (4.9) which is the response of a linear array with the generic Hamming window applied to its phase shifts. In the following, the array response, as a result of a generic Hamming windowing is obtained by substituting the generic Hamming window in (4.8) into (4.6).

$$P(\omega,\theta)=\frac{\mathbf{h}(k)}{\sqrt{K}}\sum_{k=0}^{K-1}e^{-j\ (k-\frac{K-1}{2})\ \frac{d}{c}\ (\omega\sin\theta-g(k)\omega_0\sin\theta_0)} \tag{B.1}$$

First, the exponent of (4.6) is expanded into four complex exponentials.

$$e^{-j\ (k-\frac{K-1}{2})\ \frac{d}{c}\ (\omega\sin\theta-g(k)\omega_0\sin\theta_0)} \tag{B.2}$$

$$=\frac{e^{-j\ k\ \frac{d}{c}\ \omega\sin\theta}}{e^{j\ k\ \frac{d}{c}\ A\omega_0\sin\theta_0}e^{j\ k\ \frac{d}{c}\ B\sin[\pi(\frac{k}{K}+\frac{1}{2K})]\omega_0\sin\theta_0}}\frac{e^{j\ \frac{K-1}{2}\ \frac{d}{c}\ \omega\sin\theta}}{e^{-j\ \frac{K-1}{2}\ \frac{d}{c}\ A\omega_0\sin\theta_0}e^{-j\ \frac{K-1}{2}\ \frac{d}{c}\ B\sin[\pi(\frac{k}{K}+\frac{1}{2K})]\omega_0\sin\theta_0}} \tag{B.3}$$

The exponents are then collected into one complex exponential.

$$e^{-j\ (k-\frac{K-1}{2})\ \frac{d}{c}\ (\omega\sin\theta-g(k)\omega_0\sin\theta_0)}$$

$$=e^{-j(2k+K+1)\frac{d}{c}(\omega\sin\theta+A\omega_0\sin\theta_0+B\omega_0\sin\theta_0\sin[\pi\frac{2k+1}{2K}])} \tag{B.4}$$

The resulting polynomial is substituted into Equation 4.6. The response of a linear array with the generalized Hamming phase window is

$$P(\omega,\theta)=\sum_{k=0}^{K-1}\frac{h(k)}{\sqrt{K}}e^{-j(2k+K+1)\frac{d}{c}(\omega\sin\theta+A\omega_0\sin\theta_0+B\omega_0\sin\theta_0\sin[\pi\frac{2k+1}{2K}])}\ . \tag{B.5}$$

Appendix C

Subarrays Isolation in a Triangular-Windowed Array

This appendix shows the response of the two subarrays in the triangular-windowed partial widenband array in Section 4.4.

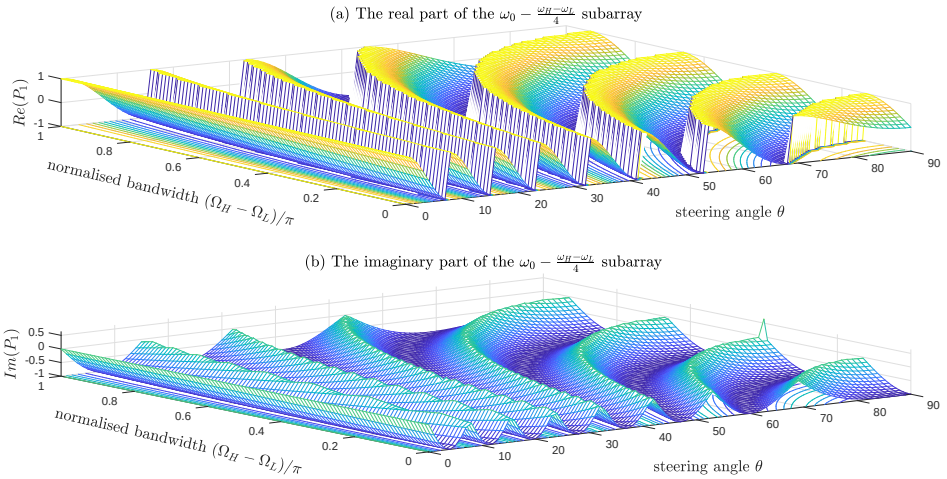

Figure C.1: The response of the lower band subarray (tuned at the reference frequency $\omega_0 - \frac{\omega_H - \omega_L}{4}$) in response to a lower band signal, (a) real-valued and (b) imaginary-valued.

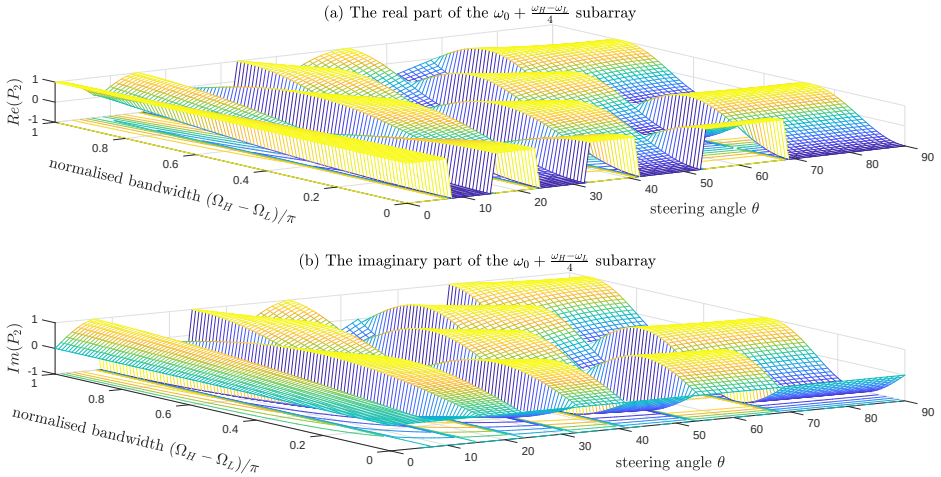

Figure C.2: The response of the upper band subarray (tuned at the frequency $\omega_0 + \frac{\omega_H - \omega_L}{4}$) in response to a lower band signal, which is $\frac{\omega_H - \omega_L}{2}$ away from its centre frequency, (a) real-valued and (b) imaginary-valued.

Bibliography

[1] C. L. Koh, S. Weiss, and W. Liu, "A comparison of adaptive beamforming implementations for wideband scenarios," in *The 2nd IEE/EURASIP Conference on DSPenabledRadio (Ref. No. 2005/11086)*, Sep. 2005, pp. 9 pp.–.

[2] R. Mailloux, *Phased Array Antenna Handbook*, ser. Antennas and Propagation Library. Artech House, 2005.

[3] W. Liu, "Adaptive wideband beamforming with sensor delay-lines," *Signal Processing*, vol. 89, no. 5, pp. 876–882, May 2009.

[4] B. Manz, "Adaesa radar and ew together target the stovepipe," *The Journal of Electronic Defense*, vol. 36, p. 28, 2013.

[5] A. Alshammary and S. Weiss, "Low-cost and accurate broadband beamforming based on narrowband sub-arrays," in *20th International ITG Workshop on Smart Antennas, WSA*, Mar. 2016, pp. 1–6.

[6] S. A. Abdullah Alshammary, Stephan Weiss, "Grating lobe suppression in rotationally tiled arrays," in *11th European Conference on Antennas and Propagation (EUCAP)*, 2016.

[7] R. C. Hansen, *Phased Array Antennas*. John Wiley & Sons, Inc, 1998.

[8] W. L. Stutzman and G. Thiele, *Antenna theory and design*. J. Wiley, 1998.

[9] E. Brookner, "Phased array radars-past, present and future," in *RADAR 2002*, 2002, pp. 104–113.

[10] C. FS, *Waves*. McGraw-Hill, New York, NY, 1968, ch. Berkeley Physics Courses.

[11] L. Godara, *Smart Antennas*, ser. Electrical Engineering & Applied Signal Processing Series. CRC Press, 2004.

[12] J. Toomay and P. Hannen, *Radar Principles for the Non-Specialist*, ser. Electromagnetics and Radar. Institution of Engineering and Technology, 2004.

[13] Y. Lo, S. Lee, and S. Lee, *Antenna Handbook: Volume III Applications*, ser. Antenna Handbook. Springer US, 1993.

[14] W. Rotman, "Multiple beam radar antenna system," Patent 3,170,158, Feb., 1965.

[15] H. L. Van Trees, *Optimum Array Processing (Detection, Estimation, and Modulation Theory, Part IV)*, 1st ed. Wiley-Interscience, Mar. 2002.

[16] A. Vosoogh and P. S. Kildal, "Simple formula for aperture efficiency reduction due to grating lobes in planar phased arrays," *IEEE Transactions on Antennas and Propagation*, vol. 64, no. 6, pp. 2263–2269, June 2016.

[17] A. Rudge, *The Handbook of Antenna Design*, ser. Electromagnetics and Radar Series. P. Peregrinus, 1982, no. v. 1.

[18] A. Alshammary, "Frequency invariant beamforming using sensor delay line," in *Saudi International Electronics, Communications and Photonics Conference (SIECPC)*, 2011, pp. 1–5.

[19] A. Yardim, G. D. Cain, and P. Henry, "Optimal two-term offset windowing for fractional delay," *Electronics Letters*, vol. 32, no. 6, pp. 526–527, Mar 1996.

[20] R. Mailloux, "Subarray technology for large scanning arrays," in *The Second European Conference on Antennas and Propagation. EuCAP*, Nov. 2007, pp. 1–6.

[21] L. Bui, A. Mitchell, K. Ghorbani, T.-H. Chio, S. Mansoori, and E. Lopez, "Wideband photonically phased array antenna using vector sum phase shifting approach," *IEEE Transactions on Antennas and Propagation*, vol. 53, no. 11, pp. 3589–3596, 2005.

[22] W. Liu and S. Weiss, "Beam steering for wideband arrays," *Signal Processing*, vol. 89, no. 5, pp. 941–945, 2009.

[23] S. Doclo and M. Moonen, "Design of broadband beamformers robust against gain and phase errors in the microphone array characteristics," *IEEE Transactions on Signal Processing*, vol. 51, no. 10, pp. 2511–2526, 2003.

[24] M. Ghavami, "Wideband beamforming using rectangular arrays without phase shifting," *European Transactions on Telecommunications*, vol. 14, no. 5, pp. 449–456, 2003.

[25] W. Liu and S. Weiss, "Broadband beamspace adaptive beamforming with spatial-only information," in *5th IEEE Sensor Array and Multichannel Signal Processing Workshop, SAM*, 2008, pp. 330–334.

[26] *Measured transmit nulling performance in wideband arrays*, May 2012.

[27] H. Duan, B. P. Ng, C. M. S. See, and J. Fang, "Broadband beamforming using tdl-form IIR filters," *IEEE Transactions on Signal Processing*, vol. 55, no. 3, pp. 990–1002, Mar. 2007.

[28] W. Zhang and T. Su, "Reference beam pattern design for frequency invariant beamforming based on fast Fourier transform," *Sensors*, vol. 16, no. 10, p. 1554, 2016.

[29] A. Abbaspour-Tamijani and K. Sarabandi, "An affordable millimeter-wave beam-steerable antenna using interleaved planar subarrays," *IEEE Transactions on Antennas and Propagation*, vol. 51, no. 9, pp. 2193–2202, Sep. 2003.

[30] R. J. Mailloux, "Constrained feed techniques for limited field of view scanning or time delay steering," in *IEEE Antennas and Propagation Society International Symposium*, vol. 2, 1998, Conference Proceedings, pp. 740–743 vol.2.

[31] R. L. Haupt, *Timed and Phased Array Antennas.* John Wiley & Sons, Inc, 2015, pp. 1–9.

[32] R. J. Mailloux, "Electronically scanned arrays," *Synthesis Lectures on Antennas*, vol. 2, no. 1, pp. 1–82, 2007.

[33] Z.-Y. Xiong, Z.-H. Xu, S.-W. Chen, and S.-P. Xiao, "Subarray partition in array antenna based on the algorithm x," *IEEE Antennas and Wireless Propagation Letters*, vol. 12, pp. 906–909, 2013.

[34] W.-D. Wirth, *Radar Techniques Using Array Antennas*, ser. Radar, Sonar, Navigation and Avionics. Institution of Engineering and Technology, 2013.

[35] E. Knott, J. Schaeffer, and M. Tulley, *Radar Cross Section*, ser. Electromagnetics and Radar Series. Institution of Engineering and Technology, 2004.

[36] S. Boyd and L. Vandenberghe, *Convex Optimization*. New York, NY, USA: Cambridge University Press, 2004.

[37] A. Tkacenko, P. Vaidyanathan, and T. Nguyen, "On the eigenfilter design method and its applications: a tutorial," *IEEE Transactions on Circuits and Systems II: Analog and Digital Signal Processing*, vol. 50, no. 9, pp. 497–517, 2003.

[38] P. Patwardhan and V. Gadre, "Design of 2-D mth band lowpass FIR eigenfilters with symmetries," *IEEE Signal Processing Letters*, vol. 14, no. 8, pp. 517–520, 2007.

[39] P. Vaidyanathan and T. Nguyen, "Eigenfilters: A new approach to least-squares FIR filter design and applications including Nyquist filters," *IEEE Transactions on Circuits and Systems*, vol. 34, no. 1, pp. 11–23, 1987.

[40] S.-c. Pei and C.-C. Tseng, "A new eigenfilter based on total least squares error criterion," *IEEE Transactions on Circuits and Systems I: Fundamental Theory and Applications*, vol. 48, no. 6, pp. 699–709, 2001.

[41] S. C. Pei and J. J. Shyu, "2-D FIR eigenfilters: a least-squares approach," *IEEE Transactions on Circuits and Systems*, vol. 37, no. 1, pp. 24–34, Jan. 1990.

[42] A. Nashashibi and C. Charalambous, "2D FIR eigenfilters," in *IEEE International Symposium on Circuits and Systems*, 1988, pp. 1037–1040 vol.2.

[43] A. Djebbari, J. Rouvaen, A. Djebbari, M. Belbachir, and S. Elahmar, "A new approach to the design of limit cycle-free {IIR} digital filters using eigenfilter method," *Signal Processing*, vol. 72, no. 3, pp. 193–198, 1999.

[44] P. S. R. Diniz, *Adaptive Filtering: Algorithms and Practical Implementation*, 4th ed. Springer, 2013.

[45] T. Laakso, V. Valimaki, M. Karjalainen, and U. Laine, "Splitting the unit delay [FIR/all pass filters design]," *IEEE Signal Processing Magazine*, vol. 13, no. 1, pp. 30–60, Jan. 1996.

[46] S. J. Orfanidis, *Electromagnetic waves and antennas*. Rutgers University New Brunswick, NJ, 2002.

[47] W. Liu and S. Weiss, *Wideband Beamforming: Concepts and Techniques*, ser. Wireless Communications and Mobile Computing. Wiley, 2010.

[48] W. Fu and D. Jiang, "Radar wideband digital beamforming based on time delay and phase compensation," *International Journal of Electronics*, vol. 105, no. 7, pp. 1144–1158, 2018. [Online]. Available: https://doi.org/10.1080/00207217.2018.1426121

[49] L. K. Lam, "Mixed signal true time delay digital beamformer," Patent US20 020 013 133A1, 1999.

[50] J. O. S. III, *Introduction to Digital Filters with Audio Applications*, S. . Edition, Ed. Stanford University, 2007.

[51] J. Selva, "An efficient structure for the design of variable fractional delay filters based on the windowing method," *IEEE Transactions on Signal Processing*, vol. 56, no. 8, pp. 3770–3775, Aug. 2008.

[52] M. A. Alrmah and S. Weiss, "Filter bank based fractional delay filter implementation for widely accurate broadband steering vectors," in *5th IEEE International Workshop on Computational Advances in Multi-Sensor Adaptive Processing (CAMSAP)*, Dec. 2013, pp. 332–335.

[53] S. Minocha, S. C. D. Roy, and B. Kumar, "A note on the fir approximation of a fractional sample delay," *International Journal of Circuit Theory and Applications*, vol. 21, no. 3, pp. 265–274, 1993.

[54] T. Laakso and Valimaki, "Principles of fractional delay filters," in *IEEE International Conference on Acoustics, Speech and Signal Processing*, 2000.

[55] T. C. Q. Alfred and S. Sanyal, "Overlapped subarray architecture of an wideband phased array antenna with interference suppression capability," *Journal of Electromagnetic Analysis and Applications*, vol. 5, no. 5, pp. 201–204, 2013.

[56] G. H. Golub and C. F. Van Loan, *Matrix Computations (3rd Ed.)*. Baltimore, MD, USA: Johns Hopkins University Press, 1996.

[57] H. Duan, B. P. Ng, C. M. S. See, and J. Fang, "Applications of the {SRV} constraint in broadband pattern synthesis," *Signal Processing*, vol. 88, no. 4, pp. 1035–1045, 2008.

[58] R. L. Haupt, "Optimized weighting of uniform subarrays of unequal sizes," *IEEE Transactions on Antennas and Propagation*, vol. 55, no. 4, pp. 1207–1210, Apr. 2007.

[59] R. J. Mailloux, "Subarray technology for time delayed scanning arrays," in *IEEE International Conference on Microwaves, Communications, Antennas and Electronics Systems, COMCAS.*, 2009, Conference Proceedings, pp. 1–6.

[60] T. Li and X. Wang, "Wideband digital beamforming by implementing digital fractional filter at baseband," in *International Conference on Communications, Circuits and Systems (ICCCAS)*, vol. 2, Nov. 2013, pp. 182–185.

[61] R. Tang, *Survey of time delay beam steering techniques.* Dedham, MA: Artech House, 1970.

[62] Y. Cao, Y. Wang, S. Wang, and S. Zhou, "Wideband subarray beamforming based on subband decomposition," in *IEEE China Summit International Conference on Signal and Information Processing (ChinaSIP)*, Jul. 2014, pp. 247–251.

[63] M. E. Bialkowski and M. Uthansakul, "A wideband array antenna with beam-steering capability using real valued weights," *Microwave and Optical Technology Letters*, vol. 48, no. 2, pp. 287–291, 2006.

[64] I. Dotlic, "Minimax frequency invariant beamforming," *Electronics Letters*, vol. 40, no. 19, pp. 1230–1231, 2004.

[65] K. Prabhu, *Window Functions and Their Applications in Signal Processing.* CRC Press, 2013.

[66] V. MADISETTI, *The Digital Signal Processing Handbook*, ser. Electrical Engineering Handbook. Taylor & Francis, 1997.

[67] C. Tarran, M. Mitchell, and R. Howard, "Wideband phased array radar with digital adaptive beamforming," in *IEE Colloquium High Resolution Radar and Sonar (Ref. No. 1999/051)*, 1999, pp. 11–17.

[68] R. C. Hansen and G. G. Charlton, "Subarray quantization lobe decollimation," *IEEE Transactions on Antennas and Propagation*, vol. 47, no. 8, pp. 1237–1239, Aug. 1999.

[69] Y. Krivosheev and A. Shishlov, "Grating lobe suppression in phased arrays composed of identical or similar subarrays," in *IEEE International Symposium on Phased Array Systems and Technology (ARRAY)*, Oct. 2010, pp. 724–730.

[70] V. D. Agrawal, "Grating-lobe suppression in phased arrays by subarray rotation," *Proceedings of the IEEE*, vol. 66, no. 3, pp. 347–349, Mar. 1978.

[71] H. Wang, D. G. Fang, and Y. L. Chow, "Grating lobe reduction in a phased array of limited scanning," *IEEE Transactions on Antennas and Propagation*, vol. 56, no. 6, pp. 1581–1586, Jun. 2008.

[72] D. Frey, "Robust system design," University Lecture, 1998.

[73] J. S. Oakland, "Chapter 1 - quality, processes and control," in *Statistical Process Control (Sixth Edition)*, sixth edition ed., J. S. Oakland, Ed.

Oxford: Butterworth-Heinemann, 2008, pp. 3 – 22. [Online]. Available: https://www.sciencedirect.com/science/article/pii/B9780750669627500043

[74] J. K. G. . G. J. Prasad, "Modularity in product design for manufacturability," *International Journal of Agile Manufacturing*, vol. 1, Aug. 1997.

[75] N. Bali and N. Iyengar, *A Textbook of Engineering Mathematics: For B.Sc. (Engg.). B.E., B.Tech., M.E. and Equivalent Professional Exams.* Laxmi Publications, 2004.

[76] S. Lee, R. T. Collins, and Y. Liu, "Rotation symmetry group detection via frequency analysis of frieze-expansions," in *IEEE Conference on Computer Vision and Pattern Recognition*, Jun. 2008, pp. 1–8.

[77] B. Grünbaum and G. C. Shephard, *Tilings and Patterns.* New York, NY, USA: W. H. Freeman & Co., 1986.

[78] C. Horne and E. Textile Institute (Manchester, *Geometric Symmetry in Patterns and Tilings*, ser. Woodhead Publishing Series in Textiles. CRC Press, 2000.

[79] J. D. Wolter, T. C. Woo, and R. A. Volz, "Optimal algorithms for symmetry detection in two and three dimensions," *The Visual Computer*, vol. 1, no. 1, pp. 37–48, 1985.

[80] D. Schattschneider, "Tiling the plane with congruent pentagons," *Mathematics Magazine*, vol. 51, 1978.

[81] T. Hahn, *International Tables for Crystallography, Space-Group Symmetry*, ser. International Tables for Crystallography. Wiley, 2005.

[82] M. Hirschhorn and D. Hunt, "Equilateral convex pentagons which tile the plane," *Journal of Combinatorial Theory, Series A*, vol. 39, no. 1, pp. 1–18, 1985.

[83] E. W. Weisstein, "Pentagon tiling." A Wolfram Web Resource., 2015.

[84] C. Mann, J. McLoud-Mann, and D. Von Derau, "Convex pentagons that admit i-block transitive tilings," 10 2015.

[85] I. Niven, "Convex polygons that cannot tile the plane," *The American Mathematical Monthly*, vol. 85, no. 10, pp. 785–792, 1978. [Online]. Available: http://www.jstor.org/stable/2320624

[86] R. B. Kershner, "On paving the plane," *The American Mathematical Monthly*, vol. 75, no. 8, pp. 839–844, 1968. [Online]. Available: http://www.jstor.org/stable/2314332

[87] D. Schattschneider, "Marjorie rice and the maa tiling," *Journal of Mathematics and the Arts*, vol. 12, no. 2-3, pp. 114–127, 2018. [Online]. Available: https://doi.org/10.1080/17513472.2018.1453740

[88] T. A. Milligan, *Modern antenna design*, 2nd, Ed. Wiley & Sons, Inc, 2005.

[89] G. Loy and J.-O. Eklundh, "Detecting symmetry and symmetric constellations of features," in *Proceedings of the 9th European Conference on Computer Vision - Volume Part II*, ser. ECCV'06. Berlin, Heidelberg: Springer-Verlag, 2006, pp. 508–521.

[90] V. S. N. Prasad and L. S. Davis, "Detecting rotational symmetries," in *Tenth IEEE International Conference on Computer Vision (ICCV'05) Volume 1*, vol. 2, Oct. 2005, pp. 954–961 Vol. 2.

[91] V. Sipal, D. Edwards, and B. Allen, "Bandwidth requirement for suppression of grating lobes in ultrawideband antenna arrays," in *IEEE International Conference on Ultra-Wideband*, Sept 2012, pp. 236–240.